



Universiteit  
Leiden  
The Netherlands

## **Granular flows : fluidization and anisotropy**

Wortel, G.H.

### **Citation**

Wortel, G. H. (2014, November 19). *Granular flows : fluidization and anisotropy*. Casimir PhD Series. Retrieved from <https://hdl.handle.net/1887/29750>

Version: Not Applicable (or Unknown)

License: [Leiden University Non-exclusive license](#)

Downloaded from: <https://hdl.handle.net/1887/29750>

**Note:** To cite this publication please use the final published version (if applicable).

Cover Page



Universiteit Leiden



The handle <http://hdl.handle.net/1887/29750> holds various files of this Leiden University dissertation

**Author:** Wortel, Geert

**Title:** Granular flows : fluidization and anisotropy

**Issue Date:** 2015-11-19

# Granular Flows: Fluidization and Anisotropy

PROEFSCHRIFT

ter verkrijging van  
de graad van Doctor aan de Universiteit Leiden,  
op gezag van Rector Magnificus  
prof. mr. C.J.J.M. Stolker,  
volgens besluit van het College voor Promoties  
te verdedigen op 19 november 2014  
klokke 11.15 uur

door

**Gerrit Herman Wortel**  
geboren te Zoetermeer  
in 1985

## Promotiecommissie:

Promotor: Prof. dr. M.L. van Hecke

Overige leden: Dr. O. Dauchot (*ESPCI-ParisTech, Frankrijk*)

Prof. dr. E.R. Eliel

Dr. D.L. Henann (*Brown University, VS*)

Dr. D.J. Kraft

Prof. dr. T.H. Oosterkamp

Prof. dr. M.A.J.G. Orrit

Prof. dr. H. Schiessel

Nederlandse titel:

Granulaire Stroming: Fluïdisatie en Anisotropie

Cover image: Sand Dunes, Huacachina, Peru cc by N. Whitford

Casimir PhD series, Delft-Leiden 2014-26

ISBN 978-90-8593-199-7

Dit werk maakt deel uit van het onderzoeksprogramma van de Stichting voor Fundamenteel Onderzoek der Materie (FOM), die financieel wordt gesteund door de Nederlandse Organisatie voor Wetenschappelijk Onderzoek (NWO).



*If we stand on the shore and look at the sea,  
we see the water, the waves breaking, the foam,  
the sound, the air, the winds and the clouds,  
the sun and the blue sky, and light.  
There is sand and there are rocks.  
There are animals and seaweed,  
hunger and disease,  
and the observer on the beach.*

*Any other spot in nature has a similar variety of things.  
It is always as complicated as that, no matter where it is.  
Curiosity demands that we ask questions,  
that we try to understand this multitude of aspects as resulting from  
the action of a relatively small number of elemental things,  
and forces acting in an infinite variety of combinations.*

*Is the sand other than the rocks?  
Is the moon a great rock?  
Is the sand perhaps nothing but a great number of very tiny stones?*

*– Richard P. Feynman  
The Feynman Lectures on Physics, p2-1*



---

# Contents

---

<b>1</b>	<b>Introduction to Granular Matter</b>	<b>1</b>
1.1	Granular Materials . . . . .	1
1.2	Examples . . . . .	4
1.2.1	Grain Silo . . . . .	4
1.2.2	Brazil Nut Effect . . . . .	5
1.2.3	Quicksand . . . . .	5
1.2.4	Soft Robotic Gripper . . . . .	6
1.2.5	Shear Thinning and Thickening . . . . .	6
1.3	Shear and Vibration . . . . .	7
1.4	This Thesis . . . . .	8
<b>2</b>	<b>Introduction to Flow of Weakly Vibrated Granular Media</b>	<b>9</b>
2.1	Introduction . . . . .	9
2.2	Setup and Protocol . . . . .	10
2.3	Phenomenology . . . . .	14
2.3.1	$\Gamma = 0$ . . . . .	14
2.3.2	$\Gamma > 0$ . . . . .	15
2.3.3	Simplest Model . . . . .	15
2.3.4	Hysteretic Transition . . . . .	16
<b>3</b>	<b>Vibration Dominated Flow in Weakly Vibrated Granular Media</b>	<b>19</b>
3.1	Introduction . . . . .	19
3.2	Protocol . . . . .	20
3.3	Phenomenology . . . . .	23
3.4	Vibration Dominated Flows . . . . .	25
3.4.1	Torque Minimization Model . . . . .	26
3.4.2	Frictional Model for $\Gamma > 0$ . . . . .	29
3.4.3	Fluidized Region . . . . .	33

3.5	Conclusion . . . . .	37
<b>4</b>	<b>A Nontrivial Critical Point in Granular Flows</b>	<b>39</b>
4.1	Introduction . . . . .	39
4.2	Setup and Protocol . . . . .	43
4.2.1	Protocol . . . . .	45
4.3	Theoretical Framework . . . . .	46
4.4	Flow Curves . . . . .	49
4.5	Fluctuations . . . . .	53
4.5.1	Phenomenology . . . . .	54
4.5.2	Determination of the Velocity . . . . .	55
4.5.3	Autocorrelation . . . . .	57
4.5.4	Statistics of $\Delta\theta$ . . . . .	64
4.5.5	Locating the Critical Point . . . . .	66
4.5.6	Scaling of Fluctuations . . . . .	69
4.A	Appendix . . . . .	74
4.A.1	Collective Behavior . . . . .	74
4.A.2	$T$ -Control Flow Curves . . . . .	74
4.A.3	Towards a Simple Model . . . . .	76
<b>5</b>	<b>The Role of Anisotropy in Granular Flow</b>	<b>77</b>
5.1	Introduction . . . . .	77
5.2	Protocol . . . . .	79
5.3	Steady State Relaxation . . . . .	81
5.3.1	Relaxation Speed . . . . .	81
5.3.2	Dependence on $(\Omega, \Gamma)$ and $(T, \Gamma)$ . . . . .	83
5.3.3	Conclusion . . . . .	85
5.4	Dynamics of Anisotropy . . . . .	85
5.4.1	Relaxing from Preshear to Steady State . . . . .	86
5.4.2	Two Stage Relaxation . . . . .	87
5.5	Conclusion and Discussion . . . . .	92
5.5.1	Outlook . . . . .	94
<b>6</b>	<b>Giant Heaping in Sheared Anisotropic Granular Media</b>	<b>95</b>
6.1	Introduction . . . . .	95
6.2	Setup and Methods . . . . .	98
6.2.1	Setup . . . . .	98
6.2.2	Methods . . . . .	100

6.3	Phenomenology . . . . .	103
6.3.1	Growth Evolution . . . . .	103
6.3.2	Aspect Ratio, Shape and Material . . . . .	105
6.3.3	Heap Location . . . . .	105
6.3.4	Filling Height Dependence . . . . .	105
6.4	The Mechanism behind the Heaping . . . . .	108
6.4.1	Heap Removal . . . . .	108
6.4.2	Reversal . . . . .	110
6.4.3	Convection . . . . .	111
6.4.4	Conclusion . . . . .	112
6.5	3D X-ray CT Tomography . . . . .	113
6.5.1	Setup and Methods . . . . .	113
6.5.2	Results . . . . .	115
6.5.3	Origin of the Convection . . . . .	117
6.5.4	Conclusion . . . . .	122
6.A	Appendix . . . . .	123
6.A.1	Outlook . . . . .	123
<b>Bibliography</b>		<b>125</b>
<b>Samenvatting</b>		<b>137</b>
<b>Summary</b>		<b>139</b>
<b>Publication List</b>		<b>141</b>
<b>Curriculum Vitae</b>		<b>143</b>
<b>Acknowledgements</b>		<b>145</b>



# INTRODUCTION TO GRANULAR MATTER

---

## 1.1 Granular Materials

Granular materials are present all around us. Common examples include sand, rice, powder, coal, cement, seeds, pills, rock avalanches, and on a much larger scale a collection of icebergs, and the particles that form the rings of Saturn. Because of this omnipresence, research on granular materials is relevant for everyday applications, but it also presents intriguing fundamental challenges [1–4].

The two most basic characteristics of a granular material are that its constituents must be large enough to not be significantly influenced by thermal fluctuations, and that the interactions between particles are dissipative. In practice, the lower limit size for the grains is about  $1\text{ }\mu\text{m}$ . For a typical sand grain raised in height by its own radius ( $0.5\text{ mm}$ ), the difference between the potential and the thermal energy is a startling factor  $10^{13}$  [1].

Like water, that, depending on temperature and pressure, can be solid (ice), liquid (water) or gas (vapor), a granular material can also show behavior that corresponds to different phases of matter. When you walk on the beach, the sand behaves like a solid and carries your weight. When you sit down and take off your shoes, the sand flows out of these as if it were a liquid. When shaken vigorously, sand behaves like a gas.

A pile of sand behaves like a solid because it is jammed due to the gravity-induced pressure. The friction between the grains plays an additional strengthening role. The stresses in a granular solid are not distributed uniformly, but are conducted away along so-called force chains [5–8], which are networks of grains with relatively strong contacts.

For making sand show liquid or gas-like properties, it has to be forced externally to drive it away from its equilibrium state. This can be done for example by tilting or vibrating the system. Surprisingly, a very small displacement of a particle can significantly alter the force chains and weaken the packing [6].

Despite some similarities between the behavior of granular solids, liquids, and gasses to their molecular counterparts, the granular phases exhibit a range of unique properties [1–4].

An example of a specific property of granular solids is that they dilate under external shear. This is caused by the shear deformation which disrupts the close-packed arrangement of the grains, forcing them into less dense arrangements. This mechanism explains the white rings around footprints made by someone walking on wet sand. The shear flow induced by a foot widens the voids between the grains. As a result, the water can drain away, which in turn makes the sand drier and whiter.

Another specific property of granular phases is found in granular liquids. Sand in an hourglass always flows at the same rate, irrespective of the amount of sand that is left in the upper vessel. In an hourglass filled with water, the flow slows down as the water level in the upper vessel (and hence the hydrostatic pressure) decreases. Sand hardly builds up a hydrostatic pressure in such a container, because the gravitational force is re-directed towards the sides of the hourglass via the force chains in the packing [9].

A very counterintuitive property of a granular gas is its tendency to cluster. An ordinary gas will spread over the entire available space, but a granular gas does the opposite: it forms clusters [10, 11]. The reason for this lays in the inelastic collisions between the grains. Once a region is denser because of a fluctuation, the particles in that region will collide more, lose more energy and form a dense cluster.

Granular materials are part of a bigger class of materials that exhibit the *jamming transition*. This transition, which separates a disordered solid-like state and a liquid-like phase, is also used to describe colloidal suspensions, emulsions, foams and even elastic networks [12–14].

Early granular research was performed by pioneers such as Coulomb (who investigated the stability of a granular heap from the point of friction [15]), Faraday (who studied heaping of the surface of a vibrated pow-



der [16]), Hagen and Janssen (who described saturation of pressure with depth in silos [9, 17]), Reynolds (who introduced the notion of dilatancy [18]), and traveler and World War I & II veteran Bagnold, who studied sand and desert dunes [19], as well as the flow of dense suspensions and granular materials.

Knowledge about the behavior of grains is very relevant for industrial applications, as many industries rely on the mining, milling, mixing, transporting, and storing of granular materials. It has been estimated that more than 50% of sales in the world involve products produced using granular materials at some stage [2, 3]. Major sectors that work with granular materials include civil engineering, the chemical (fuels and catalysts are often used in the form of grains to maximize the surface area), mining, pharmaceutical (powders are used to make pills), food, and glass industry. Estimates say that there are energy losses up to 40% in industrial processes that involve granular media, which are caused by a lack of knowledge on how to handle them [20]. Another major domain of applications of granular materials is earth science (geophysics), as our soil is mostly composed of grains. Examples of granular physics at play are avalanches, landslides, dune formation, erosion, and earthquakes.

In the 1980's, physicists got interested in granular media. Fundamentally, an important consequence of the fact that a granular system is athermal and dissipative, is that the system cannot explore phase space, and therefore is strongly non-equilibrium. In the absence of external forcing, each metastable configuration of the material will last indefinitely, and no thermal averaging over nearby configurations occurs. Because each configuration is unique and has its own precise properties, a granular experiment can never be precisely reproduced and results have to be defined in terms of ensemble averages. Because  $k_B T$  is effectively zero, traditional thermodynamic methods are not applicable to granular materials. Moreover, when driven, a wealth of counterintuitive phenomena arises. For example: vibrations make particles of different sizes separate to different regions of the system rather than mix them [21]. Since there are no attractive forces between the particles, this separation appears to violate the principle that entropy is always maximized, which normally favors mix-

ing. In a granular material, the influence of (thermodynamic) entropy is small compared to dominant dynamical effects.

Granular systems offer a relatively simple possibility to study dissipative systems far from equilibrium. Noble Prize winner De Gennes originally used sandpile avalanches as a macroscopic picture for the motion of flux lines in a type-II superconductor [22]. Slow relaxations that are found in vibrated sandpiles show behavior that is similar to the slow relaxation found in glasses, spin glasses and flux lattices [1]. Nonlinear dynamical phenomena are observed, which are useful to understand the breakdown phenomena in semiconductors, stick-slip friction on a microscopic, and earth-quake dynamics on a macroscopic scale [1].

## 1.2 Examples

In this section I will describe some examples of granular research that focuses on every day applications.

### 1.2.1 Grain Silo

A very concrete and relevant example of granular physics at work is the grain silo. The silo illustrates clearly what can go wrong if - because of a lack of understanding of granular physics - a granular material is handled as if it were a regular solid or liquid. When building a silo, the forces that will work on the bottom and side walls of the silo have to be estimated to determine how strong the walls need to be.

Naively, you could expect most of the weight of the particles to be carried by the bottom of the silo, so the sidewalls can be made thin. As explained in the previous section, in a granular system, a significant part of the forces is carried to the side walls [9, 17]. So in fact, a thin wall will not suffice. This effect is even enhanced by the fact that these forces are not distributed homogeneously over the entire side wall. At the points where the force chains of particles that carry most of the weight hit the wall, the force that the wall has to sustain is significantly higher than the force that corresponds to a homogeneous estimate. Unfortunately, many silos are still built with walls that are too thin – they will rupture and cause the entire silo to collapse [4].

Another significant complication that occurs in silos is clogging of the grains. Two important questions are how to minimize the probability of clogging, and how to make the grains unjam in case it clogs nonetheless. Going into the silo to unclog the grains by hand is extremely dangerous; no less than 25 deaths a year in grain silos are reported in the United States alone [23]. This clearly shows the relevance of understanding how to deal with granular materials.

### 1.2.2 Brazil Nut Effect

A granular effect that is widely known is the Brazil Nut Effect (or: Muesli Effect). This effect describes the phenomenon that in a jar of muesli or nuts, the biggest nuts always raise to the surface. The origin of this effect is not trivial to describe, as there are three physical mechanisms that cause the segregation of the big and the small particles [24]. The simplest mechanism is that when the system is agitated, the small particles can fill small voids at the bottom of the system while bigger particles cannot. As a result, small particles migrate downwards and big ones upwards. Surprisingly, the air pressure also plays a role, as the rearrangement of nuts requires air flow. The practical implications of this effect on transporting and storing granular materials are immense.

Another manifestation of this effect is the observation that in a bag of potato chips, the biggest chips are at the top of the bag. A good method to get the chips out uniformly mixed is by opening the package on the bottom [25].

### 1.2.3 Quicksand

A question that often arises when discussing granular materials is “can one drown in quicksand?” The *simple* answer to this question is “no”; the density of quicksand is twice as high as the density of a human, so according to Archimedes’ law, a person in quicksand will only sink up to their waist [26].

The *complex* answer to the question is: “that depends on the definition of quicksand”. Actual quicksand is a relatively dense mixture of clay, sand, and water, in which a person cannot drown. On the contrary, research has been done on so-called dry quicksand [27], which consists of a loose packing of 40  $\mu\text{m}$  grains and air. By blowing air through the pack-

ing, a packing fraction of 41% can be reached. Taking a material density of sand (quartz) of 2.65 kg/l, this results in a density of 1.09 kg/l. This is remarkably close to the density of the human body, which is around 1.06 kg/l. This leads to the conclusion that it would be possible to drown in this system. In the desert, similar packings may evolve from the sedimentation of very fine sand after it has been blown into the air by the wind.

### 1.2.4 Soft Robotic Gripper

A recent and very nice application of granular physics is the soft robotic gripper [28, 29]. A bag, filled with grains (*e.g.* coffee powder), is gently placed on an object. As air is pumped out off the bag, the grains jam, become rigid, and the bag will grab on to the object. A soft robotic gripper has been produced which can grab almost any object without breaking it; examples include an egg, a drinking glass, or a pen. By pumping air back into the bag, the gripper releases the object. By creating an overpressure, the object can be ejected. Via this mechanism the robotic gripper is able to play darts [30]. The gripper is simple, cheap, firm, and able to work with fragile objects. Because of its simplicity and reliability, the gripper could be very suitable for use in outer space [31].

In order to jam and unjam the packing with as little air as possible, the coffee powder can be replaced by 3D printed particles whose shape has been optimized using evolutionary algorithms [32].

### 1.2.5 Shear Thinning and Thickening

Physicists in general often describe a fluid or viscous material in terms of viscosity. Granular materials, similar to materials such as ketchup and blood, become less viscous when they are sheared. This kind of material behavior is called *shear thinning*. An everyday example of such a material is modern paint. When modern paints are applied, the shear created by the brush or roller will allow them to thin and wet out the surface evenly. Once applied, the paint regains its higher viscosity which avoids drips and runs.

Water belongs to a different class of materials called *Newtonian fluids*. For these types of matter, the viscosity is independent of the flow rate.

A third and perhaps most intriguing class are the *shear thickening* materials which become stiffer when sheared. The best known example is cornstarch. When gently stirred, it behaves like a liquid, but if smacked on with a hammer, it becomes rock hard [33]. Similarly, one can run over a big bath of cornstarch, but when walking gently, one sinks in. Two possible applications of shear thickening materials are a speed bump that is soft when you drive slowly, but hard when you drive too fast [34], and a bulletproof vest that is comfortable to wear because it only becomes stiff when hit by a fast bullet [35].

### 1.3 Shear and Vibration

An unperturbed granular material is rigid because of friction and gravity-induced pressure. To make the material yield and flow, it has to be forced externally [1, 2, 36–43]. The best known scenario that leads to granular flow is exerting a shear stress that is large enough to overcome the friction. This can for instance be done by simply tilting a layer of sand [1, 2].

Another possibility to let a granular material yield, is to first make it lose its rigidity using mechanical agitations. These agitations itself do not have to induce flow [38, 44–49]. To actually make the system flow, an additional stress is exerted, and the resulting flow rate then depends on both the amount of agitation and the stress [38, 44, 47, 50]. The idea that both the stress and the amount of agitations determine the flow rate, lies at the basis of numerous models for slowly flowing disordered materials [51–54].

A well-known method to agitate a granular system is by using vibrations. Experiments where the role of vibrations were studied include: (i) an experiment where the maximum angle of a stable granular slope was found to decrease with the amount of vibrations [41, 55], (ii) an experiment where granular flow on an inclined plane was induced using vibrations [39, 40], and (iii) a study that reported how grains flow out of a silo more easily when vibrated [56].

In many experiments it is found that even a tiny amount of agitations significantly weakens the system. This is caused by the fact that the force chains in the packing can already be disturbed by a small displacement of a particle [6]. This was for instance shown in experiments where piezo crystals are used to induce tiny rearrangements in the material [43, 57,

58]. Similarly, a system can also be weakened using tiny shear-induced agitations [59].

Once a system is flowing, it is agitated by the flow itself, even *far away* from the flowing region [38, 44, 60–63]. Agitations therefore play a crucial role in non-local granular rheology models [37, 64–67]. They may even, among other things, explain the large extension of shear bands in split-bottom granular flows [68–70].

Chapter 2-5 of this thesis will be devoted to experiments where we shear a weakly vibrated granular packing. Even though we use a low peak acceleration for the vibrations, and always stay below 1 g, we find that the vibrations significantly influence the flow properties of the system.

### 1.4 This Thesis

This thesis starts with an introduction to the flow of weakly vibrated granular media in chapter 2, which describes the results found in prior work using the same experimental setup [13, 71]. In chapter 3, we study to which extent the frictional description of granular materials is still valid in the case of weak vibrations. We do this by altering the pressure, which affects the frictional contacts. When the acceleration approaches 1 g, we find that the system loses its pressure dependence and behaves more like a liquid. In chapter 4, we focus on the transition between slow flows - which are enabled by the vibrations - and fast inertial flows. For a certain amount of vibrations, the regimes of slow and fast flow start to merge. We investigate the resemblance between this point and a second-order critical point, and investigate the scaling of several flow properties with the distance to the potential granular critical point. In chapter 5, we show the presence and importance of anisotropy, which is built into the system when it is sheared in a certain direction. We find that the anisotropy varies with flow rate and vibration intensity, where the anisotropy is directly related to the required shear stress.

In chapter 6, we change focus and look at the flow of rod-shaped anisotropic particles (without vibrations). We find that the fact that the particles now have an orientation, causes a strong convection, which results in a heap of particles that arises from the surface of the packing.

# INTRODUCTION TO FLOW OF WEAKLY VIBRATED GRANULAR MEDIA

---

A large part of this thesis will be devoted to flow of weakly vibrated granular media. In this chapter we will introduce the subject, describe the setup, and show the *prior results*<sup>1</sup> that were obtained before the work that is reported in chapter 3-5 of this thesis.

## 2.1 Introduction

In the absence of external forcing, a collection of granular particles jams into a metastable configuration under the influence of gravity-induced pressure and friction. To make the system flow, a shear stress larger than the so-called yield stress has to be imposed, large enough to overcome the friction between the grains. When imposing a stress below the yield stress, the material will not exhibit a steady flow, although typically there will be rearrangements at the micro-scale. For a stress above the yield stress, the material loses its rigidity and will typically start to flow fast. Surprisingly, creating a slow granular flow is not easy or perhaps even possible in a stress-controlled experiment [71].

Flow experiments can also be performed in rate-controlled geometries. In these experiments, slow flows are unstable and the stress appears to be *independent* of the flow rate (for slow enough flows). This is believed to be due to the rate-independence of the microscopic friction law.

---

<sup>1</sup>J. Dijksman, G. Wortel, L. van Dellen, O. Dauchot, and M. van Hecke, *Jamming, Yielding and Rheology of Weakly Vibrated Granular Media*, Phys. Rev. Lett. **107**, 108303 (2011) [71]

Granular flow in general is induced by imposing either a stress or a strain (rate). In the traditional inclined plane geometry [72, 73], the stress is controlled by changing the tilt angle with respect to gravity. Because of the yield stress, strain-controlled experiments are typically used when studying slow flows [13].

Granular systems can be compared to thermal systems such as glasses [74, 75]. The simple case without external forcing then corresponds to the zero temperature case. Glasses are typically studied in the more interesting case of finite temperature; equivalently, we will study granular materials subject to weak vibrations. We keep the peak acceleration of our vibrations below the gravity acceleration, which means the particles do not fly around as they do in a granular gas, but essentially stay at their relative positions.

During the upward part of the oscillation, gravity is effectively decreased, which makes it easier to make the particles flow. In the experiments, a new, stable, slow, granular flow regime is found where the stress is now *dependent* on the flow rate [13, 71]. This regime, where a granular material can flow slowly under the influence of vibrations, is utilized by many people every morning while gently pouring cereal in a breakfast bowl.

## 2.2 Setup and Protocol

**Split-Bottom Cell** – We probe the rheology of weakly vibrated granular flows in a modified split-bottom cell, as shown in Fig. 2.1. The split-bottom cell consists of an acrylic container with an inner radius  $r_0$  of 7.0 cm and a height  $H$  of 5.5 cm. The rotating inner disk that drives the flow has a radius  $r_s$  of 4 cm and thickness 5 mm. The gap between the container and the disk is about 0.3 mm so no particles can get underneath the disk. To ensure a no-slip boundary condition, the top surface of the disk is made rough by gluing glass particles with diameter of 2 mm to it.

The flow structure in the split-bottom cell depends crucially on the relative filling height  $H_0/r_s$  [76]. For low filling heights, the particles above the inner disk corotate with it, whereas the particles close to the outer wall remain stationary. The only location where there is shear between the co-moving and the stationary grains, is above the split in the bottom. For higher filling heights, the part of the system that corotates decreases with



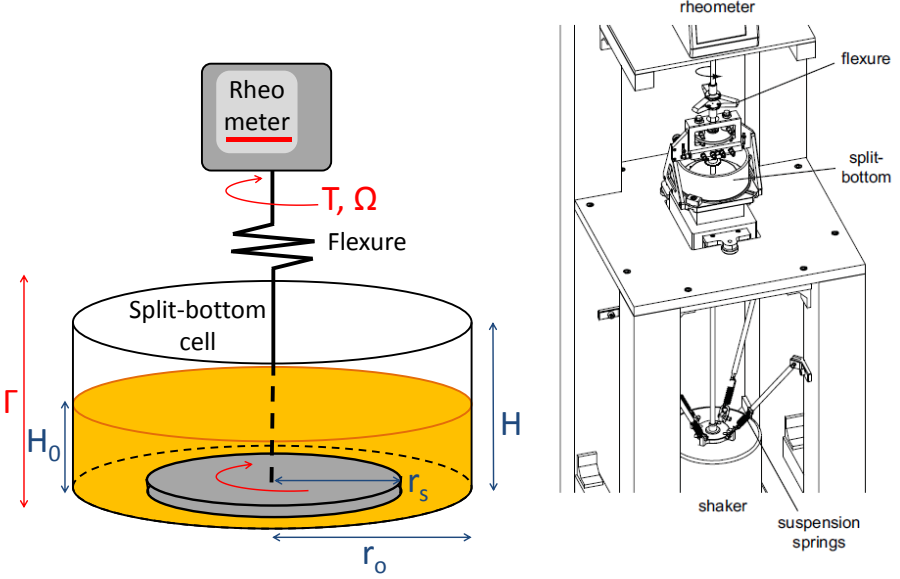


FIGURE 2.1: Left: Sketch of the vibrated split-bottom setup in which the rotation of a disk of radius  $r_s$  is used to probe the rheology of agitated granular media. The crucial experimental parameters are the relative filling height,  $H_0/r_s$ , vibration strength,  $T$ , the torque,  $T$ , and the rotation rate,  $\Omega$ . Right: Schematic 3D drawing of the setup including the bearings and the shaker. Figure adapted from [13].

the vertical coordinate  $z$  (trumpet flow), and the shear zone widens. Additionally, there is shear between horizontal layers (precession [77]), and the particles at the surface rotate with a lower angular velocity compared to the particles near the bottom. For very high filling heights, the particles at the surface no longer flow, and all the flow is located in a “dome” below the surface.

At slow driving rates, because of symmetry, the experiments can also be performed by rotating the side wall and outer bottom disk, keeping the inner bottom disk stationary.

The split-bottom flow geometry has been studied extensively and produces wide shear zones, and smooth, robust, and well-controlled granular flows [38, 46, 76–85].

**Particles and Conditions** – The container is filled with particles (black soda-lime glass beads, Sigmund Lindner 4504-007-L), a polydisperse mixture with a diameter between 1 and 1.3 mm, and a bulk density  $\rho$  of  $1.7 \times 10^3 \text{ kg/m}^3$ , up to a filling height  $H_0$ . To ensure good reproducibility, we use the total mass of the particles to control  $H_0$ . We use black coated beads because those are easier to image than transparent ones.

All experiments are carried out under ambient temperature, pressure, and relative humidity. We have verified that our experiments are insensitive to relative humidities ranging from 6% to 55%. After several months of use, the black coating of the particles visibly deteriorates, and the rheological behavior becomes more sensitive to humidity. We therefore renew our particles on a trimonthly basis, and have found that our experiments reproduce well over the course of several years.

**Rheometer** – To drive the rotation of the bottom disk and to measure the flow properties of the system, we use a rheometer (Anton Paar DSR 301), which can be used both in stress control (imposing a torque  $T$  and measuring the resulting rotation rate  $\Omega$ ) and in rate control (impose  $\Omega$ , measure  $T$ ). The native mode of the rheometer is stress control. Therefore, rate-controlled experiments require a feedback loop to adjust the torque such that the desired  $\Omega$  is reached. The characteristic time of this feedback loop can be altered using the so-called *csr*-value of the rheometer.

The rheometer can apply a maximum torque of 200 mNm and a maximum rate of 1.66 rps. For comparison, at our maximum filling height, the yield torque is around 33 mNm.

We work with the rheometer using commercial Anton Paar software. This software limits the sample rate to approximately 100 Hz. To acquire data faster, the two analogue output ports are used to read out the torque, rotation rate, or disk deflection angle  $\theta$  at a time resolution of 15 kHz.

**Vibrations** – We shake the system with a sinusoidal oscillation  $A \sin(2\pi ft)$ , with a fixed  $f$  of 63 Hz, using an electromagnetic shaker (VTS systems VG100). The amount of vibrations is characterized by the dimensionless parameter  $\Gamma = A(2\pi f)^2/g$ , where  $g$  is the gravitational acceleration. To set  $\Gamma$ , we use a feedback loop built around an accelerometer (Dytran 3120A), and a lock-in amplifier (SRS SR830 DSP), which is executed by software which is developed using LabVIEW. By time-averaging,  $\Gamma$  can be

controlled very accurately with an error in  $\Gamma$  of around  $10^{-3}$  [13].

**Coupling** – To protect the rheometer against the vibrations, we mount a flexure in the driving axis which is soft ( $1.4 \times 10^2$  N/m) in the vertical direction, but stiff (0.6 Nm/rad) in the rotational direction. The driving axis is fixed with air-bearings (see Fig. 2.1(b)). We avoid using bearings that have mechanical contact with the axis, as that would significantly contribute to the torque. Because the air-bearings can never be perfectly aligned, there is a  $T$ -offset of about 25  $\mu$ Nm.

**Imaging** – We image the surface of the system using a mirror and a Foculus FO114B camera. This allows us to extract the surface flow using particle image velocimetry.

**Filling Height** – As explained above, in the absence of vibrations, the phenomenology of the flow is determined by the dimensionless filling height  $h \equiv H_0/r_s$  [76]. In our experiments, we stay in the low filling height regime ( $h \leq 0.6$ ), where the shear bands are mainly vertical, and all grains above the disk corotate along with it. We have found that in all, but one, flow regimes, the flow profiles observed at the free surface are insensitive to the magnitude of vibrations. For the exception - which is for slow flow and strong vibrations - see Sec. 3.4.3.

**Crystallization** – In our experiments, there never is crystallization of the particles. The main reason for this is our particle polydispersity. Moreover, even for monodisperse particles, crystallization does not occur at all shaking frequencies and amplitudes [86].

**Protocol** – In order to obtain reproducible starting conditions, we subject the packing to a preshear before each experiment. The protocol consists of the following amounts of shear: (i) 10 s of 1 rps clockwise; (ii) 20 s of 1 rps counterclockwise; (iii) 10 s of 1 rps clockwise. After this preshear, we wait 10 s before starting the experiment in the clockwise direction. During the preshear and the wait time, the system is already subjected to vibrations. After the wait time, we start the experiment where we either measure  $\Omega(T)$  (stress control), or  $T(\Omega)$  (rate control).

## 2.3 Phenomenology

This section describes the previous results that were published in Ref. [71].

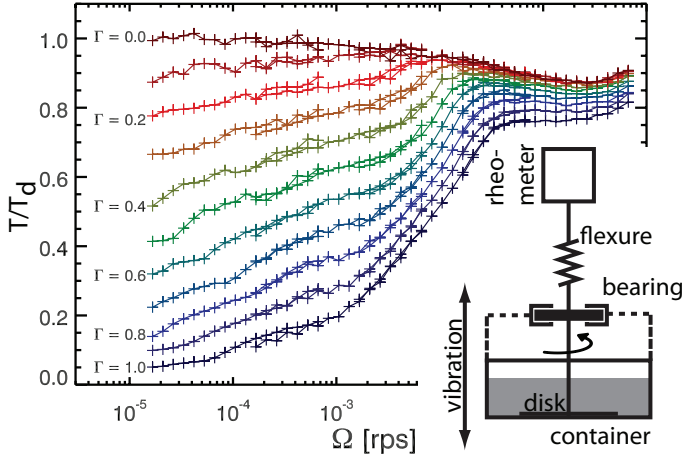


FIGURE 2.2: The flow curves that were measured in rate control for  $0 \leq \Gamma \leq 1$  [71]. The  $T$ -axis is rescaled with the dynamic yield torque  $T_d$ .

### 2.3.1 $\Gamma = 0$

In Fig. 2.2, we show  $T(\Omega)$  flow curves that are measured in rate control for  $0 \leq \Gamma \leq 1$  [71], where the torque is rescaled by the dynamic yield torque  $T_d$  (here, as in Ref. [71],  $T_d$  is defined as the plateau value of  $T$  for low  $\Omega$  and  $\Gamma = 0$ ). On top, there is the flow curve for  $\Gamma = 0$ . It is not perfectly *rate-independent* but has a *negative slope* that leads to a dip of roughly 10% of the yield torque [87]. The implications of the negative slope are significant: when comparing the situation to pushing a broken car, the negative slope says that if you want the car to go *faster*, you should push *less*. The region of the flow curve that has a negative slope, is the regime that is unstable and unaccessible in torque-controlled experiments [87–89]. For  $\Omega \gtrsim 0.1$  rps, the inertial regime is reached and the slope becomes positive [90].

The shape of the  $\Gamma = 0$  flow curve qualitatively matches the behavior that is observed when tilting a layer of sand. The sand will make the (hys-

teretic) transition from no flow to fast flow when the static yield stress is reached. If the tilt angle is then decreased again, the sand will keep flowing. Only once the torque corresponding to the dip of the flow curve is reached, the sand stops flowing. If the flow curve would have been perfectly flat, it would have been possible to let sand flow arbitrarily slowly during this decrease of the tilt angle.

We do not exactly know what physically causes the negative slope. It could be related to the rejuvenation of friction, as results similar to this non-monotonic relation between stress and velocity are also found in friction experiments [87, 91, 92]. Alternatively, the negative slope could be the result of shear-induced self-fluidization. In this picture, the system is more fluidized for higher  $\Omega$ . So, in a certain flow regime, a lower  $T$  is required to reach a faster, yet more fluidized, flow. We will discuss this idea in more detail in App. 4.A.3.

### 2.3.2 $\Gamma > 0$

The flow curves for  $\Gamma > 0$  (also plotted in Fig. 2.2) *do* drop to low  $T$  for low  $\Omega$ , suggesting that the yield torque disappears when switching on the vibrations. This is hard to say with certainty for our data range, but we have never observed indications for flattening of the flow curves for low  $\Omega$ . For  $\Gamma \lesssim 0.8$ , the curve still has a regime with negative slope. This means that there are now two stable flow regimes, one for slow and one for fast flow. In between, there is an unstable range in  $\Omega$ . The size of this regime decreases with increasing  $\Gamma$ , and for  $\Gamma \gtrsim 0.8$ , the flow curves are monotonic.

The curves can also be considered from the point of view of  $\Omega$ . For fast  $\Omega$ ,  $T$  varies little with  $\Gamma$  as the fast inertial flow [93] dominates over the vibrations. The flow at intermediate flow rates is similar to the quasi-static flow regime that was thoroughly studied in the absence of vibrations [77–79, 94]. Besides these known flow regimes [6], the new regime is the one for low  $\Omega$ , where the vibrations now play a significant role.

### 2.3.3 Simplest Model

The simplest possible model to describe our system would be to describe the flow behavior in terms of friction where the friction coefficient  $\mu$  depends on  $\Gamma$ . For  $\Gamma = 1$ , the friction would vanish, and assuming  $\mu$  varies

linearly with  $\Gamma$ , the system would yield (or: makes the transition towards fast flow) for  $T \sim (1 - \Gamma)$ . We see that this simple model does not agree with our data. First, the yield stress seems to disappear completely for any finite  $\Gamma < 1$ , and we do observe slow but stable flow for  $T/T_y + \Gamma < 1$ . In addition, the transition to fast flow is significantly above  $T/T_y + \Gamma = 1$ .

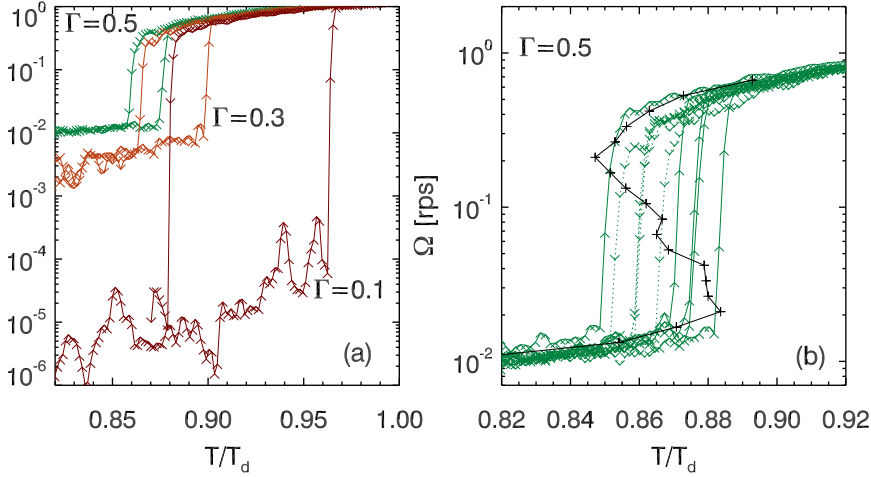


FIGURE 2.3: (a) Finite  $\Gamma$  hysteresis loops for  $\Gamma = 0.1, 0.3, 0.5$ . (b) Several hysteresis loops for  $\Gamma = 0.5$ , with the rheological data from  $\Gamma = 0.5$  from Fig. 2.2 overplotted in black. Image from [71].

### 2.3.4 Hysteretic Transition

The next step is to probe whether the negative slope regime of the flow curves for  $\Gamma > 0$  leads to hysteresis in torque-controlled experiments [71]. To do so,  $T/T_d$  is slowly ramped up and down between 0.8 and 1.1, *i.e.*, through the bistable regime. Fig. 2.3(a) illustrates the resulting hysteresis loops. Ramping upwards, a sudden jump is observed from the slow, mechanically agitated flow branch to the rapid, inertial branch. Ramping back down makes the flow rate jump back to the slow flow branch – there is considerable hysteresis between the stresses where these jumps happen. For smaller  $\Gamma$ , the gap between slow and rapid flow rates increases, con-

sistent with the flow curves shown in Fig. 2.2. In Fig. 2.3(b) the direct connection between the negative slope of the  $T(\Omega)$  curve and the hysteresis observed in the  $\Omega(T)$  curves is strengthened further for the example of  $\Gamma = 0.5$ . Several torque-controlled hysteretic data sets are combined with the appropriate flow curve. It can be seen that, while the precise location of individual hysteresis loops fluctuates, the characteristic torques remain confined to an interval which coincides well with the minimum and maximum of the  $T(\Omega)$  curve. We conclude that for  $\Gamma > 0$ , hysteresis and negatively sloped flow curves are directly related.





# VIBRATION DOMINATED FLOW IN WEAKLY VIBRATED GRANULAR MEDIA

---

In this chapter we describe the rheology of weakly vibrated granular flows as function of flow rate, vibration strength and pressure, by performing experiments in a vertically vibrated split-bottom shear cell<sup>1</sup>. For slow flows, we establish the existence of a novel vibration dominated granular flow regime, where the driving stresses smoothly vanish as the driving rate is diminished. We distinguish three qualitatively different vibration dominated rheologies within this slow flow regime, most strikingly a regime where the shear stresses are no longer proportional to the pressure.

## 3.1 Introduction

In chapter 2 we described how the rheology of weakly vibrated granular media reveals a variety of qualitatively different flow regimes. First, for large flow rates, inertial effects dominate, and the effect of vibrations is small. Second, for intermediate flow rates, we cross over to a regime similar to the well-known quasi-static flows that have been studied at length in the absence of vibrations [71, 76–79, 94]. Third, for even slower flows, we enter a regime where the vibrations lead to completely new rheological behavior.

The focus of this chapter is on these *vibration dominated flows*. By probing the equilibration times of the stresses and the variation of the steady state stresses with filling height, we find evidence for three qualitatively

---

<sup>1</sup>G. Wortel, J. Dijksman, and M. van Hecke, *Rheology of weakly vibrated media*, Phys. Rev. E **89**, 012202 (2014) [81]

different regimes. For slow enough flows, vibration effects increasingly dominate the physics, leading to compaction of the material for weak vibrations, and to fluidization of the material for vibrational accelerations approaching gravity. Most strikingly, in the latter regime, we see a breakdown of the proportionality of shear stresses and pressure, a highly unusual phenomenon in granular flows.

The outline of this chapter is as follows. In Sec. 3.2 we describe the measurement protocols used in the current and previous study [71]. In Sec. 3.3 we describe the main phenomenology of a complete set of experiments probing  $T(\Gamma, \Omega, h)$ . In Sec. 3.4.1 we introduce the canonical perspectives on granular rheology, including a model for the stresses in split-bottom flows by Unger *et al.* [95]. In Sec. 3.4.2 we use this model to extract effective friction coefficients from our data, as well as exploring the quality of the fit between the data and this model. In Sec. 3.4.3 we provide strong evidence for the existence of a pressure-independent flow regime through measurements of the flow structure.

## 3.2 Protocol

In this section we discuss our measurement protocols, and show how we ensure that we measure steady values for the rheology.

Our experiments focus on the rheological curves which relate the driving torque  $T$  and the driving rate  $\Omega$ . Our main focus is on experiments where we fix the driving rate in the range from  $10^{-4}$  to 1 rps, and probe the torque. We perform these experiments for a range of vibration amplitudes  $\Gamma = 0, 0.2, 0.5, 0.7, 0.83, 0.95$  and 1, and moreover use seven different filling heights ( $h = 0.19, 0.25, 0.31, 0.38, 0.44, 0.50$  and  $0.56$ ). Varying  $h$  allows us to probe the role of the confining pressure for the rheology.

Each experiment starts with switching on the vibrations, after which we allow the shaker feedback loop 30 s to settle to the required value of  $\Gamma$ . We proceed by applying an amount of preshear to the granular material, in order to obtain similar starting conditions for each experiment. Unless noted otherwise, the protocol consists of the following steps: (i) 2 s of 1 rps rotation clockwise; (ii) 4 s of 1 rps rotation counter-clockwise; (iii) 2 s of 1 rps rotation clockwise. (iv) 5 s without imposed stress or shear. (v) start of actual measurement. The rotation in the experiments is in the clockwise direction to minimize anisotropy effects [96].

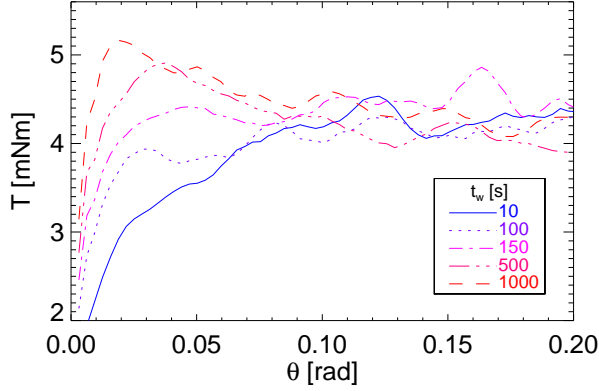


FIGURE 3.1: The torque as function of deflection angle  $\theta$  for  $\Omega = 10^{-4}$  rps,  $\Gamma = 0.7$ , and  $h = 0.31$ , but different waiting time  $t_w$  between the preshear and the actual measurement.

Vibrations lead to compaction of granular media, although this process is very slow for  $\Gamma < 1$  [58], whereas flow typically leads to dilatation [18]. Additionally, anisotropy in the fabric of the granular media needs a finite amount of strain to build up, but may be relaxed by vibrations [47, 96]. For both density and anisotropy, vibrations and flow are in competition, and as we are interested in steady state flow properties, we need to ask: what is the minimum time or strain necessary to get into a steady state flow regime?

We have probed the relaxation of our flows to a steady state by starting the flow from a denser or less densely packed state as follows: before each experiment, we perform preshear as described above. After preshear, during stage (iv), we stop the shear and vibrate the material for a waiting period  $t_w$ , during which the granular packing density increases by compaction, and then start the actual measurements. By varying the  $t_w$ , we thus manipulate the packing fraction at the start of the flow. By measuring the torque as function of time we capture the evolution of the torque to its steady state value. As we expect this equilibration to be slowest for small  $\Omega$  we perform this test at the smallest  $\Omega$  ( $10^{-4}$  rps) that we explore in our experiments. The results of this test are shown in Fig. 3.1, where we plot  $T$  as function of the total angle of rotation of the bottom disk  $\theta$ .

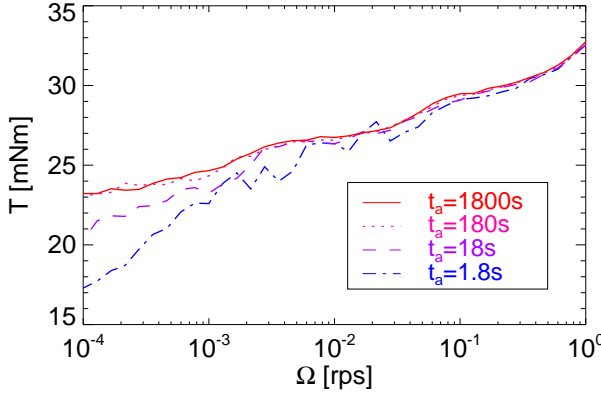


FIGURE 3.2: Flow curves for different averaging times  $t_a$ . Below  $\Omega \approx 0.5 \times 10^{-3}$  rps, the torque increases with the waiting time. The measurements are for  $\Gamma = 0.6$  and  $h = 0.56$ .

This figure shows that for small  $t_w$ ,  $T$  grows monotonically before reaching steady state, whereas for large  $t_w$ , the torque peaks at values larger than the steady state value. This is consistent with a simple picture where the longer the waiting time, the denser the grains are packed at the start of the experiment, and the larger the torque needed to cause flow.

For all waiting times, the torque reaches its steady state value for  $\theta < 0.1$  rad, corresponding to a measurement time of 150 s at  $10^{-4}$  rps. We claim that this represents the longest equilibration time necessary to reach a steady state flow situation, as all our experiments are carried out for  $\Omega \geq 10^{-4}$  rps. Moreover, in many experiments our data is acquired in a so-called strain rate sweep, where the rotation rate is varied by a small amount so that equilibration will be faster. In all cases, an equilibration strain or time of  $\theta > 0.1$  rad, or 150 s, will be sufficient to obtain steady state flow curves. We choose 180 s for all the experiments described in this chapter. Additional data that supports the claim that, also for lower  $\Gamma$ , a new steady state is reached within  $\theta < 0.1$  rad, can be found in Ref. [13].

To independently verify that equilibration times of 180 s are long enough, we perform a strain rate sweep at fixed  $\Gamma = 0.6$ . We sweep the flow rate from fast to slow rates, and then compare flow curves obtained for different times  $t_a$  per step, as shown in Fig. 3.2. While for small values of  $\Omega$

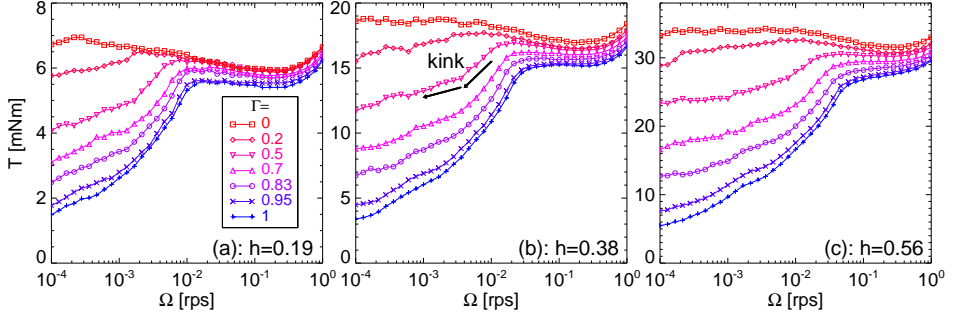


FIGURE 3.3: Selected flow curves for fixed filling height and varying  $\Gamma$ . In all cases,  $T$  decreases monotonically with  $\Gamma$ —its dependence on  $\Omega$  is more complex. The selected filling heights are  $h = 0.19$  (a),  $h = 0.38$  (b),  $h = 0.56$  (c).

and  $t_a$ , the torque shows a variation with  $t_a$ , for all the flow rates probed here we note that the data for  $t_a = 180$  s and 1800 s are indistinguishable, showing that for  $t_a \geq 180$  s the obtained values of  $T$  are steady state values. As a final additional test, we have also inspected  $T(t)$  to confirm we reach steady state [13].

### 3.3 Phenomenology

We now turn our attention to the rheological curves  $T(\Omega)$ . As shown in the  $T(\Omega)$  curves in Fig. 3.3, the flows in our system exhibit a rich rheology. There are two simple trends we see illustrated in these curves: increasing the filling height always increases  $T$ , whereas increasing the vibration strength always decreases  $T$ . The role of the flow rate is not as simple, with the torque often being a non-monotonic function of the disk rate  $\Omega$ —moreover, the details of the rheological curves depend on both the vibration strength  $\Gamma$  and filling height  $h$ . We note here that the sign of  $\partial T / \partial \Omega$  has a crucial rheological implication: flows for which  $\partial T / \partial \Omega > 0$  can also be accessed in experiments where the torque is fixed, whereas flows for which  $\partial T / \partial \Omega < 0$  are *unstable* in torque-controlled experiments. As we discussed in [71], this range of unstable flows leads to hysteretic switching between two different flow regimes when the torque is varied, and is deeply connected to the yielding behavior of granular media observed for  $\Gamma = 0$ .

Here we focus on rate-controlled experiments, and as a first step in characterizing these curves, we plot the boundaries between the regions where  $\partial T/\partial \Omega$  is positive and negative for three values of  $h$  in Fig. 3.4. Roughly speaking, we can distinguish three regimes.

**Inertial flows** — For  $\Omega \gtrsim 0.3$  rps,  $\partial T/\partial \Omega > 0$ ; the flow curves show an increasing  $T$  for increasing  $\Omega$ . This increase corresponds to the onset of the inertial regime [93]. To estimate the inertial number  $I = \dot{\gamma}d/\sqrt{P/\rho}$  at  $\Omega = 0.3$  rps, we have to choose a characteristic pressure and strain rate scale, as both  $\dot{\gamma}$  and  $P$  vary throughout the system. Taking  $P$  as the hydrostatic pressure at  $0.5H$ , and  $\dot{\gamma}$  corresponding to a shear band of three particles wide, we get  $I = 0.09$  for  $h = 0.38$  and  $\Omega = 0.3$  rps. Considering that the inertial regime typically starts at  $I = 0.1$  [90], there is good agreement between the onset of increasing  $T(\Omega)$  and the onset of the inertial regime. In the remainder of the chapter we will focus on slower flows.

**Unstable flows** — For intermediate flow rates,  $T(\Omega)$  has a negative slope for small  $\Gamma$ — for  $\Gamma \rightarrow 0$ , this regime extends to arbitrarily small flow rates, although there the flow curves become essentially flat. Despite the unsta-

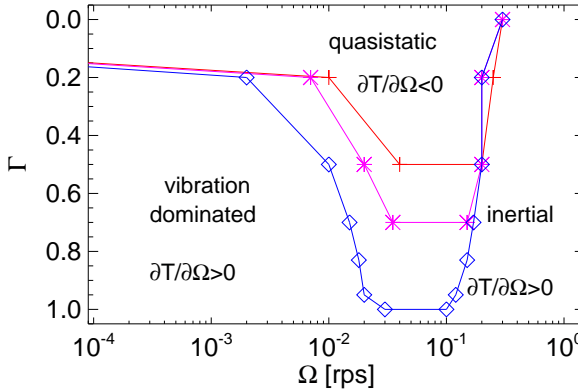


FIGURE 3.4: The boundaries between the regions where the flow curves have a positive and a negative slope for  $h = 0.19$  ( $\diamond$ ),  $h = 0.38$  ( $*$ ) and  $h = 0.56$  ( $+$ ). For  $\Gamma = 0$  and  $\Omega < 0.3$  rps, the flow curve always has a negative slope. The region extends to  $\Gamma > 0$ , and it extends to higher  $\Gamma$  for lower  $h$ .

ble character of the global rheology, and in contrast to unstable flows in *e.g.* micelles [61], we do not see any changes in the shear bands as we move in and out of this unstable regime. As the variation of the stress with flow rate is not very large, this regime can also be referred to as *quasi-static*.

**Vibration dominated flows** — Both the unstable/quasi-static and inertial regime have been studied in great detail already [36, 37, 66, 90, 94, 97], as they also arise in the absence of vibrations. Hence, in the remainder of the chapter we will focus on the new vibration dominated regime of slow, stable flows that arises for  $\Gamma > 0$  and  $\Omega < 10^{-2}$  rps.

One striking qualitative feature of this regime we already want to point out is the pronounced “kink” in the flow curves that can be seen for  $10^{-2} < \Omega$  [rps]  $< 10^{-3}$  in Fig. 3.3. In Fig. 3.3(b) we explicitly mark such a kink. The kinks coincide with the flow rates where  $t_a$  needs to be sufficiently large for  $T$  to equilibrate (see Fig. 3.2). We suggest that at sufficiently low  $\Omega$ , compaction effects become significant, leading to an increase of  $T$  with time, and a “kink” in the flow curves.

### 3.4 Vibration Dominated Flows

We will now turn our attention to the increase of  $T$  with  $h$ , which allows us to probe the underlying mechanisms that govern the rheology of vibration dominated flows. The canonical starting point of descriptions of *non-vibrated* slow granular flows is that the shear stresses  $\tau$  are proportional to the pressure  $P$  [66, 94, 97], and the ratio of  $\tau$  and  $P$  is an effective friction coefficient,  $\mu$ . For inertial flows, a description where  $\mu$  becomes rate dependent (through the inertial number) has been shown to capture much of the phenomenology [36, 37, 90], and for slow, non-vibrated flows, this Mohr-Coulomb picture combined with a non-local rheology captures the essentials of steady, slow granular flow [68–70].

By varying the filling height  $h$ , we can modify the pressure  $P$  and probe its role for the rheology in the different regimes. Here, we do not measure  $P$ , but assume it to be hydrostatic. Clear predictions for  $T(h)$  exist from a well-studied rheological model for the driving torques in a split-bottom geometry [95]. In addition, this model provides clues to the flow’s spatial structure and how it depends on friction and other factors. In this section, we describe how our experiments allow us to build on these

basic ingredients to identify two qualitatively different regimes in vibration dominated flows. We find a frictional regime in which  $P \sim \tau$ , yet with  $\mu(\Omega)$  a rate-dependent friction for  $\Omega \gtrsim 10^{-3}$  rps or  $\Gamma \lesssim 0.8$ . For even slower, more strongly vibrated flows, both the rheology and the location of the shear band presents strong evidence for a regime where  $T$  becomes *independent* of  $P$ .

### 3.4.1 Torque Minimization Model

To interpret the observed filling height dependence of the shear stresses, we start from a simple frictional model due to Unger *et al.*, which was developed to describe the three-dimensional shape of the shear zones in the split-bottom geometry, but which also makes a precise prediction for the driving torque as function of filling height for purely frictional flows [76, 77, 95]. This model is based on the following three ingredients. First, think of the shear zones as localized along a narrow sheet  $r(z)$  (corresponding to the center of the shear zones [76–79]). Second, assume that the stress tensor is collinear with the strain rate tensor [66] and proportional to the hydrostatic pressure. Third, assume that the sheet shape  $r(z)$  minimizes the driving torque<sup>2</sup>:

$$\tilde{T}[r(z)] = 2\pi g \rho \mu \int_0^H (H - z) r^2 \sqrt{1 + (dr/dz)^2} dz, \quad (3.1)$$

where  $g$  denotes the gravitational acceleration, and  $\rho$  the bulk density ( $1.7 \times 10^3$  kg/m<sup>3</sup>) of the granular material. Minimizing  $\tilde{T}$  for a given  $h$  determines the shear sheet  $r(z)$ , from which the torque can be determined as function of  $h$ . As expected, we can write this torque as  $\tilde{T}(h) = \mu \tilde{T}_f(h)$ , where  $\tilde{T}_f$  is a universal function of  $h$ . Note that for shallow filling heights, the torque is approximately proportional to the product of pressure and the extension of the shear band, so that  $\tilde{T}_f(h)$  is quadratic in  $h$  for  $h \ll 1$ .

In contrast to the original split-bottom cell for which Eq. (3.1) was developed, in our system the driving disk is slightly elevated with respect to the bottom. This is done in order to avoid observing spurious torque fluctuations that we associate with the diverging strain rate in the original split-bottom setup. We have found that the torques occasionally show

---

<sup>2</sup>Note that whereas we characterize the filling height with the dimensionless  $h$ , we write the frictional model in terms of  $H$ , which is the common notation.



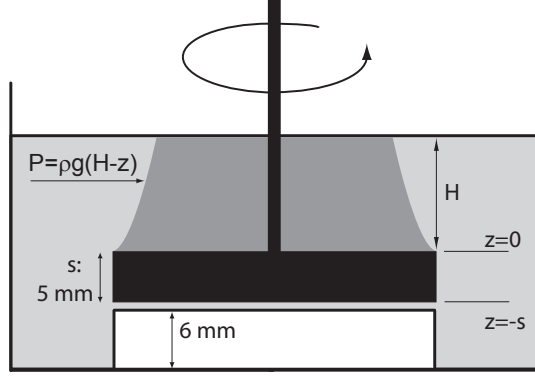


FIGURE 3.5: Schematic side view of the split-bottom setup. A cylinder of height 6 mm is placed underneath the disk, which has a thickness  $s$  of 5 mm and a radius  $r_s$  of 40 mm. The gray area represents the volume occupied by the grains; the dark gray region indicates the volume of particles corotating with the disk in the trumpet regime. The hydrostatic pressure  $P$  acts on the interface between the corotating and ‘static’ volume of particles as indicated. The side of the disk is also exposed to particles and, although smooth, contributes to dissipation during rotation as discussed in the text.

strong fluctuations in this case, presumably due to individual particle being trapped just above the split – moreover, these fluctuations depend on the precise roughness near the split, thus leading to a dependence of the average  $T$  on such experimental details. To avoid this, we make sure that the strain rate field is smooth at the grain level and have elevated the driving disk by 6 mm – see Fig. 3.5. The side of the disk is smooth, and particles immediately next to the disk hardly move, creating a static bottom layer flush with the disk. Hence, the boundary conditions are essentially the same as for the ordinary split-bottom disk, and the elevation does not affect the overall flow field for  $h \equiv H/r_s$  larger than about 0.1. The elevation does ensue that the torques are insensitive to experimental details and do not show the aforementioned spurious fluctuations.

The elevated disk does lead to a  $\mu$ -dependent addition in the experimental torque signal  $T$ , due to slip between the side of the disk and the

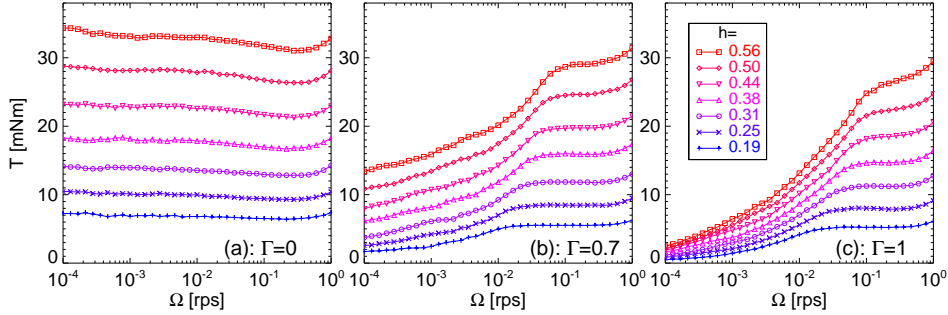


FIGURE 3.6: Selected flow curves for fixed  $\Gamma$  and varying  $h$ . In all cases,  $T$  grows monotonically with  $h$ . The selected values of  $\Gamma$  are: (a)  $\Gamma = 0$ , (b)  $\Gamma = 0.7$  and (c)  $\Gamma = 1$ .

stationary particles next to it. This drag term can be estimated as:

$$T_{\text{drag}}(H) = 2\pi r_s^2 \mu \rho g \int_0^s (H + z) dz, \quad (3.2)$$

where  $s$  is the disk thickness (5 mm), and  $\mu$  is the effective friction coefficient for sliding of the disk past the particles, for which we use the same effective friction coefficient as for the granular flow. The contribution of  $T_{\text{drag}}$  to the torque varies with  $H$  and is proportional to  $\mu$ , so that we can write  $T_{\text{drag}} = \mu T_d$ , where  $T_d$  can be deduced from Eq. (3.2).

We conclude that the measured torque  $T$  is composed of two contributions:

$$T = \tilde{T}(H) + T_{\text{drag}} = \mu \left[ \tilde{T}_f(H) + T_d \right] = \mu T_f, \quad (3.3)$$

so that, we can extract  $T(h)$  from our flow curves, and check whether the flow appears frictional, and if so, determine  $\mu$  [80] and  $\tilde{T}(h)$ .

### $\Gamma=0$

In Fig. 3.6(a) we show flow curves for  $\Gamma = 0$  and a range of  $h$ . Clearly, the torque only weakly varies with  $\Omega$  and we expect the stresses to be frictional. For each fixed  $\Omega$ , we extract  $T(h)$  from our data and fit it to  $\mu T_f$  (Eq. (3.3)), as shown in the inset of Fig. 3.7. We find that this fit is excellent, which implies that the stresses are frictional, and which allows us to extract  $\mu(\Omega)$ . As shown in Fig. 3.7,  $\mu(\Omega)$  is almost flat, and has the

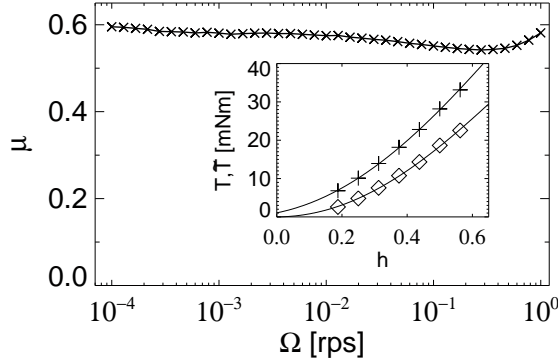


FIGURE 3.7:  $\mu(\Omega)$  as obtained from the fit with the frictional model. The inset shows one example of the fit for  $\Omega = 8.5 \times 10^{-4}$  rps. The upper curve (+) shows the raw data  $T$ , the bottom curve ( $\diamond$ ) is the raw data minus the correction term,  $\tilde{T}$  – which goes through the origin. The fit matches the data very well resulting in a  $\chi^2$  of  $2.0 \times 10^{-3}$  for the upper curve (see Eq. 3.4).

same shape as the flow curves. We stress here that  $\mu(\Omega)$  together with the frictional model predicts the stresses for *all* values of  $h$ , thus representing all the flow curves taken at different  $h$ . We note that our values for  $\mu$  are comparable to those found previously in a standard split-bottom cell using the same particles [76].

### 3.4.2 Frictional Model for $\Gamma > 0$

In Fig. 3.6(b) and Fig. 3.6(c) we show examples of flow curves for a range of  $h$  and  $\Gamma > 0$ . We will now use  $T(h, \Gamma > 0)$  to test if the basic assumptions for the Unger model break down in the vibration dominated regime. We will find two flow regimes with the distinguishing features  $T \sim \mu(\Omega)P$  and  $T \sim \mu P$ . We describe here how we can distinguish these regimes in the rheological data.

From Fig. 3.6(b-c) we see that the flow curves for  $\Gamma > 0$  all show significant rate dependence. Even so, we attempt to fit Unger's model to the rheological data. We thus fit  $T(h, \Omega)$  to try to obtain a  $\mu(\Omega)$ . If this rate dependence were captured by an effective friction coefficient that depends only on  $\Omega$ , with  $T(h, \Omega) = \mu(\Omega)T_f(h)$ , the rate dependence would lead to

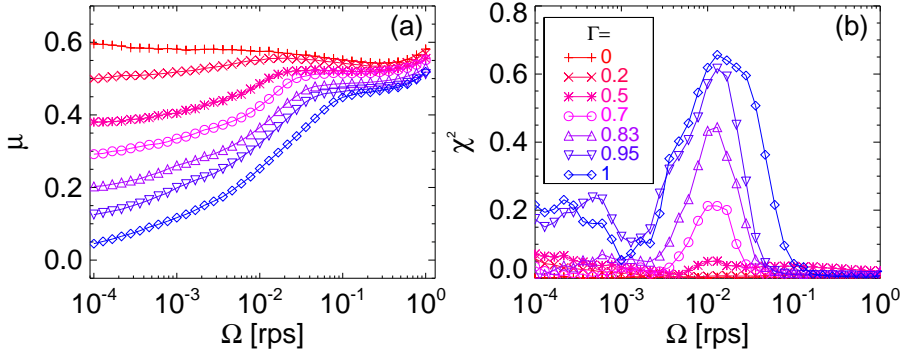


FIGURE 3.8: (a) The effective friction coefficient  $\mu(\Gamma, \Omega)$  as found by fitting the data with Eq. 3.3. Instead of plotting an arbitrary,  $h$ -dependent,  $T$ , we now assign a dimensionless  $\mu$  to each combination of  $\Omega$  and  $\Gamma$ . As expected, the curves have similar shape as the traditional  $T(\Omega)$  flow curves, indicating that  $\mu$  decreases with increasing  $\Gamma$  and decreasing  $\Omega$ . (b) The  $\chi^2$  of the fits, as defined in Eq. 3.4. There are two clear regions where the fit does not correspond well to the data.

a good fit of our data to the frictional model. To quantify the deviations between the data and fits to the frictional model, we calculate the best estimate of  $\mu$  and the corresponding  $\chi^2$  as follows. For each fixed  $\Omega$  and  $\Gamma$ , we have measured the torque for seven values of  $h$ , and then determine:

$$\chi^2 := \langle (\mu T_f(h) - T(h))^2 \rangle / \sigma_{T(h)}^2, \quad (3.4)$$

where  $\chi^2$  is a standard measure to quantify the quality of a fit, and  $\sigma_{T(h)}^2$  is the variance of  $T(h)$ . We apply this procedure for each value of  $\Omega$  and  $\Gamma$ , and show the result for  $\mu$  and  $\chi^2$  of these calculations in Fig. 3.8. For  $\Omega > 0.3$  rps - the inertial regime - the fit works very well and results in a weakly rate-dependent  $\mu$ , just as for  $\Gamma = 0$ . In addition, we find a large region for  $\Gamma \leq 0.83$  and  $\Omega < 0.5 \times 10^{-3}$  where the fit also works well, but this time with a more strongly rate-dependent effective friction  $\mu(\Omega)$ . This tells us that even in this rate-dependent, vibration dominated regime, a frictional prediction is perfectly capable of describing the flow.

We do however observe two distinct regimes where  $\chi^2$  is large, indicating a poor fit. First, there is a significant peak in  $\chi^2$  around  $\Omega = 10^{-2}$  rps for  $\Gamma \geq 0.7$ . Second, for  $\Gamma \geq 0.95$  and  $\Omega < 10^{-3}$  rps,  $\chi^2$  also is substan-

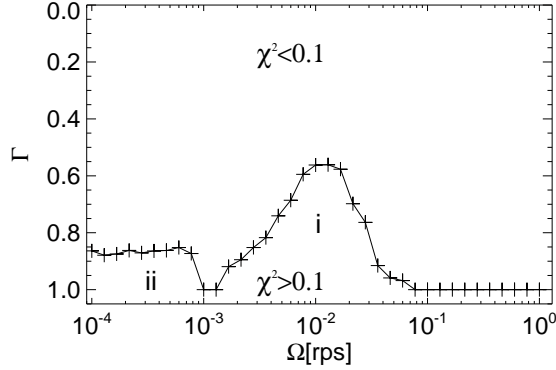


FIGURE 3.9: The boundary of  $\chi^2 = 0.1$ , where we interpolate  $\chi^2(\Gamma)$  to find the location of the boundary. The two distinct regions where the data does not agree with  $T_f(H)$  (i and ii) can clearly be seen. In the next sections we will see what causes the deviations from the frictional model in these two regimes.

tial. The two regimes are also clearly visible in Fig. 3.9 where we plot the boundary between a good fit ( $\chi^2 < 0.1$ ) and a bad fit as a function of  $\Omega$ .

The underlying physics in the two regimes is different. As we will show in the next section, the first peak is associated with a broad crossover regime between rate-dependent and rate-independent flows – a direct consequence of the flow profiles in the split-bottom geometry. The second peak we associate with a flow regime in which the rheology becomes pressure independent, as shown in Sec. 3.4.3.

### Onset of Rate Dependence

The peak in  $\chi^2$  around  $\Omega = 10^{-2}$  rps is consistent with the onset of rate dependence below  $\Omega = 10^{-2}$  rps as per the following reasoning. First, both our raw data for  $T$  as well as the best fits for  $\mu$  show that rate dependence sets in rather abruptly for  $\Omega < 0.1$  rps, and that rate dependence is strongest for large  $\Gamma$ , consistent with the location and strength of the peak in  $\chi^2$ . Crucially, this onset of rate dependence sets in at different flow rates for different heights (see Fig. 3.6), so that at a given  $\Omega$ , the data for  $T(h)$  mixes rate-independent and rate-dependent flows.

In Fig. 3.10(a) we show examples of  $T$  as function of height, that illustrate that when  $\Omega$  enters this rate-dependent regime,  $T(h)$  strongly de-

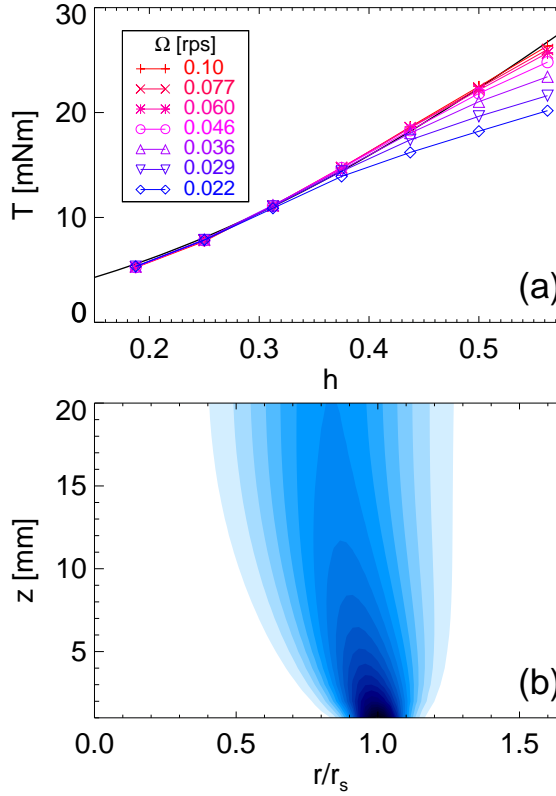


FIGURE 3.10: (a)  $T(h)$  for  $\Gamma = 0.95$  and a range in  $\Omega$  at the point where the rate dependence starts. It can be seen that the curve drop for high  $h$ , resulting in an s-shaped  $T(h)$  curve rather than an upwards curved  $T_f$  one. The black line is the fit with the frictional model to the top curve. (b) A theoretical prediction of  $\dot{\gamma}/\Omega$  -which decreases with  $z$ - in the split-bottom cell [76, 85]. The color is scaled linearly from high  $\dot{\gamma}/\Omega$  (dark) to low  $\dot{\gamma}/\Omega$  (light).

viates from the quadratic form predicted by Eq. (3.3). To interpret this deviation, it is important to realize that at a given  $\Omega$ , the local strain rate  $\dot{\gamma}$  spans a wide range of values and has a strong  $z$  dependence [76, 85, 95] – see Fig. 3.10(b). Hence, as the torque  $T$  is an integral over the local stress in different layers in the material,  $T(\Omega)$  mixes different local rheologies. More precisely: under the assumption that rate dependence sets in below a given  $\dot{\gamma}$ , there is a range of values of  $\Omega$  for which the lower part of the sys-

tem (where strain rates are largest) is still rate independent, whereas the top part of the system (where strain rates are smallest) are already rate dependent. This is consistent with the "drop" in the  $T(h)$  curves at large  $h$  shown in Fig. 3.10(a) – the deviations from the Unger model emerge first for large  $h$ , for which the range of strain rates is biggest and regime mixing is thus most pronounced. Our data also shows that once  $\Omega$  is sufficiently low, so that all of the material is in a rate-dependent state,  $T(h, \Omega)$  is close to  $\mu T_f(h)$  so that  $\chi^2$  drops to low values again, and  $\mu$  can be replaced with a rate-dependent  $\mu(\Omega)$ . The range of  $\Omega$  over which this crossover exists broadens with  $\Gamma$ , since the rate dependence becomes stronger with  $\Gamma$ .

In conclusion, the lowering of the friction coefficient  $\mu$  and the peak in  $\chi^2$  around  $\Omega = 0.01$  rps are caused by the onset of rate dependence which occurs at different  $\Omega$  for different vertical locations in the flow cell. For  $\Gamma \lesssim 0.8$ , we also observe that once all the material is in the slow, rate-dependent regime, the fit to the frictional model achieves a low  $\chi^2$  again, so that  $T(h, \Omega) \approx \mu(\Omega)T_f(h)$ .

### 3.4.3 Fluidized Region

The growth of  $\chi^2$  for large  $\Gamma$  and low  $\Omega$  signals a breakdown of the frictional picture, where shear stresses are proportional to the pressure, as we will describe in this subsection. To gain deeper insight in the flow phenomenology in this regime, we plot  $T(h)$  for  $\Gamma = 1$  and a range in  $\Omega$  in Fig. 3.11. We see that for all filling heights the stresses drop with  $\Omega$ , and at low  $\Omega$ ,  $T(h)$  becomes approximately *linear*. The standard Unger model predicts a quadratic dependence of  $T(h)$  on  $h$ , as mentioned above. A linear dependence would suggest a pressure-independent rheology, for which the increase of  $T$  with  $h$  is due only to increasing surface area on which the shear stress acts. Note that the large values of  $\chi^2$  here cannot be due to the existence of a crossover regime, as presented above for  $\Omega \approx 10^{-2}$  rps. Evidence for this comes from Fig. 3.6(c), which shows that both rate dependence of  $T(\Omega)$  is small, and that there is no strong difference in the rate dependence for different values of the height in this regime. First of all, that means that there is little mixing of different rheologies in the global torque signal; second, the rate dependence is weak, so even if there were some mixing, it would not produce a strong  $h$  dependence.

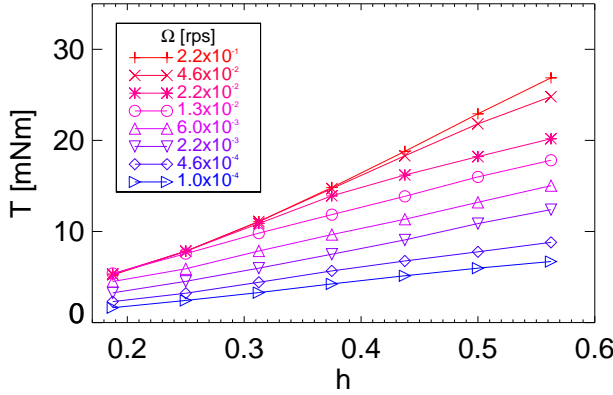


FIGURE 3.11:  $T(h)$  curves for  $\Gamma = 1$  and  $\Omega < 10^{-3}$  rps. Towards lower  $\Omega$ , the curves lose their curvature and become straight lines.

It is perhaps not surprising that new phenomena occur around the special value  $\Gamma = 1$ . For  $\Gamma \approx 1$ , the grains lose contact during part of the vibration cycle – the precise value of  $\Gamma$  where this happens depends on details [98, 99]. As a result, the confining pressure becomes zero during part of the cycle, and as most slip can be expected to occur when the normal grain forces are absent, the flows may become pressure independent, as in a viscous liquid.

### Rate Dependent Flow Structure

Additional evidence for the loss of pressure dependence for high  $\Gamma$  and low  $\Omega$  comes from measurements of the flow structure. From finite element calculations on the flow structure of a viscous liquid in the split-bottom geometry, it is known that the shear band is much closer to the center of the cell than for frictional flow [80]. As such, a pressure-independent rheology for the granular flows in this regime can be expected to be accompanied by similar changes in the flow structure.

To test this, we measured the velocity profiles  $\omega(r)$  at the surface of our system for a range in  $\Gamma$  and  $\Omega$  using particle image velocimetry [76–79]. In Fig. 3.12(a) we show examples of  $\omega(r)$ , showing a broadening and shift of the shear zones when  $\Omega$  enters the pressure-independent regime. We



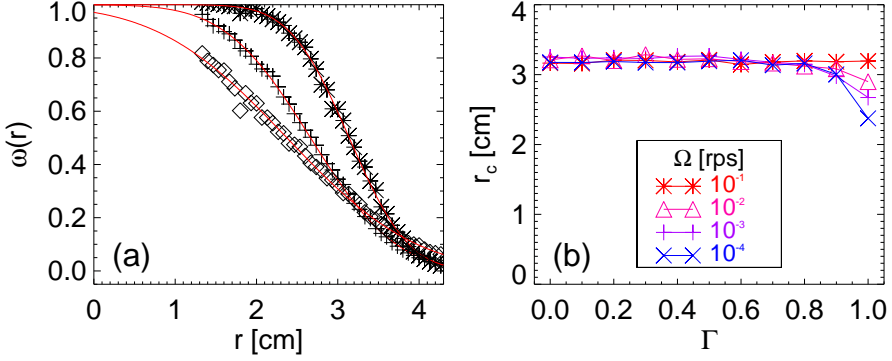


FIGURE 3.12: (a)  $\omega(r)$  for  $\Omega = 10^{-1}$  rps,  $\Gamma = 0.2$  ( $\times$ ),  $\Omega = 10^{-3}$  rps,  $\Gamma = 1$  ( $+$ ),  $\Omega = 10^{-4}$  rps,  $\Gamma = 1$  ( $\diamond$ ). In red, we add the fit with  $\omega(r) = 1/2 - 1/2 \operatorname{erf}[(r - r_c)/W]$ . (b) The center of the shear band at the surface  $r_c$  as a function of  $\Gamma$  for  $h = 0.47$  and  $\Omega$  as indicated. For low  $\Omega$ ,  $r_c$  clearly decreases.

fit the velocity profiles with  $\omega(r) = 1/2 - 1/2 \operatorname{erf}[(r - r_c)/W]$ , where  $r_c$  is the center of the shear band at the free surface [79].

In Fig. 3.12(b), we plot  $r_c$  for  $\Omega$  ranging from  $10^{-1}$  to  $10^{-4}$  rps and a range in  $\Gamma$ . Clearly, the location of the shear band is mostly independent of  $\Omega$  and  $\Gamma$ , including most of the rate-dependent regime. However, in the regime where we observed the pressure-independent rheology, we observe significant deviations in the flow profiles. The deviations show a trend towards a shear band moving inwards – consistent with the idea of a pressure-independent regime.

Moreover, we can modify the Unger model to test which rheological scenario is most compatible with the observed shift in the shear band. Throughout, we assume that the torque minimization principle is robust. The frictional torque model assumes  $\sigma(z) \sim 1 - z/H$ , in which the shear stress, being proportional to the hydrostatic pressure, goes to zero at the surface. We can replace this model with  $\sigma(z) \sim 1 - (1 - \alpha_1)z/H$ , in which the shear stress reaches a final value when approaching the free surface – see Fig. 3.13(a). The extreme case  $\alpha_1 = 1$  represents a pressure-independent rheology. We compute the location of the shear band at the free surface as a function of model parameter  $\alpha_1$ . The results are shown in Fig. 3.13(b). We find that for larger  $\alpha_1$ , the location of the shear band at the free surface moves inwards. Thus, the closer the model resembles

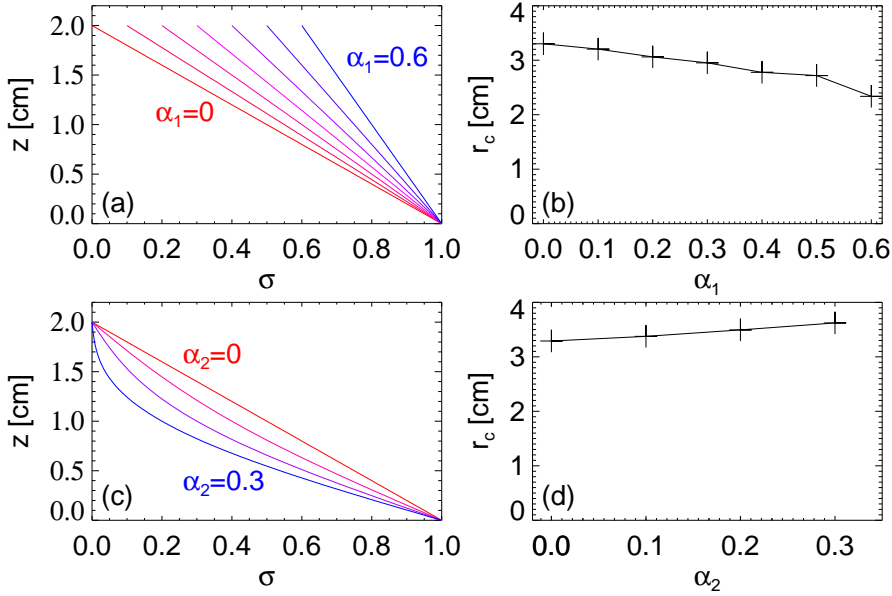


FIGURE 3.13: The center of the shear band at the surface,  $r_c$ , can be found using the method by Unger for given  $z$ -dependent stress  $\sigma(z)$ . In (a), we plot  $\sigma(z)$  for case  $\sigma(z) \sim 1 - (1 - \alpha_1)z/H$  where  $\sigma$  is still finite at  $z = H$ , in contrast to the frictional description where  $\sigma(H) = 0$ . The resulting  $r_c$  is shown in (b), we recover an inwards moving shear band as we observe in experiments. In (c) we plot  $\sigma(z)$  for  $\sigma = (1 - z/H) + \alpha_2 \sin[2\pi z/(2H)]$ , where  $P$  and  $\mu$  respectively vanish and decrease towards the surface, corresponding the a strain rate-dependent frictional picture, as we show in (d), this predicts an outwards moving shear band, contrary to what we observe.

a Newtonian rheology, the more the shear band moves towards the center. This can be understood intuitively as follows: the penalty for having a shear band at large radius at the surface is zero in the pressure-dependent model, because the shear stress goes to zero at the free surface. Once a finite amount of shear stress is present in the shear band at the surface, torque minimization will move the shear band inwards precisely as we observe in the experiments at  $\Omega < 10^{-3}$  rps,  $\Gamma > 0.9$ .

Conversely, for a frictional, rate-dependent rheology, the shear stress closer to the surface is *lower* than that of a simple frictional model. We

model this with a  $\sigma(z)$  that can be captured with:

$$\sigma = (1 - z/H) + \alpha_2 \sin[2\pi z/(2H)] , \quad (3.5)$$

as shown in Fig. 3.13(c). The torque penalty for having a shear band at finite  $r$  is thus reduced, and the model predicts indeed an *increase* of the shear band radius at the free surface (Fig. 3.13(d)), contrary to what we observe. We thus conclude that our observation of the inward displacement of the shear band location at  $\Omega < 10^{-3}$  rps,  $\Gamma > 0.9$  is consistent with the granular flow obtaining a rheology which becomes pressure independent.

### 3.5 Conclusion

To summarize, we probe the rheology of weakly vibrated granular media and find several different flow regimes. First, for  $\Omega > 0.3$  rps, our data shows the well-known *inertial flow* regime. In the absence of vibrations, lower flow rates lead to an essentially rate-independent, *quasi-static*, regime, where the variation of the torque is small, and where  $T(h)$  is well fitted using Eq. (3.3), implying that the shear stresses are proportional to the pressure here. For  $\Gamma = 0$ , this regime covers all  $\Omega < 0.1$  rps, whereas the range of flow rates where this rate-independent regime resides shrinks in the presence of vibrations, and almost vanishes for  $\Gamma = 1$ . For  $\Omega$  below the rate-independent regime and  $\Gamma > 0$ , we have described three *vibration dominated* regimes. For two of these regimes, our data shows that the shear stresses are still proportional to the normal stresses, but now via rate-dependent  $\mu(\Omega)$ . For the slowest of these two regimes, we see a slow densification, leading to a kink in the flow curves. Finally, for  $\Gamma$  close to one, the vibrations affect the rheology of the granular medium so significantly, that the shear stresses are no longer proportional to the normal stresses, signifying a complete departure of the frictional nature that is a hallmark of all other types of slow granular flows.



# A NONTRIVIAL CRITICAL POINT IN GRANULAR FLOWS

---

## 4.1 Introduction

In this chapter we investigate the transition between slow and fast granular flows in the weakly vibrated split-bottom geometry. As we have seen in chapter 2, this transition is hysteretic in stress-controlled experiments at low vibration strength  $\Gamma$ .

To see how the transition develops with increasing  $\Gamma$ , we show a collection of flow curves in Fig. 4.1. The red curves on top correspond to low  $\Gamma$ , and the negative slope part around  $\Omega = 0.1$  rps reflects the hysteretic regime. With increasing  $\Gamma$ , the magnitude of the hysteresis decreases. For  $\Gamma_c \approx 0.43$ , the flow curve no longer has a negatively sloped part, but instead contains an essentially flat part. At this plateau, there is a large range in  $\Omega$  that corresponds to a very narrow range in torque around the critical torque  $T_c$ . For  $\Gamma > \Gamma_c$ , the flow curves are monotonic.

In this chapter we will explore the idea that  $(\Gamma_c, T_c)$  is similar to a second-order critical point. If we identify the flow curves with the variation of an order parameter ( $\log(\Omega)$ ) as a function of two control parameters  $(T, \Gamma)$ , then these curves are analogous to the well-known  $(P, V)$  curves for the gas-liquid transition, which are given by the van der Waals equation [100]. Water can be turned into vapor via a first order phase transition by decreasing the pressure  $P$  at low temperatures. Here, the order parameter which distinguishes the fluid phase from the gaseous phase is the volume  $V$ . At a certain higher temperature  $T_c$ , the transition becomes continuous at the second-order critical point  $(T_c, P_c)$ . To make our analogy concrete, we associate the temperature with the vibration amplitude

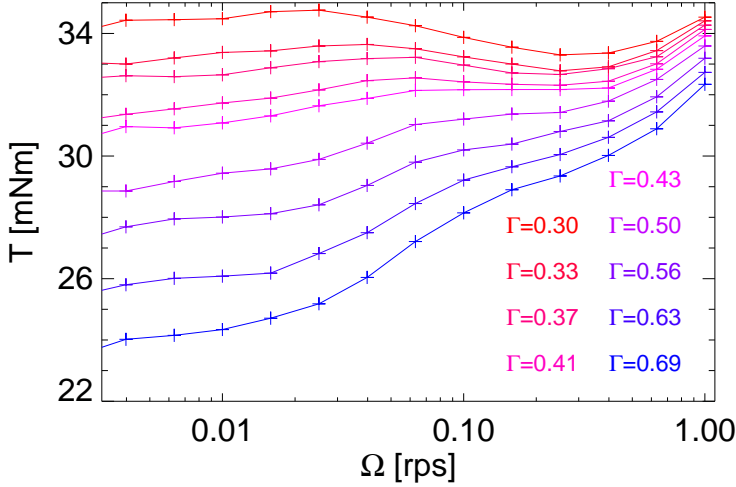


FIGURE 4.1: Examples of flow curves for different  $\Gamma$ . In the crossover between the curves with a negative slope part (red) and the monotonic ones (blue), there is a curve for  $\Gamma \approx 0.43$  with an essentially horizontal plateau.

Vibrheology	Gas-Liquid	Ising Model
Vibration $\Gamma$	Temperature $T$	Temperature $T$
Torque $T$	Inv. Pressure $P^{-1}$	Inv. Magnetic Field $H^{-1}$
Flow rate $\Omega$	Volume $V$	Inv. Magnetization $M^{-1}$

TABLE 4.1: Comparison of the control and order parameters between our system, the gas-liquid transition, and the Ising model.

$\Gamma$ , the inverse pressure with the torque  $T$  and the inverse volume with the rotation rate  $\Omega$ <sup>1</sup>. At low  $\Gamma$ , there is a discontinuous transition from slow to fast flow as  $T$  is increased. By choosing the correct combination  $(T_c, \Gamma_c)$ , our flow transition becomes continuous. In Table 4.1, we summarize the mapping between our system and the gas-liquid transition, as well as the comparison to the Ising model [101, 102]. At this point, this is a purely an analogy.

<sup>1</sup>We denote the rotation rate with  $\Omega$  if it concerns a control parameter or a time averaged value and with  $\omega$  if it is a time-dependent order parameter.

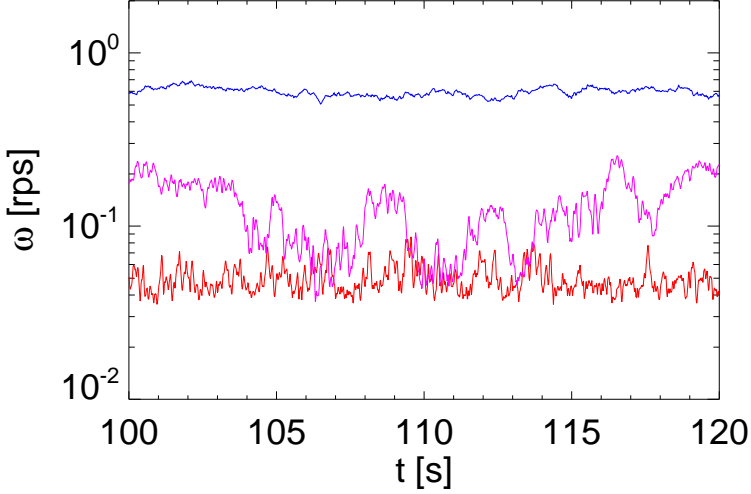


FIGURE 4.2: Three  $\omega(t)$  signals for  $\Gamma$  just above  $\Gamma_c$  for  $T < T_c$  ( $\Gamma = 0.71$ ,  $T = 30.1$  mNm, red),  $T \approx T_c$  ( $\Gamma = 0.71$ ,  $T = 31.0$  mNm, pink) and  $T > T_c$  ( $\Gamma = 0.71$ ,  $T = 31.6$  mNm, blue). The fluctuations are largest for the data set closest to the critical point.

To explore if the analogy to a critical point in our system is more than just a superficial coincidence, we will perform several experiments, both in rate and stress control.

First, we measure the flow curves  $T(\Omega)$  in rate control. We study in detail how the shape of the flow curves changes as we vary  $\Gamma$ . We will consider: (a) the scaling of the distance between the local minimum and maximum of the flow curves for  $\Gamma < \Gamma_c$ , that decreases when approaching  $\Gamma_c$ , and (b) the scaling of the slope at the inflection point, which goes to zero when approaching  $\Gamma_c$  either from above or below. We will find that the shape of the flow curves can very well be described using a mean field picture [103, 104], and the critical exponents we extract from the data are equal to the mean field values within error bars.

Second, in stress control we study the fluctuations in  $\omega(t)$ . If we impose  $\Gamma^* \equiv (\Gamma - \Gamma_c)/\Gamma_c \approx 0$  and  $T^* \equiv (T - T_c)/T_c \approx 0$  - which corresponds to the plateau in Fig. 4.1 - we expect to see large fluctuations in  $\omega$ . Moving away from the critical point, the flow curve gets steeper and we expect smaller fluctuations in  $\omega$ . Indeed, we will provide evidence for such a variation of the fluctuations.

In general, the packing can be thought of to possess an effective viscosity  $\eta$ , so that  $\omega = T/\eta(T)$ .  $T$  is constant in experiments where we probe the fluctuations in the flow rate, but the packing (and thus  $\eta$ ) continuously fluctuate. At the *flat* part of the flow curve, a tiny increase in  $T$  then leads to a large increase in  $\omega$ , which in turn corresponds to a large change in  $\eta$ . If the flow curve is *steep*, a change in  $\omega$  requires a large change in  $T$ . Based on this reasoning, we expect the magnitude of the fluctuations  $\sigma$  to be related to the slope of the flow curve via:

$$\sigma \sim \frac{1}{\partial T / \partial \Omega} . \quad (4.1)$$

For each  $\Gamma$ , we thus expect the fluctuations to be maximal at the inflection point  $(\Omega_i, T_i)$  of the flow curve, where the slope is smallest. We have explored Eq. 4.1 in detail and found that, indeed, the fluctuations increase monotonically as the slope of  $T(\Omega)$  gets flatter, but the prefactor depends on  $\Gamma$  and is different for the slow and fast flowing branch [105].

In Fig. 4.2, we show three  $\omega(t)$  curves for  $\Gamma$  just above  $\Gamma_c$  and  $T < T_i$ ,  $T \approx T_i$  and  $T > T_i$ . We see that the fluctuations are non-monotonic in  $T$  and are largest around  $T_i$ . We will find that, in general, the fluctuations increase if the critical point is approached either by changing  $T$  or  $\Gamma$ ; the corresponding critical exponent matches the mean field value.

Third, we study the characteristic time scale of the  $\omega(t)$  signals via their autocorrelation function. Whereas the lower curve in Fig. 4.2 fluctuates rapidly with a time scale significantly below 1 s, there is a longer time scale in the critical curve. We will find that the time scale increases if the critical point is approached either by changing  $T$  or  $\Gamma$ . Even though a precise single time scale is hard to identify, we conclude that the critical exponent for the divergence of the characteristic time scale deviates from the mean field value.

The outline of this chapter is as follows: in Sec. 4.2 we will explain in more detail how we perform the experiments, and in Sec. 4.3 we will explicitly introduce the scaling relations and exponents that we test in our system. In Sec. 4.4 we discuss the scaling of the flow curves, and in Sec. 4.5 we consider the magnitude and time scale of the fluctuations that are measured in stress control. We finish with an appendix, where we suggest a simple heuristic model to describe the flow in App. 4.A.3.



## 4.2 Setup and Protocol

To perform the measurements, we have developed an extended version of the setup that was introduced in Sec. 2.2. Our geometry has the complication that, because of the flexure, the angle  $\theta$  of the disk that drives the system is not necessarily the same as the angle measured by the rheometer. In the case of experiments at constant  $\Omega$ , we are not significantly hindered by this problem as we measure flow in *steady state*, where the deflection of the flexure also reaches a steady state value. For stress-controlled *fluctuation* measurements, the deflection of the flexure will vary, and the motion above and below the flexure will definitely not be the same. To circumvent this, we extended the setup by mounting an optical encoder just below the flexure - see Fig. 4.3 - which is thus rigidly connected to the disk.

In most encoders there is mechanical contact between the sensor and the rotating axis which results in a torque similar to the torques we want to measure. We therefore have specifically chosen an encoder in which there is no contact between these two parts.

The encoder (Heidenhain ERO 1285 - 2500) consists of a glass disk with 2500 engraved lines which is mounted on the axis of the system. Above the disk - attached to the cell itself and not to the axis - there is an LED and below the disk there are sensors that detect how much light shines through the disk. If there is a line between LED and detector, the sensor measures a lower light intensity. The light intensity is turned into a voltage, which is the raw output of the device.

The disadvantage of a non-contact encoder is that it has to be mounted very accurately. The distance between the sensor and the engraved disk is crucial and has to be  $0.2 \pm 0.03$  mm and may not vary much over a full rotation of the disk. To achieve this, we had to realign the entire setup and renew the driving axis. The aligning is done by reading out the

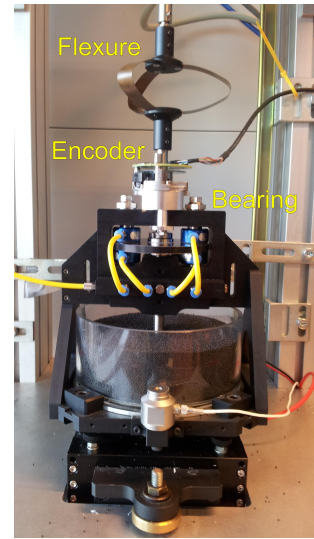


FIGURE 4.3: A photo of the shear cell with the new angular encoder.

raw sine signal of the encoder and by adjusting the alignment such that amplitude of the signal does not vary with  $\theta$ .

In case of a constant rotation rate, the output of the encoder has the shape of a sine wave with constant frequency. We use an interpolator (Heidenhain IBV 101) which extracts from each sine wave a series of 10 block pulses. This increases our resolution by a factor 10. There are two channels that measure the light through different spots of the disk, which is required to determine the direction of the rotation. We connect the two pulse signals we obtain from the interpolator to the counter ports on the DAQ I/O card, which can count pulses with frequencies up to 80 MHz. From the two pulse trains,  $\theta$  can be calculated via a standard method called “quadrature encoding” [106], which as a bonus gives an additional factor 4 in resolution (resulting in  $2500 \times 10 \times 4 = 10^5$  pulses per rotation).

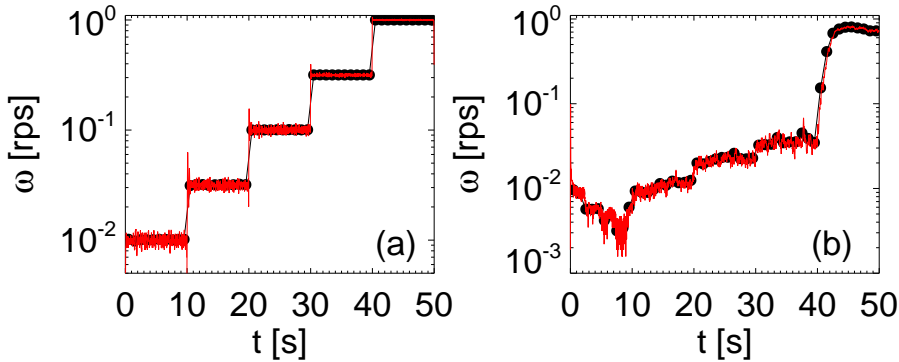


FIGURE 4.4: Comparison between  $\omega$  measured by the rheometer (black) and the encoder (red). In (a), we control  $\Omega$  at 5 different values, each for 10 s, in (b) we control  $T$ , also at 5 values, for 10 s. The encoder signal resolves more fluctuations because it measures the disk’s angle at much higher temporal resolution. For the encoder signal we measure the position of the disk using a temporal resolution of 63 Hz and obtain  $\omega$  by taking a three-point derivative. The good correspondence between the red and black data shows that the encoder works well in the  $\Omega$  range where we will measure.

The accuracy of an encoder depends on how constant the distance between the engraved lines on the disk is. An estimate for the accuracy is 10% of the grading, which in our case leads to 0.25 mrad [107]. How strongly this affects the error on the rotation rate, varies with  $\omega$  and the time resolution used in the experiment. To ensure that the encoder is ca-

pable of probing  $\omega$  in the full range where we will measure, we perform test experiments at both constant  $T$  and constant  $\Omega$  that cover the two relevant decades in  $\omega$ . We compare the output of the encoder with the numbers that are found by the rheometer and see that they correspond well – see Fig 4.4.

When reading out the encoder at 1 kHz, we observe a significant 63 Hz signal caused by the shaking at this frequency. Filtering out this signal is not trivial, since it is distributed over a frequency band around 63 Hz with a width of the order of 1 Hz, as well as over the higher harmonics. We therefore decide to read out the encoder stroboscopically with a sample rate of 63 Hz, where we use the sync output of the function generator that is used to control the shaker as a trigger to read out  $\theta$  (it triggers on the moment the sine goes through the equilibrium from negative to positive). This way, we always measure  $\theta$  in the same position of the cycle, thereby suppressing the spurious signal caused by the shaker.

### 4.2.1 Protocol

**Filling Height** – As shown in Fig. 3.3, the value of  $\Gamma_c$  depends on the relative filling height  $h \equiv H/r_s$ . The reason for this  $\Gamma$  dependence stems from the details of the flow structure, as explained in Sec. 3.4.2. For low  $h$ , we have observed that  $\Gamma_c$  becomes close to 1, which makes the range of monotonic flow curves we can study inconveniently small. Therefore, we choose a relatively high filling height,  $h = 0.6$ , which, as we know from exploratory stress-controlled experiments, results in  $\Gamma_c \approx 0.65$ .

**Control parameters** – We perform two different types of measurements.

First, we measure flow curves  $T(\Omega)$  in rate control to study the scaling of the shape of the flow curves around the critical point. To study the scaling of the flow curves, we measure a set of flow curves for  $0.3 \leq \Gamma \leq 0.7$  with  $\Delta\Gamma = 0.01$  and  $\Omega = 1.0, 0.63, 0.40, 0.25, 0.16, 0.1, \dots, 0.001$  rps in 16 logarithmic steps. We average each point for 180 s, which is long enough to reach the steady state – see Sec. 3.2.

Second, we measure  $\theta(t)$  in a stress-controlled experiment to probe the fluctuations in its derivative  $\omega$ , for a range of torques and vibration amplitudes which form a grid in  $(T, \Gamma)$ -space. If we want data that is suitable to accurately determine the scaling of the fluctuations with  $\Gamma^*$ , we have to be certain that the grid is closely centered around the critical

point. From test measurements in stress control we know that  $\Gamma_c \approx 0.65$  and  $T_c \approx 30.5$  mNm. We have taken two data sets. In data set 1, we choose our 20x20 grid with  $T$  going from 28.9 mNm to 31.75 mNm in steps of  $\Delta T = 0.15$  mNm and  $\Gamma$  going from 0.65 to 0.935 with  $\Delta \Gamma = 0.015$ . In data set 2, where we focus on what happens around the inflection points of the flow curves, we take  $\Gamma$  from 0.62 to 0.77 with  $\Delta \Gamma = 0.01$ , but different  $T$  values for each  $\Gamma$  around  $T_i$ . From exploratory measurements, we estimate that  $T_i$  [mNm]  $\approx 34.64 - 5.16\Gamma$  and we choose the ten  $T$ -values such that they surround  $T_i$  with  $\Delta T = 0.1$  mNm. In both data sets, we measure 40 min per  $(T, \Gamma)$  for good statistics and to be able to extract time scales up to a few minutes.

### 4.3 Theoretical Framework

By comparing the transition from slow to fast flow to the liquid-gas and the Ising ordered-disordered transitions, as shown in the mapping in Table 4.1, we obtain several predictions for the scaling behavior and values for the critical mean field exponents [108, 109].

**Parameters** – In this section we summarize the many parameters that we will use throughout this chapter. We denote the rotation rate by  $\Omega$  if it concerns a control parameter or a time averaged value, and by  $\omega$  if it is a time-dependent order parameter. When looking at scaling relations, we will quantify the flow rate with  $l \equiv \log_{10}(\Omega/1 \text{ rps})$ . Throughout this chapter we will see several examples that imply that  $l$  is the natural coordinate. For example, many properties of the system (for instance Eq. 4.2) scale with  $l$  via a power-law relation whereas the scaling in  $\Omega$  would take a more complex form.

For each  $\Gamma$ , the flow curve has an inflection point  $(T_i, l_i)$ . At the critical  $\Gamma_c$ , this is the critical point  $(T_c, l_c)$ . We define the reduced  $\Gamma^* \equiv (\Gamma - \Gamma_c)/\Gamma_c$  and  $T^* \equiv (T - T_i)/T_i$ , both of which are zero at the critical point (at the critical point,  $T_i = T_c$  and  $T^* \equiv (T - T_c)/T_c$ ).

**Flow Curves** – To examine the shape of the flow curves, we wish to determine their inflection points  $(T_i, l_i)$ , as well as the slope at these inflection points  $\chi^{-1} \equiv \partial T_i / \partial l_i$  and the distance between the local minimum and maximum,  $\Delta l$ , for  $\Gamma^* < 0$ . To obtain accurate values for  $T_i, l_i, \chi^{-1}$  and  $\Delta l$ ,

we do not wish to calculate numerical derivatives from our experimental data, but rather use simple polynomial fits. From the raw  $T(l)$ -curves that are shown in Fig. 4.5(a), we see that the shape of the flow curves around their inflection points is reminiscent of a third order polynomial, where the linear part dominates the inflection point and controls the slope around  $l_i$ . We therefore will fit the flow curves around the inflection point with:

$$T = a(l - l_i)^3 + \chi^{-1}(l - l_i) + T_i . \quad (4.2)$$

In the next section we will show that this fit is capable of fitting the flow curves in the region around the inflection point given by  $-1.6 < l < 0$ .

The susceptibility  $\chi$  of a system describes its response to an applied field and diverges at the critical point. However, since we consider  $T(l)$ , the slopes at our inflection points vanish towards the critical point, which is why we denote this slope as  $\chi^{-1}$ .

Based on what we can measure for our system, we can test the following three scaling relations:

$$T^* \sim l^{*\delta} , \quad (4.3)$$

$$\chi^{-1} \sim |\Gamma^*|^\gamma , \quad (4.4)$$

$$\Delta l \sim |\Gamma^*|^\beta . \quad (4.5)$$

The mean field values of these exponents are:

$$\delta = 3 , \quad (4.6)$$

$$\gamma = 1 , \quad (4.7)$$

$$\beta = 1/2 . \quad (4.8)$$

Note that we do not measure the value of  $\delta$ , but based on the shape of the flow curves and mean field prediction, we have set it to  $\delta = 3$ . The fact that fit of the data to Eq. 4.2 works well justifies this assumption. As  $\Delta l$  is found by identifying the zero crossings of the derivative of  $a(l - l_i)^3 + \chi^{-1}(l - l_i)$ ,  $\Delta l$  and  $\chi^{-1}$  are related. This results in the constraint  $\gamma = 2\beta$ . Hence, from the flow curves we can extract a single exponent (either  $\gamma$  or  $\beta$ ); the determination of the other is then a consistency check.

**Fluctuations** – As diverging fluctuations are an important hallmark of critical behavior, we want to study the fluctuations in the velocity of the

flow. However, we measure the disk angle  $\theta$  and we cannot a priori know that we are allowed to calculate a *velocity* for our fluctuating disk; for fluctuating systems such as a random walker, the velocity is not even defined.

Of course, because of the inertia of our driving disk, the velocity cannot grow arbitrarily large, and extremely rapid velocity fluctuations are suppressed. To get an idea of the relevant scales, we note that the moment of inertia of our disk and corotating grains  $\approx 0.3 \text{ gm}^2$ . Even if we suddenly subject the disk to the typical driving torque of 30 mNm, we expect its rate to vary with 0.3 rps in 1/63 s. As the effective torque fluctuations are typically much smaller, we do not expect rate differences of the order of 0.1 rps between two consecutive data points. Therefore, we expect a smooth  $\theta(t)$  that we *can* differentiate.

We will use two different methods to extract values for the magnitude  $\sigma^2$  and characteristic time scale  $\tau$  of  $\omega(t)$ .

First, we will show further evidence that we indeed probe  $\theta(t)$  fast enough to evaluate its derivative  $\omega$ , and then calculate its variance  $\sigma_\omega^2$  as a measure for the magnitude of the fluctuations. The characteristic time scale  $\tau_a$  is obtained from the autocorrelation function of  $l$  (which is  $\log_{10}(\omega/1 \text{ rps})$ ).

Second, we interpret the motion of our disk as the path of a massive random walker, whose behavior is given by an overall drift plus a noise  $\eta$ . To capture the effect of inertia, the noise  $\eta$  is not delta-correlated, but we assume it has an exponential correlation:

$$\langle \eta(t')\eta(t'') \rangle = \sigma_c^2 \exp(-|t'' - t'|/\tau_c), \quad (4.9)$$

where  $\sigma_c^2$  is the magnitude and  $\tau_c$  the time scale of the fluctuations. For a random walker with drift, the quantity to look at is  $\sigma_{\Delta\theta}^2$  as a function of  $\Delta t$ . For a system with noise as in Eq. 4.9, this is given by [110]:

$$\sigma_{\Delta\theta}^2 = 2\sigma_c^2\tau_c[\Delta t - \tau_c(1 - e^{-\Delta t/\tau_c})]. \quad (4.10)$$

For small  $\Delta t$ , this reduces to  $\sigma_c^2\Delta t^2$ , *i.e.*, ballistic motion due to the correlated nature of  $\eta$ . In this regime,  $\omega$  is well-defined. For large  $\Delta t$ ,  $\sigma_{\Delta\theta}^2$  approaches  $2\sigma_c^2\tau_c\Delta t$ , *i.e.* diffusive behavior (where  $\sigma_c^2\tau_c$  is the diffusion constant  $D$ ). We stress that, in this model, the complete behavior of  $\sigma_{\Delta\theta}^2$  is governed by two parameters:  $\sigma_c^2$  and  $\tau_c$ .

In Sec. 4.5.6 we will show that the analyses via  $\omega(t)$  and  $\sigma_{\Delta\theta}^2$  produce similar results for  $\sigma^2$  and  $\tau$ ; both the fluctuation magnitudes and correlation times are consistent between both methods.

The scaling relations we will test for the fluctuations are:

$$\sigma^2 \sim \Gamma^{*- \gamma} , \quad (4.11)$$

$$\tau \sim \Gamma^{*- \nu} . \quad (4.12)$$

The mean field values of these exponents are:

$$\gamma = 1 , \quad (4.13)$$

$$\nu = 1/2 , \quad (4.14)$$

where  $\gamma$  is the same as in Eq. 4.4. Of course, we measure the fluctuations as a function of both  $\Gamma^*$  and  $T^*$ , so if we want to look at the scaling only as a function of  $\Gamma^*$ , we have to decide for which  $T$  to select  $\tau$  and  $\sigma^2$ . Since the critical point is the inflection of the curve for  $\Gamma^* = 0$ , we will take  $\tau$  and  $\sigma^2$  at the inflection point for each  $\Gamma^*$ .

In conclusion, we can determine *two* independent scaling exponents of our data;  $\nu$ , which characterizes the divergence of the characteristic time scale; and  $\gamma = 2\beta$ , which can be obtained from the magnitude of the fluctuations, and from the steady state flow curves.

## 4.4 Flow Curves

In this section we will fit the flow curves with a cubic polynomial and demonstrate that the fit accurately describes the data. We will use the fit parameters thus obtained to determine  $\Gamma_c$  and to discuss how the flow curves vary with  $\Gamma$ . We then extract values for the inverse slope at the inflection point,  $\chi$ , and the distance between the local minimum and maximum of the flow curve,  $\Delta l$ , and finally determine their scaling with  $\Gamma^*$ .

**Fit** – To determine the shape of the flow curves  $T(l)$ , we fit the flow curves with a cubic polynomial (Eq. 4.2):

$$T = a(l - l_i)^3 + \chi^{-1}(l - l_i) + T_i .$$

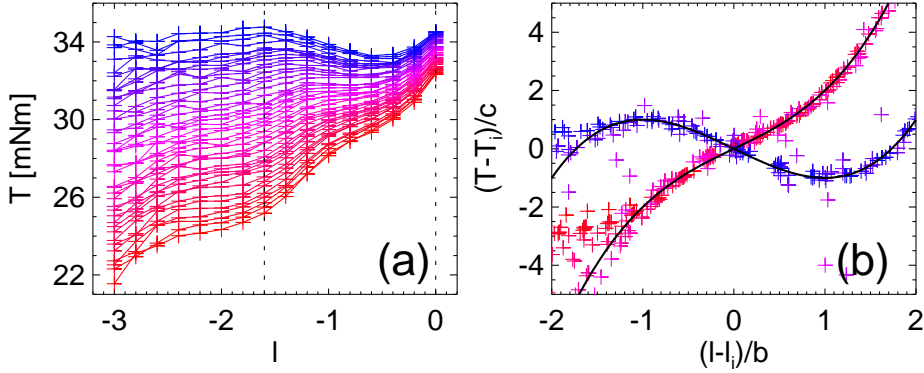


FIGURE 4.5: (a) The flow curves measured in rate control. The color indicates  $\Gamma$  from 0.3 (blue) to 0.7 (red). The dotted lines indicate the region of the curves we fit. (b) Using the fit to Eq. 4.2, we collapse the flow curves onto the master curves (plotted in black)  $T - T_i = l_i + 1/2(l - l_i)^3 \pm 3/2(l - l_i)$ , using the horizontal scale factor  $b = \sqrt{|\chi^{-1}/3a|}$  and the vertical scale factor  $c = \sqrt{|4(\chi^{-1})^3/27a|}$ . Note that for  $\Gamma^*$  very close to 0,  $b$  and  $c$  become very small, which magnifies the small deviation between the fit and the data (see purple outliers for  $\Gamma \approx 0.46$ ).

From the raw data, shown in Fig. 4.5(a), it can be seen that it is not possible to fit the flow curve over the full range of  $l$  with a cubic polynomial in  $l$ , as Eq. 4.2 is symmetric around  $(l_i, T_i)$ , whereas the data is not. We find that the fit corresponds well to the data for all  $\Gamma$  if we limit the fitting range to  $-1.6 < l < 0$  (we have verified that there is no strong dependence of the fit parameters on the choice of these boundaries).

To demonstrate that the fit accurately describes the data in this range, we collapse the flow curves using the fit parameters. To achieve a collapse, we plot  $(l - l_i)/b$  on the horizontal axis and  $(T - T_i)/c$  on the vertical axis. This way, the inflection point is shifted to the origin, and  $b$  and  $c$  are chosen such that the local maximum for  $\Gamma^* < 0$  rescales to  $(-1, 1)$ . The actual values  $b = \sqrt{|\chi^{-1}/3a|}$  and  $c = \sqrt{|4(\chi^{-1})^3/27a|}$  are found by solving a simple quadratic equation derived from Eq. 4.2. We show that the rescaled data nicely collapses onto two branches in Fig. 4.5(b). The master curves,  $T - T_i = l_i + 1/2(l - l_i)^3 \pm 3/2(l - l_i)$  are added in black.

The dependence of the four fit parameters of Eq. 4.2 on  $\Gamma$  is shown in Fig. 4.6. In (a), we plot  $\chi^{-1}$ , which sets the slope at the inflection point, as function of the actual  $\Gamma$ . The curve is close to linear and its zero crossing



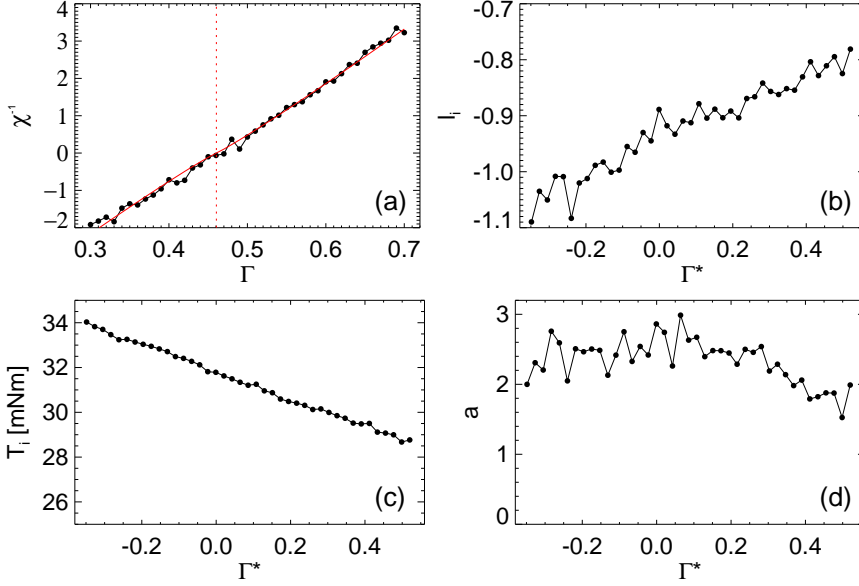


FIGURE 4.6: The four parameters of the fit with Eq. 4.2 as a function of  $\Gamma$ .  $\chi^{-1}$  (a) is linear in  $\Gamma$  and crosses  $\chi^{-1} = 0$  at  $\Gamma_c$ . We determine  $\Gamma_c$  and  $\gamma$  by fitting this data (the fit is overplotted in red); the dashed line indicates  $\Gamma_c$  *i.e.*  $\Gamma^* = 0$ .  $l_i$  (b) and  $T_i$  (c) vary linearly with  $\Gamma^*$ .  $a$  (plotted in (d)) is constant, especially around  $\Gamma^* = 0$ .

defines  $\Gamma_c$ . We use this data to determine  $\Gamma_c$  as well as the exponent  $\gamma$  (which is the scaling exponent of the slope at the inflection point as a function of  $\Gamma^*$ ) by fitting the data with:  $\chi^{-1} = \alpha \cdot \text{sgn}(\Gamma - \Gamma_c) |\Gamma - \Gamma_c|^\gamma$ . Doing so, we find  $\gamma = 1.07 \pm 0.27$ , and  $\Gamma_c = 0.460 \pm 0.012$ . The red dashed line in Fig. 4.6(a) represents  $\Gamma_c$ , *i.e.*,  $\Gamma^* = 0$ .

The rotation rate at the inflection point,  $l_i$ , increases linearly with  $\Gamma^*$  (Fig. 4.6(b)). The corresponding  $T_i$ , that decreases linearly with  $\Gamma^*$ , is plotted in Fig. 4.6(c). These scalings offer insight into the underlying mechanisms of the transition from slow to fast flow, and will be discussed in App. 4.A.3. The global cubic shape of the flow curve is set by the fit parameter  $a$ . In Fig. 4.6(d) we plot  $a(\Gamma^*)$ , which, especially around  $\Gamma^* = 0$ , is essentially constant. This agrees with the observation that, away from the inflection point, the flow curves exhibit a very similar shape (Fig. 4.5(a)).

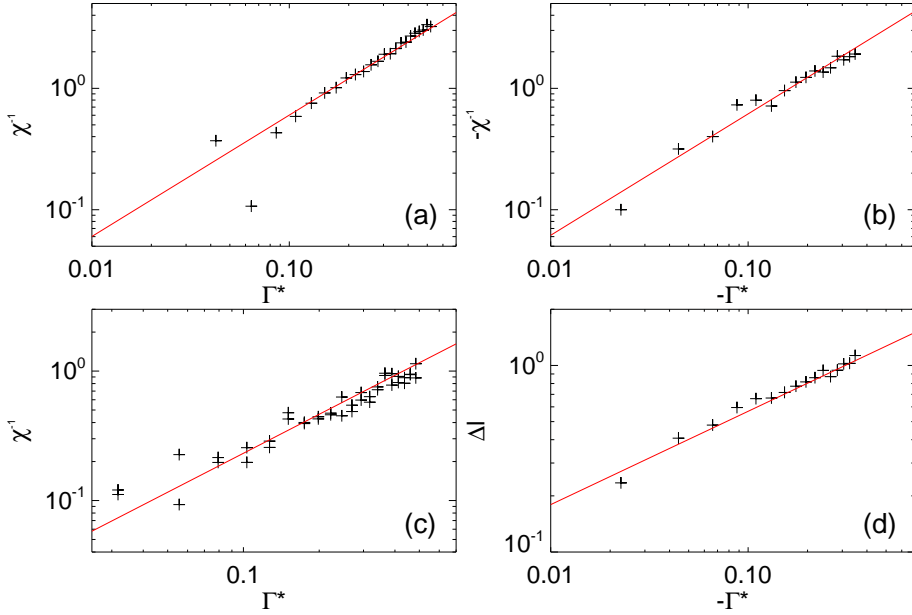


FIGURE 4.7: The scaling of  $\chi^{-1}$  and  $\Delta l$  with  $\Gamma^*$ . (a) Susceptibility for rate control  $\Gamma^* > 0$ , (b) for  $\Gamma^* < 0$ , (c) for stress control. In (a-c), the red lines are linear fits. (d)  $\Delta l$  for rate control. Here, the red line is a square root fit.

**Susceptibility  $\chi$**  – The susceptibility  $\chi$  is defined as the inverse slope of  $T(l)$  at the inflection point, and is expected to diverge as  $\Gamma^* \rightarrow 0$ . In Fig. 4.7(a), we plot  $\chi^{-1}$  (actual slope; inverse susceptibility) versus  $\Gamma^*$  for  $\Gamma^* > 0$ , and in Fig. 4.7(b) we plot  $\chi^{-1}$  for  $\Gamma^* < 0$ , both measured in *rate* control. In both cases, the scaling is close to linear as can be seen from the linear fits added in red. The prefactors for (a),  $6.02 \pm 0.21$  and (b),  $6.16 \pm 0.25$ , are equal within error bars. In Fig. 4.6(a), we found an exponent  $\gamma = 1.07 \pm 0.27$  for the full range in  $\Gamma^*$ . Here, we show that an exponent 1 (which is the mean field value) also matches the data well. The very nice linear relation between  $\Gamma^*$  and  $\chi^{-1}$  indicates that our data agrees with a mean field description of the system.

We can also obtain  $\chi^{-1}$  from the *stress*-controlled measurements that we use to study the fluctuations. The 400 measurements from data set 1 are performed as 40 torque ramps at constant  $\Gamma^*$ . From these 40 ramps,

we can extract 40 flow curves and extract  $\chi^{-1}$ . The result is shown in Fig. 4.7(c) and tells us that also in stress-controlled experiments,  $\chi^{-1}$  grows linearly with  $\Gamma^*$ . We note however that in this case, the prefactor is  $2.32 \pm 0.19$ , which is different than in Fig. 4.7(a-b). As we shall see in Sec. 4.5, the flow curves measured in  $T$  control are not exactly the same as the curves measured in  $\Omega$  control. One possible explanation is that constant  $T$  and constant  $\Omega$  measurements sample different ensembles, and  $\langle \omega(T) \rangle$  and  $\Omega(\langle T \rangle)$  need not coincide.

**Rate Difference  $\Delta l$**  – In Fig. 4.7(d), we plot  $\Delta l$  - which is extracted from the fit to the flow curve via  $\Delta l = \sqrt{-4\chi^{-1}/3a}$  - as a function of  $\Gamma^*$ . In red, we add a fit with a power-law with exponent  $1/2$  (the mean value for  $\beta$ ). We find that this fit accurately matches the data. As explained above, we have the constraint  $\gamma = 2\beta$ . The fact that this is indeed true for the data, supports our claim that the steady state flow curves can be described using a mean field picture.

**Conclusion** – In this section we have seen that the mean field description works well to describe the shape of the flow curves. The scaling of  $\chi^{-1}$  and  $\Delta l$  agrees with mean field scaling exponents  $\gamma = 1$  and  $\beta = 1/2$ .

## 4.5 Fluctuations

In this section we will discuss the magnitude and time scale of the fluctuations in the  $\omega(t)$  signals, which are measured in experiments at fixed  $\Gamma$  and  $T$ .

As explained in Sec. 4.3, the fluctuations will be analyzed using two different methods. In Sec. 4.5.2- 4.5.3, we will show that we measure  $\theta(t)$  at high enough temporal resolution so that we can evaluate its derivative  $\omega(t)$ . Using  $\omega(t)$ , we then calculate the fluctuation magnitude  $\sigma_\omega^2$  and time scale  $\tau_a$  from the autocorrelation function of  $l(t)$ . In Sec. 4.5.4, we approach the problem from a statistical point of view by studying the evolution of  $\sigma_{\Delta\theta}^2$  as function of time. Using Eq. 4.10, we obtain magnitude  $\sigma_c^2$  and time scale  $\tau_c$ . In Sec. 4.5.5 we discuss how to locate the critical point in stress-controlled experiments, and in Sec. 4.5.6 we show the scaling of  $\sigma_\omega^2$  and  $\tau_a$  with  $\Gamma^*$ .

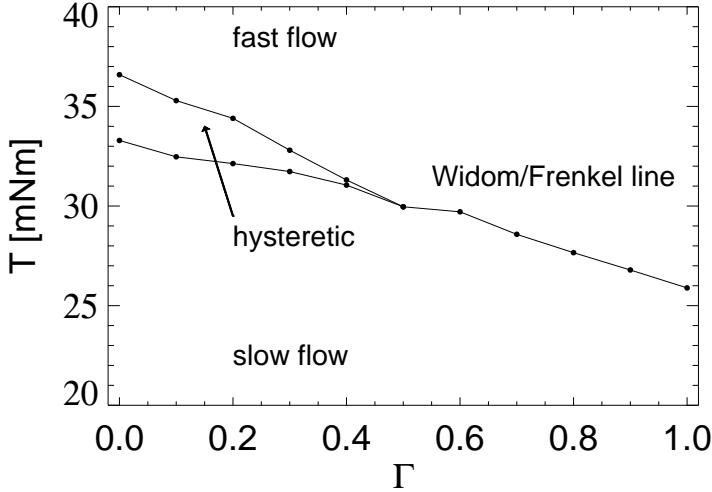


FIGURE 4.8: The slow and fast flow regime, separated by a hysteretic regime ( $\Gamma^* < 0$ ) and the Widom/Frenkel line ( $\Gamma^* > 0$ ) [111], in  $(T, \Gamma)$ -space.

#### 4.5.1 Phenomenology

Before we study the velocity signals in detail, we identify the different regimes in  $(T, \Gamma)$ -space in Fig. 4.8. For  $\Gamma < \Gamma_c$ , we plot the values of  $T$  at the local minima and maxima of the flow curves. In between these two boundaries, the system is hysteretic. This means that if we do experiments in torque control in this regime, the flow is bistable and fluctuations may cause  $\omega$  to be jumping back and forth between the slow and fast flowing branch. At  $\Gamma_c$ , these boundaries come together. For  $\Gamma > \Gamma_c$ , we plot a line which connects the torque values at the inflection point. This line - which is called Widom or Frenkel line [111] - signifies the smooth crossover between the slow and the fast flow, and it is here where we expect the fluctuations to peak for each  $\Gamma$ . While studying the behavior close to the Widom line, we will also identify several fundamental differences between the slow and the fast flowing regime. This suggests that the transition that we study is between two *flowing*, but very different, states.

A natural question to ask is what happens when the fluctuation experiments are performed in rate control. You could expect very large fluctuations in  $T$  for flow in the negative slope regime, since there is no con-

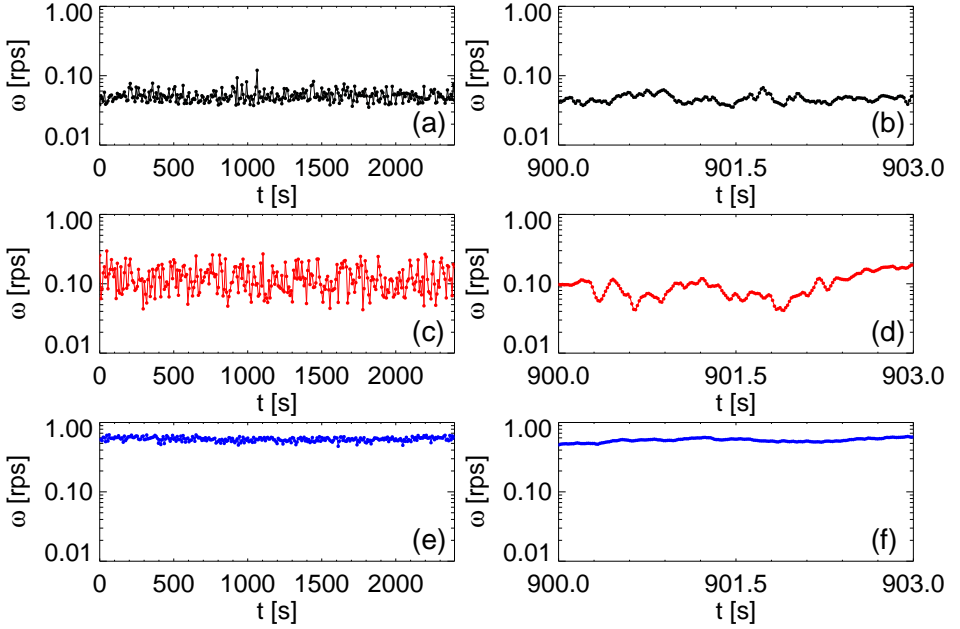


FIGURE 4.9:  $\omega(t)$  for  $\Gamma$  just above  $\Gamma_c$  and  $T < T_i$  (a-b),  $T \approx T_i$  (c-d),  $T > T_i$  (e-f). The vertical scale is equal for all panels to visualize that the fluctuations are the largest for  $T \approx T_i$ ; b,d,f zoom in on shorter time scales. The fluctuations are much smaller for fast flow than for slow flow, but are maximal at the inflection point (Widom line).

stant  $T$  for which there is stable flow in this regime. Around the critical point the fluctuations could be small, since a small change in  $T$  results in a significantly different  $\Omega$ . However, we found that these experiments cannot be performed in our setup. The problem is that the native mode of the rheometer is stress control, and rate-controlled experiments require a feedback system. The characteristic time of the feedback loop, the so-called *csr*-value, completely dominates the size of the fluctuations, and there is no clear relation between the amplitude of the fluctuations and the distance to the critical point.

#### 4.5.2 Determination of the Velocity

In this section we study the raw signal,  $\theta(t)$ , and its derivative  $\omega(t)$ , to demonstrate that we probe  $\theta(t)$  at a high enough temporal resolution to be

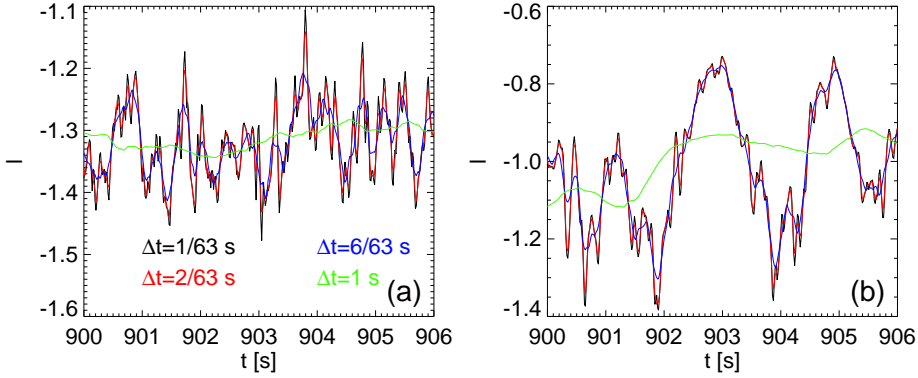


FIGURE 4.10:  $\omega(t)$  calculated for four different values of  $\Delta t$  as indicated in the legend. (a)  $\omega(t)$  for  $(\Gamma^* = 0.060, T^* = -0.032)$  (b)  $\omega(t)$  for  $(\Gamma^* = 0.060, T^* = 0.0032)$ . For  $\Delta t = 1/63$  s,  $2/63$  s and  $6/63$  s, the signal looks roughly the same, only the fluctuations become smaller for longer averaging. For  $\Delta t = 1$  s, which is longer than the  $\tau$  corresponding to (a), the dominated features of the curve completely disappeared, in (b)  $\tau \approx 1$  s, and the slow fluctuations are still present in the green signal.

allowed to take a derivative. In Fig. 4.9 we plot  $\omega(t)$  (a three-point derivative of  $\theta(t)$  with  $\Delta t = 1/63$  s) for slow, intermediate and fast flow. Again it can be seen that the fluctuations are largest at intermediate flow rate. In panels (c,d,f) we show a magnification of the data which clearly shows the individual data points (in (a,c,e) we only plot each 500th point). On this scale, the signal appears smooth which means that  $\theta$  does not correspond to purely delta-correlated diffusive behavior; rather,  $\theta$  is sufficiently smooth on short time scales so that  $\omega(t)$  is well-defined.

As an additional check to see if we extract a proper velocity, we calculate the three-point derivative of  $\theta(t)$  for different  $\Delta t$  and show the results in Fig. 4.10. For  $\Delta t = 1/63$  s,  $2/63$  s and  $6/63$  s, the signal looks quite similar. For  $\Delta t = 1$  s (which we will show to be longer than the correlation time  $\tau$  that corresponds to (a)), the dominant fluctuations are strongly suppressed. On the contrary, for the data in (b), for which we will show that  $\tau \approx 1$  s, the dominant slow features of the curve are still visible in the curve for  $\Delta t = 1$  s.

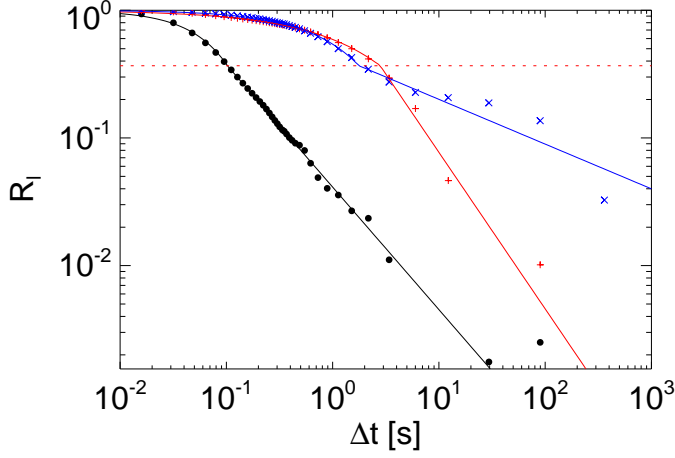


FIGURE 4.11: Autocorrelation functions  $R_l$  for the data in Fig. 4.9. For small  $\Delta t$ , the curves can be fitted with a stretched exponential. The black ( $\bullet$ ) curve is for slow flow and has a short time scale, the red (+) curve corresponds to large fluctuations and has the longest time scale. The blue ( $\times$ ) curve is for fast flow and also has a high  $\tau$ . For large  $\Delta t$ , the curves take the shape of a power-law where the fast flow has the highest exponent.

### 4.5.3 Autocorrelation

Now that we have established that we have a well-defined  $l(t)$ , we will extract the characteristic time  $\tau_a$  from its autocorrelation function  $R_l(\Delta t)$ . In principle, it would also be possible to directly calculate the autocorrelation function of  $\theta(t)$ . The reason that we do not do this, is that long time fluctuations in the signal will dominate the autocorrelation function and result in an  $\infty$  time scale. If we first differentiate to get  $l(t)$ , we can see both the fast time scale (in the initial exponential decay) and the longer time scale (in the tail of the correlation function). The autocorrelation function is defined as:

$$R_l(\Delta t) = \frac{\sum_{k=0}^{N-\Delta t-1} (l_k - \bar{l})(l_{k+\Delta t} - \bar{l})}{\sum_{k=0}^{N-1} (l_k - \bar{l})^2}, \quad (4.15)$$

where  $N$  is the number of data points in  $l(t)$  after the removal of a transient. We removed a 4 min transient from each data set, which even for

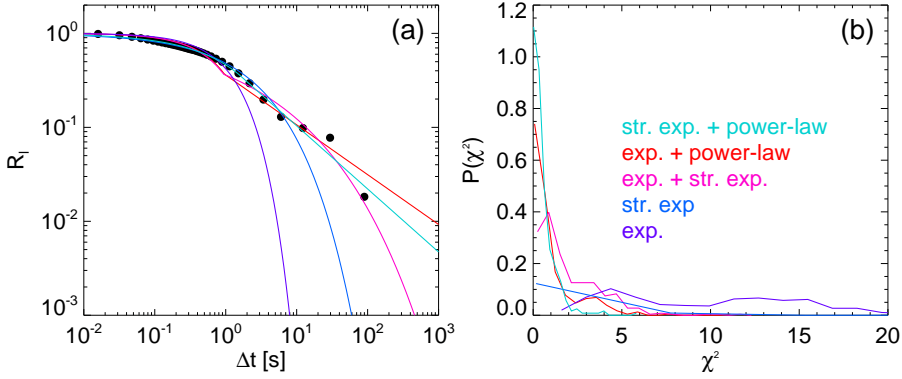


FIGURE 4.12: (a) The autocorrelation function  $R_l$  for  $(\Gamma^* = 0.19, T^* = -0.024)$  fitted with the five different fit functions that are indicated in (b). (b) The distributions  $\chi^2$  for the five fits. Clearly, the fit with Eq. 4.16 is the best.

the slowest runs corresponds to a strain of 7 rotations – enough to be sure that the system has reached a steady state.

In Fig. 4.11 we show  $R_l(\Delta t)$  for the slow, intermediate, and fast flow curves shown in Fig. 4.9. The curves have significantly different and complex shapes and cannot easily be collapsed or fitted with a standard exponential decay fitting function. In this section we will carefully investigate in what way best to extract a time scale from these correlation functions.

We will start by finding a fitting function for  $R_l$ . The data in Fig. 4.11 suggests that the autocorrelations are stretched exponentials for small  $\Delta t$ , crossing over to power-laws for larger  $\Delta t$ . This is illustrated in Fig. 4.12. In (a), we show fits to  $R_l$  for a slow flow run ( $\Gamma^* = 0.060, T^* = -0.0032$ ). Attempts to fit the data with an exponentially decaying function (purple) and stretched exponential (blue) fail for large  $\Delta t$ , where  $R_l$  decreases more slowly. We will therefore use a fit that is a linear combination of two functional forms, one for  $\Delta t < \tau_a$  and another for  $\Delta t > \tau_a$ . We start with a three-parameter fit that combines stretched exponential decay and a power-law (in cyan):

$$R(\Delta t) = \frac{s(\tau_a)}{e} (\Delta t / \tau_a)^\eta + [1 - s(\tau_a)] e^{-(\Delta t / \tau_a)^\zeta}, \quad (4.16)$$



where  $\zeta$  is the stretching exponent, and  $\eta$  is the slope of the power-law for large  $\Delta t$ .  $s(\tau_a)$  is a logistic function that governs the crossover from stretched exponential to power-law, with its center around  $\tau_a$ :

$$s(\tau_a) = \frac{1}{1 + e^{\lambda(\log_{10}(\tau_a/\Delta t))}} , \quad (4.17)$$

where  $s \approx 0$  for  $\Delta t < \tau_a$ ,  $s \approx 1$  for  $\Delta t > \tau_a$ , and  $\lambda$  determines the width of the crossover. We find that the crossover in our data is sharp and verify that the fit does not significantly depend on  $\lambda$  as long as  $\lambda \gtrsim 50$  (we pick  $\lambda = 100$ ).

In Fig. 4.12(a), we compare this three-parameter fit with a two-parameter combination of a simple exponential decay and a power-law (Eq. 4.16 with  $\zeta = 1$ , plotted in red):

$$R(\Delta t) = \frac{s(\tau_a)}{e} (\Delta t/\tau_a)^\eta + [1 - s(\tau_a)] e^{-\Delta t/\tau_a} , \quad (4.18)$$

and a two-parameter combination of a simple and a stretched exponential (pink):

$$R(\Delta t) = s(\tau_a) \times e^{-(\Delta t/\tau_a)^\zeta} + [1 - s(\tau_a)] e^{-\Delta t/\tau_a} . \quad (4.19)$$

In Fig. 4.12(a) we see that only the fit with Eq. 4.16 is capable of grasping all the features of the data. We verify if this is the case for all the runs by plotting the distributions of the quality of the fits,  $\chi^2$ , for the five different functional forms that are shown in Fig. 4.12(a) in Fig. 4.12(b). The high peak at low  $\chi^2$  in the cyan curve shows that the fit with Eq. 4.18 is clearly superior. This is not surprising as it is the one with the most fit parameters. However, Fig. 4.12 shows that the three-parameter fit is *significantly* better than the two-parameter fits, suggesting that we need three fit parameters to describe the complex shape of  $R_l$ .

To see how  $R_l$  varies throughout our parameter space, we plot the values of  $\tau_a$ ,  $\zeta$  and  $\eta$  as a function of  $\Omega$  and  $\Gamma$  in Fig. 4.13. Even though  $T$  is the control parameter, we plot as a function of  $\Omega$  so that we can compare  $\tau_a$  to the duration of one revolution  $1/\Omega$ .

In Fig. 4.13(a), we see that, for each  $\Gamma$ ,  $\tau_a$  initially increases with  $\Omega$  and reaches a peak for  $\Omega \approx 0.2$  rps. For large  $\Omega$ ,  $\tau_a$  decreases but does not drop back very much, and approaches  $\Omega^{-1}$  for large  $\Omega$  – this suggests that in this regime, correlations due to the periodicity of the system start

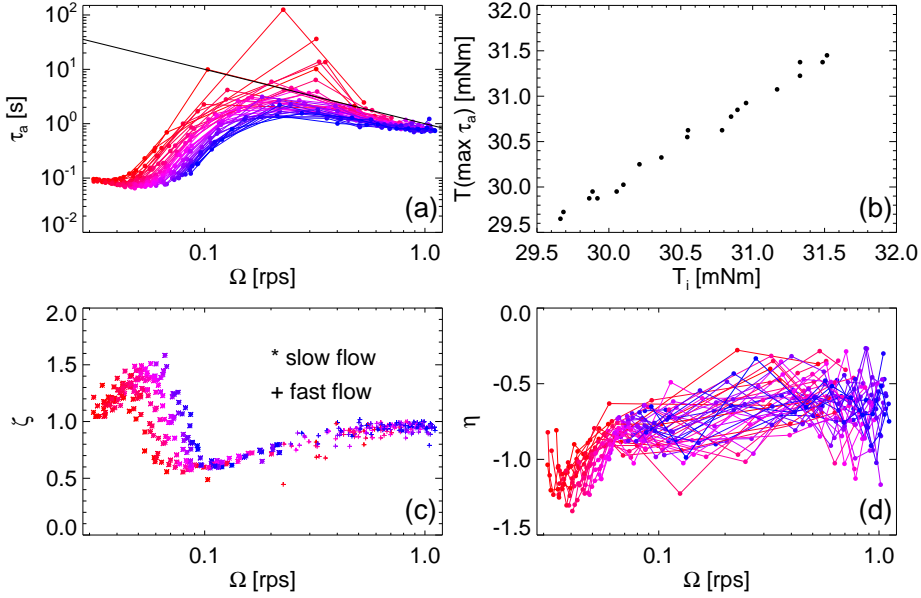


FIGURE 4.13: The fit parameters of the autocorrelation function. (a) the time scale  $\tau_a$  as a function of  $\Omega$ , color coded by  $\Gamma$  (red corresponds to low  $\Gamma$ ). The black line indicates  $\tau_a = 1/\Omega$ . (b) The  $T$  for which the time scale is longest  $T(\max \tau_a)$  is the torque at the inflection point  $T_i$ .  $T_i$  is found using a fit with Eq. 4.2. (c) The stretching exponent  $\zeta$ . The (\*) and (+) symbols reflect slow and fast flow. (d) The power-law slope  $\eta$  of the autocorrelation for long  $\Delta t$ .

to dominate. Nevertheless, the data shows a clear peak, which is largest for  $\Gamma^* \approx 0$ .

The dependence of  $\zeta$  (Fig. 4.13(c)) is more complex. For slow and fast flow,  $\zeta \approx 1$ , whereas in the intermediate range,  $\zeta$  varies between 1.5 and 0.5. Surprisingly, the region where  $\zeta$  varies most dramatically,  $\Omega \approx 0.07$  rps, is significantly below  $\Omega_i$  (as indicated by the plot symbols).

The dependence of  $\eta$  (Fig. 4.13(d)) is noisy but there is a trend that  $\eta$  is lower for slow flow. In Fig. 4.13(b) we plot the  $T$  at which the time scale peaks versus the inflection torque  $T_i$  and see that, as expected, the time scale peaks at the inflection point.

We will now investigate the behavior of  $\tau_a$  for large  $\Omega$ , where  $\tau_a \approx \Omega^{-1}$ . In Fig. 4.14, we test if a concomitant periodicity is visible in the raw data

for a fast flow run. In (a), we plot  $\omega$  as a function of  $\theta$  but find that it is hard to see which frequencies are present in the signal. Therefore, we plot the power spectrum ( $PS$ ) as a function of frequency of  $\omega(\theta)$  in  $\theta$  space ( $f_r$ ) in (b). We see that  $PS \sim f_r^{-2}$ , which corresponds to normal Brownian noise. Nevertheless, zooming in on the spectrum around  $f_r = 1$ , we find that there is a 1 rev periodicity in the data (inset).

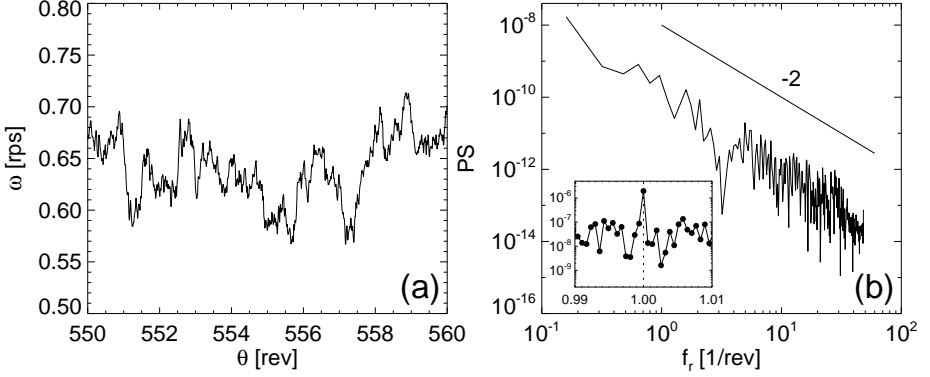


FIGURE 4.14: (a)  $\omega$  as a function of  $\theta$ . For this run,  $\tau_a = 1.24$  s whereas  $\Omega^{-1} = 1.53$  s. (b) The power spectrum ( $PS$ ) of  $\omega(\theta)$  scales as  $PS \sim f_r^{-2}$ , which corresponds to normal Brownian noise. In the inset, we show the spectrum around  $f_r = 1$ , which shows that there is a 1 rev periodicity in the system.

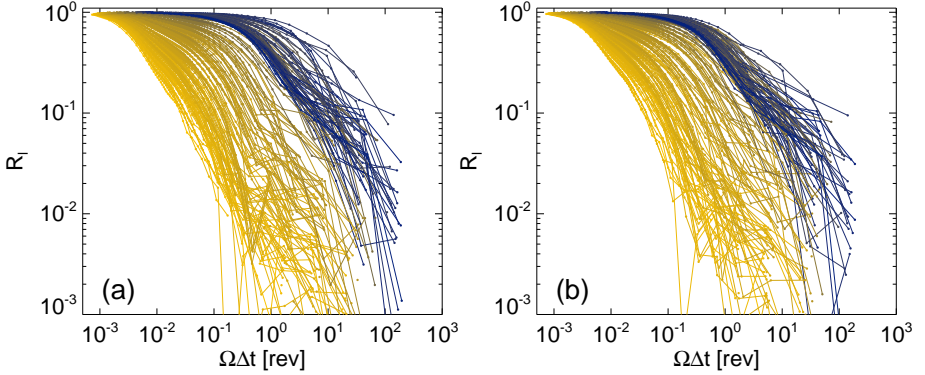


FIGURE 4.15: All the autocorrelation functions  $R_l$  for data set 2. In (a), we show the uncorrected data. In (b), we show  $R_l$  where the 1 rev component is filtered out before calculating the correlation function. In both cases, there is a (blue) cluster of fast flowing curves with a  $\tau_a \approx \Omega^{-1}$ .

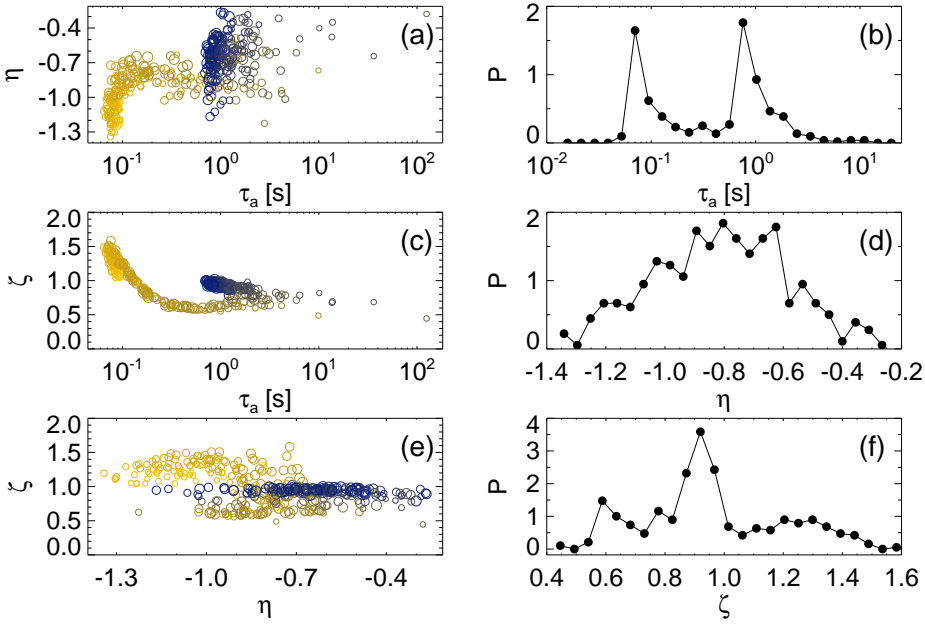


FIGURE 4.16: Scatter plots of  $\tau_a$  vs  $\eta$  (a),  $\tau_a$  vs  $\zeta$  (c) and  $\eta$  vs  $\zeta$  (e). The color of the data points indicates  $l$  (yellow:  $l < l_i$ , green:  $l \approx l_i$ , blue:  $l > l_i$ ), the symbol size indicates  $\Gamma$  where a larger blob corresponds to a higher  $\Gamma$ . The local blobs show how  $R_l$  is systematically different for flow, intermediate and fast flows. These blobs are also visible in the distributions of  $\tau_a$  (b),  $\eta$  (d) and  $\zeta$  (f).

We want to investigate whether filtering out the  $\Omega^{-1}$  component from  $l(t)$  significantly changes the signal; this might make the results for slow and fast flow more comparable. In Fig. 4.15 we show all the correlation functions for data set 2 for both the unfiltered (a) and the filtered (b) case. We find that although the filtering affects  $R_l$ , in both panels of the figure there is a cluster of (blue) curves for fast flow with a time scale of approximately  $\Omega^{-1}$ . This suggests that the behavior of  $\tau_a \sim \Omega^{-1}$  is not only caused by a spurious  $\Omega^{-1}$  component in the spectrum.

To further investigate qualitative differences between slow and fast flows, we study the results of the fit with Eq. 4.16 in more detail in Fig. 4.16. The scatter plots of  $\tau_a$  vs  $\eta$  (a),  $\tau_a$  vs  $\zeta$  (c) and  $\eta$  vs  $\zeta$  (e) show several blobs, which we believe to correspond to physically different flow regimes. In (a),

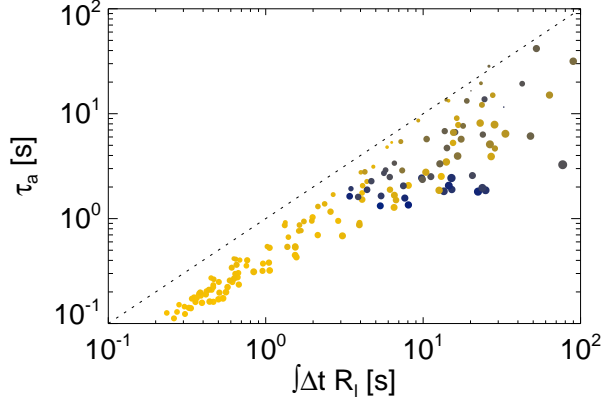


FIGURE 4.17: A scatter plot of  $\tau_a$  vs  $\int \Delta t R_l$  for data set 2 shows a good correspondence. The correlation is not perfect, which is caused by the complex shape of  $R_l$ . This can be seen from the size of symbols that represent  $\eta$  (larger symbols are larger  $\eta$ ). A large  $\eta$  results in a large area under the curve and a relatively large  $\int \Delta t R_l$ .

there are two clear blobs, one at low  $\tau_a$  for slow flow and one at high  $\tau_a$  for fast flow. In (c), we see a systematic relation between  $\tau_a$  and  $\zeta$ , and a large blob arises for fast flow at  $\zeta \approx 1$ . Panel (e) shows that slow, intermediate, and fast flow are well separated with different  $\zeta$ , whereas within one flow regime, there is a large spread in  $\eta$ . The different regimes arise as peaks in the distributions of  $\tau_a$  (b) and  $\zeta$  (f). The blobs in Fig. 4.16 suggest that the dominant fluctuations in the slow (quasi-static) and fast flow (inertial) regime might be caused by different physical phenomena.

Because of the three-parameter form of our fit, and the complex variation and dependencies of the fit parameters, doubt might arise on the values found for  $\tau_a$ . We therefore extract a time scale from  $R_l$  without having to fit, by evaluating its integral over time. Due to long time fluctuations in  $R_l$ , the integral over  $R_l$  does not converge to zero but rather slowly fluctuates around zero, which makes the integral of  $R_l$  for  $\Delta t \rightarrow \infty$  ill-defined. To get a well-defined value for  $\int \Delta t R_l$ , we stop integrating once  $R_l \leq 10^{-2}$  – this leads to robust estimates for  $\int \Delta t R_l$ , not strongly dependent on the value of the cut-off.

In Fig. 4.17 we show a scatter plot of  $\tau_a$  vs  $\int \Delta t R_l$  which shows a good correspondence. Nevertheless, systematic deviations can be seen: for ex-

ample, large values of  $\eta$  (large symbols) lead to  $\int \Delta t R_l > \tau_a$ .

**Conclusion** – In this section we have shown that we can fit the autocorrelation function  $R_l$  with Eq. 4.16 and obtain  $\tau_a$ . The fit parameters systematically vary with  $T$  and  $\Gamma$ . Not only do we see that  $\tau_a$  increases towards the critical point, but we also find that the fits are systematically different for flow rates above and below the critical point, suggesting qualitative differences between fast and slow flows. The correspondence between  $\tau_a$  and  $\int \Delta t R_l$  indicates that we have extracted a robust time scale from  $l(t)$ .

#### 4.5.4 Statistics of $\Delta\theta$

In this section we will analyze the data by looking at the statistics of  $\Delta\theta$ . This way, we avoid having to calculate the instantaneous velocity of the probe, but instead, look at the fluctuations in  $\Delta\theta$  around the overall drift  $\langle\theta\rangle = \Omega\Delta t$ . By fitting  $\sigma_{\Delta\theta}^2(\Delta t)$  to Eq. 4.10:

$$\sigma_{\Delta\theta}^2 = 2\sigma_c^2\tau_c[\Delta t - \tau_c(1 - e^{-\Delta t/\tau_c})],$$

we get values for the magnitude  $\sigma_c^2$  and time scale  $\tau_c$  of the fluctuations, independent of those obtained from  $l$ .

We calculate  $\Delta\theta$  via  $\Delta\theta = \theta(t + \Delta t) - \theta(t)$  for  $\Delta t = \text{ceil}(10^{n/5})/63$ , with  $n = 0, 1, \dots, 23$  (as before, we always remove a 4 min. transient).

In Fig. 4.18 we show distributions of  $\Delta\theta$  for slow and fast flows and different  $\Delta t$ . It is clearly visible that the center of the distributions moves to larger  $\Delta\theta$  for larger  $\Delta t$ , which is an indication that the fluctuations do not dominate the overall drift of the signal.

In Fig. 4.19 we show the rescaled distributions  $(\Delta\theta - \langle\Delta\theta\rangle)/\sigma_{\Delta\theta}$ , where  $\sigma_{\Delta\theta} = \sqrt{\langle(\Delta\theta - \langle\Delta\theta\rangle)^2\rangle}$ , for slow (a), intermediate (c), and fast (e) flows. We find that these rescaled pdf's for different  $\Delta t$  collapse reasonably well; hence their variation with  $\Delta t$  can be captured by  $\sigma_{\Delta\theta}$ . The pdf's typically are asymmetric and have the shape of skewed Gaussians. There is a trend that for slow flow, the pdf is positively skewed whereas for fast flow, it is negatively skewed. We suggest that this originates from the fact that the flow curve becomes flatter towards the inflection point. We expect that fluctuations in  $\omega$  can be larger where the flow curve is flatter. This leads to an asymmetry in  $P(\Delta\theta)$ . Note that for fast flows, the inflection point is so far away that the pdf becomes symmetric and Gaussian – see e.g. Fig. 4.19(e).

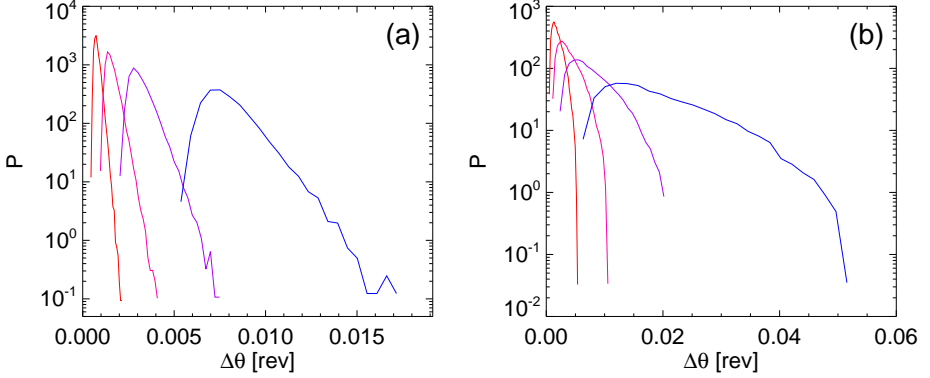


FIGURE 4.18: The distributions of  $\Delta\theta$  for examples of slow flow (a) and fast flow (b) for  $\Delta t = 1/63, 2/63, 4/63, 10/63$  s. The center of the distributions move to larger  $\Delta\theta$  for larger  $\Delta t$ , which indicates that the fluctuations do not dominate the signal and that a clear average  $l$  can be extracted. The precise shape of the distributions depends on the distance to the critical point and will be discussed below.

We proceed our analysis by calculating the variance of  $\Delta\theta$ ,  $\sigma_{\Delta\theta}^2$  (equivalent to the mean squared displacement) as a function of  $\Delta t$ , and plot  $\sigma_{\Delta\theta}^2/\Delta t$  as function of  $\Delta t$  in Fig. 4.19(b,d,f). For ballistic behavior,  $\sigma_{\Delta\theta}^2/\Delta t$  grows linearly with  $\Delta t$ , whereas for a diffusive system,  $\sigma_{\Delta\theta}^2/\Delta t$  is a constant (we divide by  $\Delta t$  because it is easier to identify a plateau than a line with slope 1). In Fig. 4.19, we see both kinds of behavior, and observe ballistic behavior for small  $\Delta t$  and a crossover to a plateau at long times. The fact that the crossover occurs for  $\Delta t > 1/63$  s, agrees with our claim that we are allowed to differentiate  $\Delta\theta$  on a time scale of  $1/63$  s to obtain  $\omega$ .

For most of our data we do not observe a nice plateau, but instead, see the curve bend up again for  $\Delta t > 100$  s (see for example Fig. 4.19(b,f)). This, we believe, is caused by longer time scale fluctuations beyond the scope of this analysis. For even larger  $\Delta t$ , the curve drops because the magnitude of the fluctuations in  $l$  is limited and cannot grow indefinitely as it does for a diffusive system.

To obtain  $\sigma_c^2$  and  $\tau_c$ , we fit  $\sigma_{\Delta\theta}^2$  with Eq. 4.10 and overplot the fit in red. As a result of the long time scale fluctuations and the finite measuring time, the fit is not always good for large  $\Delta t$ . However, as we shall see

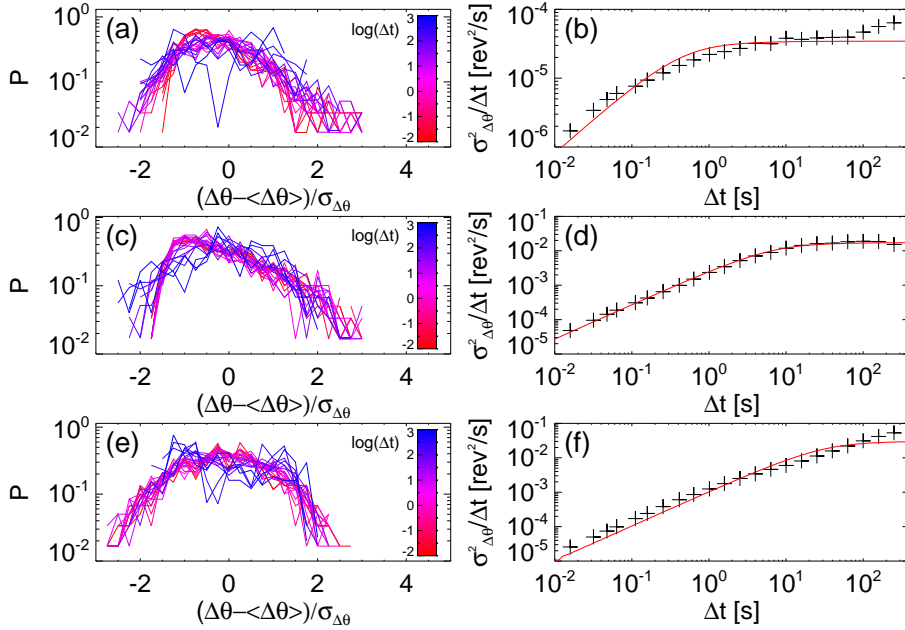


FIGURE 4.19: The rescaled distributions  $(\Delta\theta - \langle\Delta\theta\rangle)/\sigma_{\Delta\theta}$  and  $\sigma_{\Delta\theta}^2/\Delta t$  as function of  $\Delta t$  for slow flow ( $\Gamma^* = 0.09$ ,  $T^* = -0.033$  (a-b)), intermediate flow ( $\Gamma^* = 0.09$ ,  $T^* = -0.0044$  (c-d)) and fast flow ( $\Gamma^* = 0.09$ ,  $T^* = 0.15$  (e-f)). The data in (f) does initially start to flatten, but never reaches its plateau and then bends up again. The resulting shape cannot precisely be fitted with Eq. 4.10. However, reasonable values for  $\sigma_c^2$  and  $\tau_c$  can still be extracted.

in Sec. 4.5.6, the region where the fit is good, is large enough to extract proper values for  $\sigma_c^2$  and  $\tau_c$ .

#### 4.5.5 Locating the Critical Point

Before we can proceed to the scaling of the time scale and magnitude of the fluctuations with  $\Gamma^*$ , we have to identify  $\Gamma_c$ . Finding the critical point is more difficult in stress-controlled than in rate-control experiments. In rate control, we simply plot  $\chi^{-1}$  and determine the zero crossing, but in stress control, this is much harder to determine since we cannot measure the “negative slope” parts of the flow curves. In addition, we have very few data points around the inflection point, because a small increase in  $T$



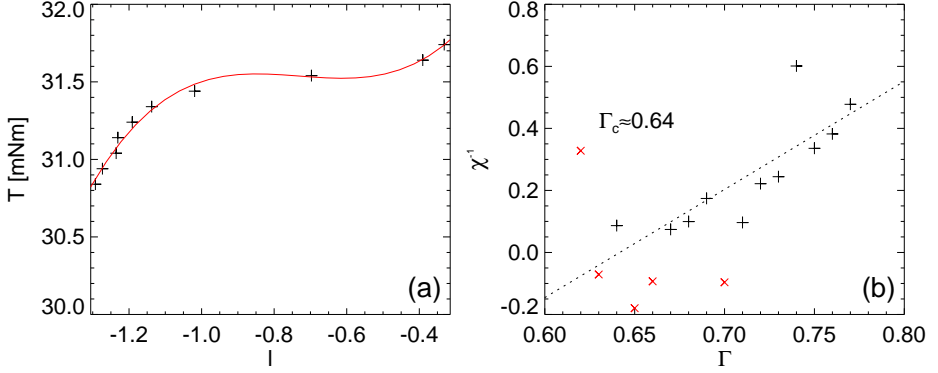


FIGURE 4.20: (a) The flow curve for  $\Gamma = 0.65$  and a fit with Eq. 4.2. (b) The slope at the inflection point,  $\chi^{-1}$ , as a function of  $\Gamma$ . We fit the data to obtain  $\Gamma_c$  and find  $\Gamma_c = 0.64 \pm 0.03$ .

results in a large increase in  $\Omega$  near the critical point – the grids of data points in torque or rate control are different.

In Fig. 4.20(a), we show the flow curve, measured in  $T$ -control, for  $\Gamma = 0.65$ . In red, we add a fit with Eq. 4.2 to obtain a value for  $\chi^{-1}$ . We do this for all  $\Gamma$ , and plot all the values of  $\chi^{-1}$  vs  $\Gamma$  in Fig. 4.20(b) (measuring flow curves in stress control will be discussed in more detail in App. 4.A.2). We want to compute where this relation crosses zero. For certain  $\Gamma$ , there is so little data around the inflection point that the fit yields an unrealistic (typically negative) value for  $\chi^{-1}$ . We decide to not take these points into account and draw them in red ( $\times$ ). Using the rest of the data (indicated by black (+)), we find  $\Gamma_c = 0.64 \pm 0.03$ .

As an alternative method, we can look at the fluctuation data to determine  $\Gamma_c$ . As explained in Sec. 4.5.1, the  $\omega(t)$  signal is bistable in the hysteretic regime. This means that here, a pdf of  $\omega(t)$  will be multi-humped.  $\Gamma_c$  is then the smallest value of  $\Gamma$  for which we do not observe this bistable behavior. In Fig. 4.21(a) we show the distributions for  $\Gamma = 0.65$  and 10 increasing values of  $T$ . For low  $T$ ,  $P$  is nearly Gaussian and as  $T$  increases, a new local maximum develops at large  $\omega$ . Moreover, as  $T$  crosses through  $T_i$ , the center makes a big jump towards an  $\omega$  that corresponds to fast flow.  $P$  now again takes a Gaussian shape.

To decide if a certain  $P(\omega)$  is multi-humped, we want to identify its local maxima. We do this as follows: for slow flow, we find the maximum

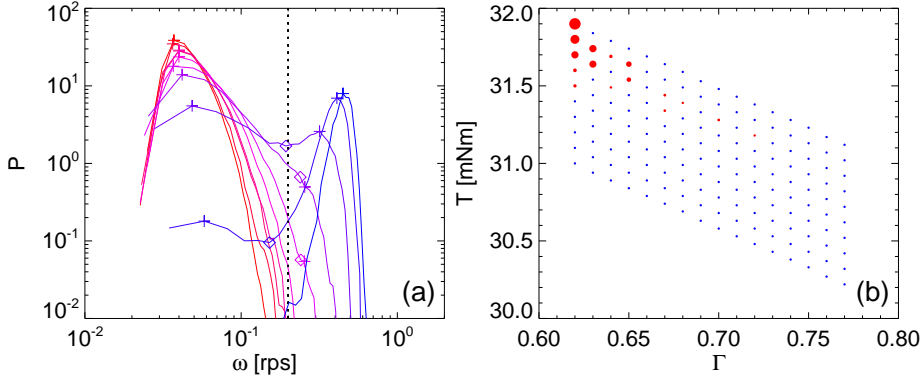


FIGURE 4.21: (a) Distributions  $P(\omega)$  for  $\Gamma = 0.65$  and varying  $T$ .  $P$  goes from monostable slow flow (red) via bistable (purple) to monostable fast slow (blue). The  $+$  and  $\diamond$  symbols indicate the local minima and maxima of  $P$ . The black dashed line at 0.2 rps represents the separation between slow and fast flow. (b) Identification of the bistable (red) and monostable (blue) points in  $T, \Gamma$ -space. The size of the dot represents  $H$  (see Eq. 4.20).

of the curve (we call this  $s_+$ ) for  $\omega < 0.1$  rps, for fast flow, we take  $f_+$  for  $\omega > 0.25$  rps. For intermediate flow rate, we identify the minimum  $i_-$  for  $0.1 \text{ rps} \leq \omega \leq 0.25 \text{ rps}$ . We now say  $P(\omega)$  is bistable if  $s_+ > i_-$  and  $f_+ > i_-$ , and both  $s_+$  and  $f_+ > 0.1$  (to eliminate hits where in a low, noisy tail, a local maximum, by accident, is larger than the center dip). To quantify the bistability of  $P(\omega)$ , we define:

$$H = \min \left( \frac{s_+}{i_-}, \frac{f_+}{i_-} \right) - 1 ; \quad (4.20)$$

for monostable curves, we define  $H \equiv 0$ . In Fig. 4.21(b) we show our data set 2 in  $(T, \Gamma)$ -space where a blue or a red point respectively indicates a monostable or bistable state. The size of the data point represents  $H$ . There is a clear blob of large red points for  $\Gamma \leq 0.65$  which suggests  $\Gamma_c \approx 0.65$ . However, for larger  $\Gamma$ , there are still some bistable points, but the corresponding  $H$  is very low. This means that close to the Widom line, the fluctuations can be large for  $\Gamma > \Gamma_c$ , but the pdf is just broad and does not indicate significant bistable behavior.

The methods of Fig. 4.20 and Fig. 4.21 result in a similar value for  $\Gamma_c$ . The large fluctuations at the Widom line make it difficult to be very

precise, but we estimate  $\Gamma_c = 0.65 \pm 0.01$  and  $T_c = 31.6 \pm 0.1$  mNm. This value for  $\Gamma_c$  differs significantly (30%) from the one that was found for the rate-controlled measurements in Sec. 4.4. This is surprising and shows that, at least around  $\Gamma_c$ , rate and stress control experiments are not simply physically equivalent. We believe that the reason for this lies in the nature of the fluctuations, which are different in rate- (because of the feedback loop of the rheometer) and in stress-controlled experiments.

### 4.5.6 Scaling of Fluctuations

We want to study the scaling of the magnitude and time scale of the fluctuations with the distance to the critical point. Before we can do this, we need to carefully define which quantities we will consider exactly for the scaling.

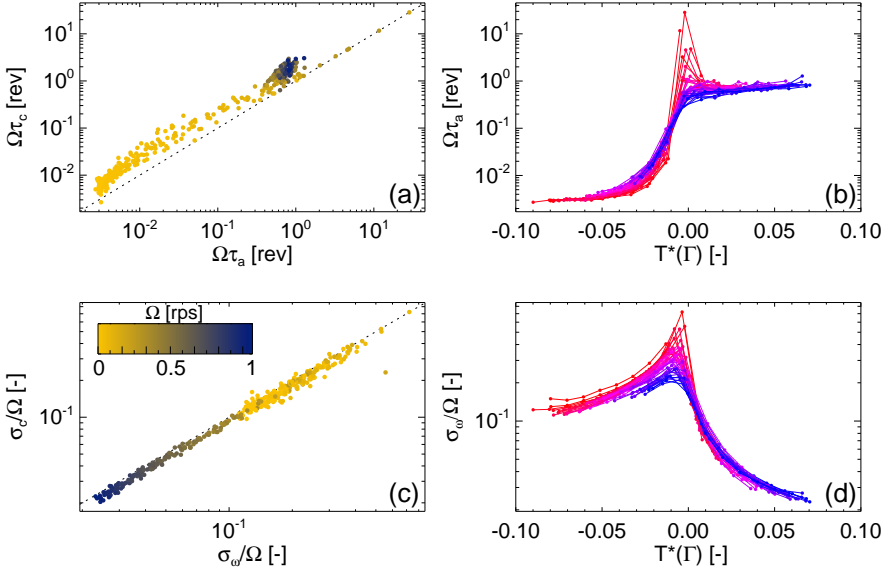


FIGURE 4.22: (a) The relation between  $\tau_a\Omega$  (from the autocorrelation) and  $\tau_c\Omega$  (from the crossover from ballistic to diffusive in  $\sigma_{\Delta\theta}^2(\Delta t)$ ) is linear. (b)  $\tau_a\Omega$  as function of  $T^*$ , color coded by  $\Gamma$ , where red indicates a  $\Gamma$  close to  $\Gamma_c$ . (c) The good correspondence between  $\sigma_w/\Omega$  and  $\sigma_c/\Omega$ . (d)  $\sigma_w/\Omega$  as function of  $T^*$ .

We have determined two different *time scales*:  $\tau_a$ , from the autocorrelation function, and  $\tau_c$  from the crossover from ballistic to diffusive in  $\sigma_{\Delta\theta}^2(\Delta t)$ . Of course, there is another time scale in our system, which is  $\Omega$ . To correct our time scales for this overall time scale  $\Omega$ , we will consider the scaling of the characteristic strain  $\tau_a\Omega$ . In Fig. 4.22(a), we show a scatterplot of  $\tau_a\Omega$  vs  $\tau_c\Omega$ . It shows that there is a great proportionality between  $\tau_a$  and  $\tau_c$ , and hence the two different methods we used to extract a time scale from the data.

In Fig. 4.22(b) we show  $\tau_a\Omega$  as a function of  $\Gamma^*$  and  $T^*$ . We find that these curves have similar shape and there is a systematic trend that  $\tau_c\Omega$  increases when approaching the critical point either in the  $\Gamma$  or in the  $T$  direction. This is similar to critical phenomena, for which the time scale diverges towards the critical point.

To characterize the *magnitude* of the fluctuations we also have two options. First, we take the derivative of  $\theta(t)$ ,  $\omega(t)$ , and take its variance  $\sigma_\omega^2$  as a measure for the fluctuations. Alternatively, from fitting  $\sigma_{\Delta\theta}^2(\Delta t)$  with Eq. 4.10, we get a fluctuation magnitude  $\sigma_c^2$ . To get a dimensionless magnitude, we will consider  $\sigma_\omega/\Omega$ . In Fig. 4.22(c) we plot  $\sigma_c/\Omega$  vs  $\sigma_\omega/\Omega$  and see a nearly perfect correspondence. This means that we are confident that we have extracted a proper magnitude of the fluctuations. In (d), we show  $\sigma_\omega/\Omega$  as a function of  $T^*$  and  $\Gamma^*$ . In this case, very clearly,  $\sigma_\omega/\Omega$  increases towards the critical point both in the  $T$  and  $\Gamma^*$  direction. Since the data peaks at  $T^* = 0$  for all  $\Gamma$ , this data is very suitable to determine the scaling of  $\sigma_\omega/\Omega$  with  $\Gamma^*$ .

To test the scaling relations (Eq. 4.11, 4.12), we want to investigate how  $\tau_a\Omega$  and  $\sigma_\omega/\Omega$  scale with  $\Gamma^*$ . As explained in Sec. 4.3, we take the values of  $\tau_a\Omega$  and  $\sigma_\omega/\Omega$  at the inflection point for each  $\Gamma$ . There is however the complication that in  $T$ -controlled experiments, we do not have much data close to the inflection point – see Fig. 4.20(a). To account for this problem, we want to estimate what the value of  $\sigma_\omega/\Omega$  would be precisely at  $T_i$ . We do this by finding the maximum of  $\sigma_\omega/\Omega(T)$  by performing a fit. We find that the best way to find the maximum is by plotting  $\sigma_\omega/\Omega(l)$ . In this representation, we find that we can fit the data for all  $\Gamma$  using a Gaussian as functional form:

$$\sigma_\omega/\Omega = a + b \cdot \exp\left(\frac{-(l - l_i)^2}{d}\right). \quad (4.21)$$

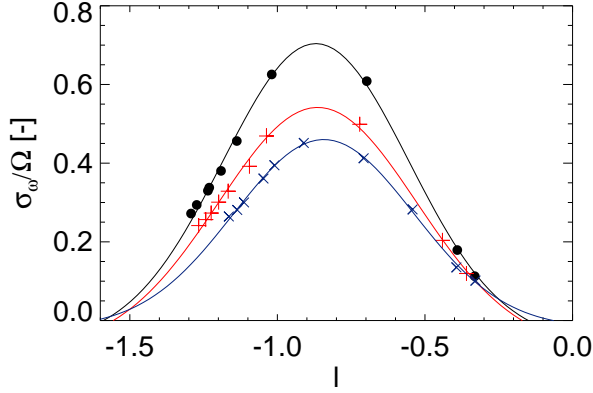


FIGURE 4.23: To estimate the value of  $\sigma_\omega/\Omega$  exactly at the inflection point, we fit  $\sigma_\omega/\Omega(l)$  with Eq. 4.21. The three examples presented here are for  $\Gamma^* = 0.019$  (black  $\bullet$ ),  $0.097$  (red  $+$ ) and  $0.18$  (blue  $\times$ ).

In Fig. 4.23 we show that this works well for  $\Gamma^* = 0.019, 0.097$  and  $0.18$ . The value of the maximum is then simply extracted from the fit as  $a + b$ . We note that we found this fit function empirically and have no reason to believe that Eq. 4.21 is an actual scaling function.

In Fig. 4.24 we show the peak values of  $\tau_a\Omega$  (a) and  $\sigma_\omega/\Omega$  (b) at the inflection point as a function of  $\Gamma^*$ . We combine the data of data set 1 (black) and data set 2 (yellow) to cover a larger range in  $\Gamma^*$ . We see that both  $\tau_a\Omega$  and  $\sigma_\omega/\Omega$  depend on  $\Gamma^*$  via a power-law, and want to extract the corresponding critical exponents. Note that, as we now look at the standard deviation  $\sigma_\omega$  rather than the variance, we also have to take the square root of Eq. 4.11, which means we now obtain a value for the critical exponent  $\gamma/2$ .

The values of the exponents strongly depend on the value of  $\Gamma_c$ . Because of the error bar on  $\Gamma_c$ , we decide to neglect the data with  $\Gamma^* < 0.05$  (indicated by the dotted line in Fig. 4.24). We fit the data with a power-law (plotted in red) and find  $\nu = 0.94 \pm 0.47$  (mean field:  $\nu = 1/2$ ) and  $\gamma/2 = 0.47 \pm 0.22$  (mean field:  $\gamma/2 = 1/2$ ).

For  $\gamma$ , our data is consistent with the mean field value  $\gamma = 1$ , both for the slope at the inflection point of the flow curve and the magnitude of the

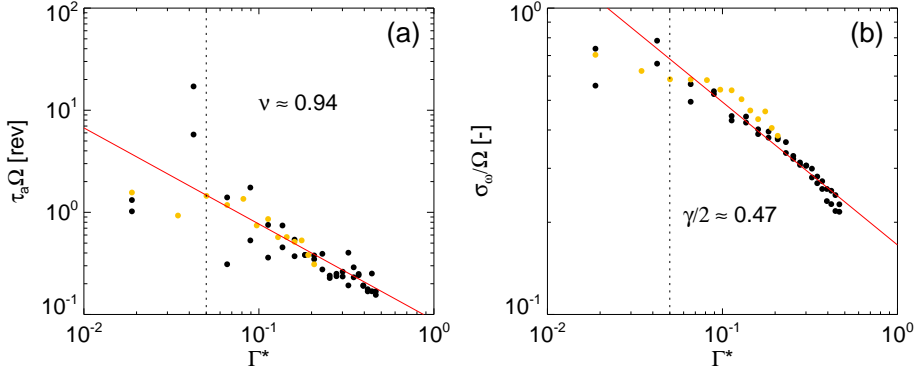


FIGURE 4.24:  $\tau_a \Omega$  (a) and  $\sigma_\omega / \Omega$  (b) as found using the fit with Eq. 4.21 as a function of  $\Gamma^*$ . The black data is for data set 1, the yellow data for data set 2. We fit the data with a power-law (plotted in red) and find  $\nu = 0.94 \pm 0.47$  and  $\gamma/2 = 0.47 \pm 0.22$ .

fluctuations. This supports our picture (Eq. 4.1) that the fluctuations for certain  $T$  and  $\Gamma$  are closely related to the local slope of the flow curve. If the  $T(\Omega)$  flow curve is flatter, the corresponding fluctuations are larger.

The exponent  $\nu$ , corresponding to the time scale, deviates from the mean field value (even though the mean field value of  $1/2$  is just within the error bar). We interpret this as an indication that the mean field description is not capable of governing the details of the fluctuation measurements. The value we find for  $\nu$  is larger than its mean field equivalent, which means  $\tau_a \Omega$  decreases faster with  $\Gamma^*$  than it does in a mean field system. The deviation in the value for  $\nu$  suggests that the slow and the fast flowing branches are, compared to a mean field system, relatively stable close to  $\Gamma_c$ . This is a useful observation towards precisely understanding the two flowing states.

The second step in investigating the scaling of  $\tau_a \Omega$  and  $\sigma_\omega / \Omega$  is to consider their complete scaling with  $\Gamma^*$  and  $T^*$ , rather than only approaching the critical point via the inflection points of the flow curves. To achieve this we try to find a scaling function of the form [112]:

$$\Omega \tau_a \text{ or } \sigma_\omega / \Omega = \frac{1}{\Gamma^* \Delta} \mathcal{F} \left( \frac{T^{*\gamma}}{\Gamma^*} \right), \quad (4.22)$$

however, due to a limited amount of data (very close to the critical point), uncertainty in the value of  $\Gamma_c$ , and an asymmetry between slow and fast flow (even though the scaling could in principle be different on both sides of the transition), we are unable to find such a scaling relation.

**Conclusion** – In this section we have shown that we can extract robust values for the magnitude and time scale of the fluctuations in the stress-controlled experiments. The scaling of the magnitude agrees with the scaling of the slope at the inflection point of the flow curves and the corresponding mean field exponent. The exponent that we find for the scaling of the time scale is larger than its mean field equivalent. This suggests that the average quantities in our system do agree with a mean field description, whereas the fluctuations show deviations. This, in turn, is a reflection of the differences between the slow and fast flowing states in our system and the states in mean field systems.

## 4.A Appendix

### 4.A.1 Collective Behavior

A fundamental property of a second-order critical point is collective behavior of the particles, which arises in the correlation length  $\xi$ . We have searched for this in two different ways.

First, we have studied the location and width (and their fluctuations) of the shear band, as well as the precession of the core for varying  $T$  and  $\Gamma$ . We found that the flow structure is actually very robust, with an only exception for the moving shear band for high  $\Gamma$  and small  $\Omega$  (see Sec. 3.4.3), which we believe is not related to our critical point.

Second, we have looked at so-called kymographs of pictures of the surface of the system. For this, we identify a circular path on the surface that the particles follow. We then make a 2D picture where each horizontal line corresponds to the same image line, but a different moment in time. This way, the trajectories of all the particles on the identified path are visualized. We took kymographs close and far from the critical point in  $(T, \Gamma)$ -space, but found no significant differences.

Of course, our system is relatively small (the shear band is only a few particle wide), the particles are incompressible, and we can only observe what happens at the surface. Therefore, not only is it physically hard to imagine a certain blob of particles moving at a different speed than the adjacent blobs, even if it does happen, it would be hard to observe [113].

### 4.A.2 $T$ -Control Flow Curves

In Sec. 4.4 we discussed flow curves that were measured in  $\Omega$ -control. To look at the transition between slow and fast flow from a different perspective, we measure an additional set of flow curves in  $T$ -control and plot them on a double linear scale.

The data is presented in Fig. 4.25. In (a), we first plot the  $\Omega(T)$  flow curves in the usual logarithmic  $\Omega$ -axis representation, and see that they are of similar shape as the curves that are measured in rate control (note that the  $T$  and  $\Omega$  axis are interchanged compared to our usual  $\Omega$ -control plots such as Fig. 4.1). The main difference is the absence of the negative slope, which is replaced by a discontinuous jump in the data for  $\Gamma < \Gamma_c$ .



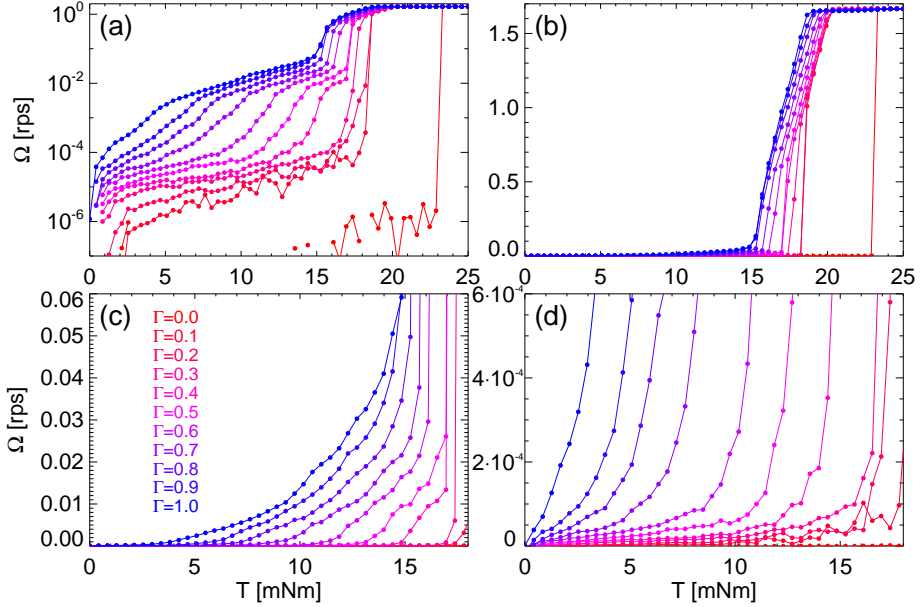


FIGURE 4.25: Flow curves measured in  $T$ -control plotted on log-lin (a) and lin-lin (b-d), where (c-d) are zoom ins of (b). The curves are bounded by  $\Omega = 1.66$  rps which is the maximum rotation rate of the rheometer. The different flow regimes that we can identify using this representation are discussed in App. 4.A.3.

The curves are bounded by  $\Omega = 1.66$  rps, which is the maximum rotation rate of the rheometer.

In panels (b-d) we plot the data in a lin-lin representation. In (b), we see the fast flow regime where  $\Omega$  grows linearly with  $T$ . The curves are parallel to each other, which indicates that the flow rate is mostly determined by the stress, where the vibrations are just a small correction. In (c-d), we zoom in to the slow flow regime. For very small  $T$ ,  $\Omega(T)$  seems linear, and above a certain “kink”, it increases exponentially. In App. 4.A.3 we will use these observations as ingredients towards finding a simple model to describe the flow of weakly vibrated granular media.

### 4.A.3 Towards a Simple Model

We want to see if we can introduce a simple heuristic model similar to those of Bocquet *et al.* [114–116], Kamrin *et al.* [68–70], and Kuwano *et al.* [87] to describe the transition from slow to fast flow. The key ingredient of this model is that we consider the granular system from the point of fluidity, which is a result of both the vibration and the flow itself.

In flow curves such as the ones in Fig. 4.25, we can identify four different regimes. (i) For finite  $\Gamma$  and very low  $\Omega$ ,  $\Omega(T)$  is linear. We interpret this by saying that the vibrations fluidize the grains to become a very viscous liquid-like material where stable, slow flow is possible. (ii) For faster rates,  $\Omega(T)$  becomes curved upwards, where a higher flow rate requires a relatively small increase in  $T$ . This is, we believe, due to self-fluidization caused by the flow itself. The flow makes the system more fluid, so at similar  $T$ , it can now flow faster. (iii) For  $\Gamma^* < 0$ , there is a jump in stress-controlled, and a negative slope in rate-controlled experiments. This is perhaps the hardest regime to understand. Apparently, there is a  $\Gamma$ -dependent “yield” torque above which the system jumps to the inertial regime. In rate control, we *can* access these “forbidden” speeds that correspond to the jump. However, we know that there is no constant  $T$  which leads to an  $\Omega$  in this regime, so  $T$  *has* to fluctuate. Here, the fluidity picture offers an explanation for the negative slope. In the case of a relative slow, forbidden,  $\Omega$ , the rheometer often has to impose a large  $T$  to rebreak the contacts to allow for a forbidden rate. For a relatively fast, but forbidden,  $\Omega$ , the system is very fluid, so the fluctuations to large  $T$  (to sustain the flow) can be smaller. For  $\Gamma^* > 0$ , regime (iii) does not exist, and the self-fluidizing regime (ii) is directly connected to the inertial flow branch. (iv) In the inertial regime [90],  $\Omega(T)$  is linear, but the relation does not cross the origin. We explain this as follows: the  $T$  splits into two contributions, one to completely break the contacts and one to sustain the fast flow. In this regime,  $T(\Omega)$  still depends on  $\Gamma$ . We believe this is because, at higher  $\Gamma$ , a smaller portion of  $T$  is required to break the contacts, so more  $T$  is left to reach a higher flow rate.

We hope to concretize this concept either by finding analytic expressions for  $T(\Omega, \Gamma)$  and  $\Omega(T, \Gamma)$ , or by developing an iterative simulation that, for each time step, compares  $T$  with the current fluidity, and adapts the rate accordingly.

# THE ROLE OF ANISOTROPY IN GRANULAR FLOW

## 5.1 Introduction

In this chapter we study the influence of the anisotropy of a granular packing on its flow and rheology. When a granular system is sheared, the particles rearrange and form a dilated, anisotropic packing [47, 117–124]. We believe that the buildup and release of anisotropy influences many granular experiments, typically during transients and reversals. In this chapter we will develop a method to measure the anisotropy *explicitly*.

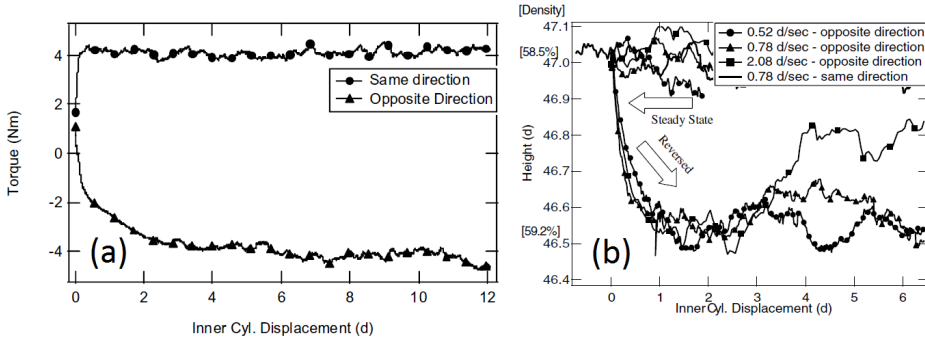


FIGURE 5.1: (a) Torque as a function of strain for a flow reversal experiment. When a fully disordered packing is first sheared, is it isotropic and the required  $T$  is low. After a strain of about a grain diameter, the steady state  $T$  is reached. When reversing the flow direction (bottom curve), the required  $T$  initially is very low. (b) The height and density of the packing. Upon reversal, the packing compacts. Image from [117].

An example where the anisotropy plays a role is an experiment by the group of W. Losert, where the flow of a granular material is investigated in a Taylor-Couette geometry [117]. The emphasis of this work is the response of the flow to a reversal of the flow direction. Two main figures from the paper are shown in Fig. 5.1. In (a), the torque that is required to shear the system, is plotted as function of the strain. Initially, there is a short transient where, for very low strain, the torque is very low. After this stage, when a steady state anisotropy and density have been reached, the system is in a steady state and  $T \approx 4$  Nm. When the flow is reversed, there is a new transient where, initially,  $T$  is very low and the packing compacts (b). After a transient in the strain of around 5 particle diameters, a new steady state is reached. This experiment shows the influence of the anisotropy of the packing: both the rigidity and the density of the packing change when the shear is reversed. Similar results are also found in a frictionless system [118].

In general, the anisotropy of the packing resists shear. This can also be seen in the force chains that are formed in the direction *counter* to the flow [118, 119]. This is visualized in Fig. 5.2, which is made using photo elastic disks [118]. In the figure, the white arrow indicates the flow direction; the white lines through the particles are the visualization of the force chains.

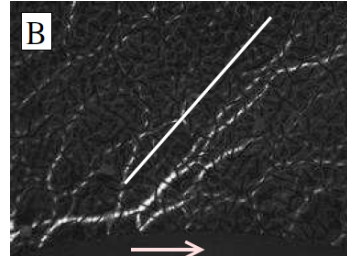


FIGURE 5.2: Using photo elastic disks, the force chains, directed opposite to the flow, can be visualized [118].

In a third example, the rheological curve  $T(\Omega)$  of a granular material is measured in the split-bottom geometry [47]. At the bottom of the container there is a rotating disk which fluidizes the system [38] (main flow). Higher up in the system, the flow curves are measured via the rotation of a vane (secondary flow) connected to a rheometer for different rates of the bottom disk. It is found that, in the absence of any main flow, the probe experiences a clear yield stress, whereas for any finite flow rate, the yield stress disappears and the secondary rheology takes on the form of a double exponential relation between  $\Omega$  and  $T$ . This secondary rheology does not only depend on the magnitude of  $T$ ,

but is anisotropic – which is shown by varying the relative orientation of the probe and main flow [47].

We perform our experiments of the anisotropy with the setup that was introduced in Sec. 2.2. The basic idea is as follows: we prepare a system by shearing it in rate control until we reach a steady, critical state [125], with a certain constant torque and anisotropy. When we then just vibrate this packing, the vibrations will relax the anisotropy, which leads to a small rotation of the disk in the direction counter to the direction of the initial shear. We measure this rotation with the rheometer, where a larger rotation means that the packing was more anisotropic. This explicit way to measure the anisotropy is a beautiful example of what is possible with our experimental setup that combines shear and vibration.

	Anisotropy	Density
Flow	increase	decrease
Vibrations	decrease	increase

TABLE 5.1: Flow and vibrations compete in terms of both anisotropy and density.

We study the anisotropy as a function of flow rate  $\Omega$  and vibration intensity  $\Gamma$ . Whereas the flow *builds* anisotropy, the vibrations *relax* the packing. This means that there is a competition between the two, which will eventually lead to a equilibrated value of the anisotropy. Interestingly, this is very similar to density, which is increased by vibrations [126] and decreased by flow [18]. The situation is summarized in Table 5.1. When interpreting the data it is important to be aware of the subtle relation between shear and vibrations and the possible influence of density changes.

## 5.2 Protocol

The protocol that we use to measure the anisotropy is shown schematically in Fig. 5.3. When *building* the anisotropy, we impose a flow rate  $\Omega_{\text{shear}}$  and vibration intensity  $\Gamma_{\text{shear}}$ . When *probing* the anisotropy we impose  $T = 0$  and  $\Gamma_{\text{probe}}$ , where the rotation of the disk is purely caused by the relaxation of the anisotropic packing. The protocol is complex, which originates from the fact that we cannot instantly change from building the anisotropy to measuring it. If we were to abruptly change from finite  $\Omega$  to  $T = 0$ , the inertia of the disk would cause it to keep rotating, which

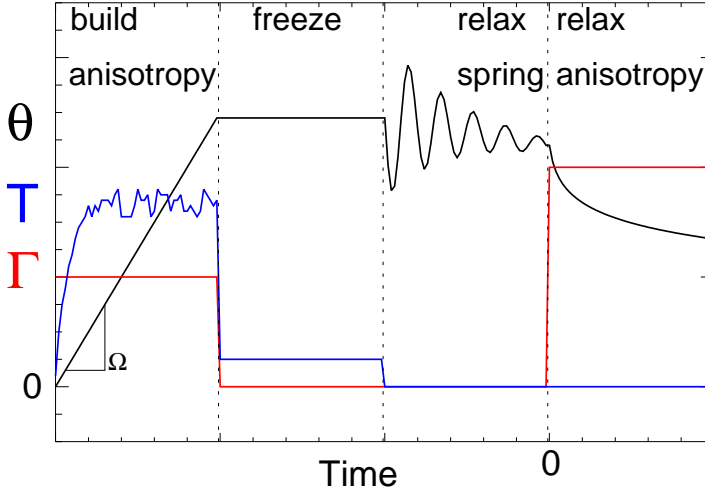


FIGURE 5.3: A schematic representation of the measurement protocol.

would interfere with measuring the relaxation. In addition, the spring, that forms the flexure between the disk and the rheometer, is stretched during the stage when we build the anisotropy. When switching to  $T = 0$ , the spring relaxes, which results in a significant oscillation on the signal. To circumvent these two complications, the following protocol is developed:

*Preshear* (not shown in figure): We start with a preshear that consists of 5 s shear at 1 rps, followed by 10 s shear with -1 rps and again 5 s at 1 rps. We conclude with a waiting period of 10 s during which the system is not sheared. During the entire preshear stage, the vibrations are already switched on at value  $\Gamma_{\text{shear}}$ .

*Stage 1:* This is the stage during which we build the anisotropy into the system. There are two control parameters: the vibration intensity  $\Gamma_{\text{shear}}$  and the constant rotation rate  $\Omega_{\text{shear}}$ . We verify that we reach steady state flow by measuring  $T$  and making sure that it equilibrates. At the slowest  $\Omega_{\text{shear}}$  that we probe, this takes approximately  $1.6 \times 10^4$  s.

*Stage 2:* Since we want the disk to be stationary at the beginning of the measurement of the relaxation, we impose  $\Omega = 0$ . To freeze the anisotropy,

we simultaneously switch to  $\Gamma = 0$ . The system is now frozen, with the anisotropy still present in the packing.

*Stage 3:* Now that the disk is frozen and the rheometer is at  $\Omega = 0$ , the flexure is still stretched. We therefore switch to  $T = 0$  while  $\Gamma = 0$ . The flexure now relaxes without significantly influencing the frozen packing.

*Stage 4:* We switch on the vibration (this moment is defined  $t = 0$  s) and measure the relaxation of the system. We probe at  $\Gamma_{\text{probe}} = 0.4$  and a sample rate of 5 Hz for 28 s. Since the flexure is relaxed and the rheometer axis can rotate freely, there is no difference between the deflection of the axis above and below the flexure (we have verified this with the optical encoder that measures the position below the disk that we introduced in Sec. 4.2). This means we can measure the relaxation using the rheometer.

We perform five measurements for each combination of  $\Gamma_{\text{shear}}$  and  $\Omega_{\text{shear}}$  (except for the  $\Omega < 10^{-5}$  rps, where we measure three times), and average the results thus obtained.

## 5.3 Steady State Relaxation

### 5.3.1 Relaxation Speed

We measure the relaxation for  $\Gamma_{\text{shear}} = 0, 0.2, 0.4, 0.5, 0.6, 0.7, 0.8$  and  $\Omega = 1, 0.316, 0.1, \dots, 10^{-6}$  rps, at  $H/R_s = 0.33$  and  $\Gamma_{\text{probe}} = 0.4$ . In Fig. 5.4(a) we present the raw relaxation curves  $\theta(t)$ , where the color represents the relaxation speed at  $t=0$  s. The relaxation speeds vary over a large range, but for all data, the relaxation becomes slower over time. Apart from some exceptions, the curves do not intersect.

To see how the relaxation varies with  $\Omega_{\text{shear}}$  and  $\Gamma_{\text{shear}}$ , we want to extract a number for the relaxation speed from the  $\theta(t)$ -curve using a fit. From the data in Fig. 5.4(a), we see that the relaxation curves seem to have a logarithmic shape (this cannot be true for all  $t$ , since  $\log(t) \rightarrow \infty$  for  $t \rightarrow \infty$ , whereas our data does not). We find that we cannot fit the data using a 1-parameter fit. The reason for this is that not only the overall relaxation speed, but also the curvature of  $\theta(t)$  varies per data set. To take into account both properties of the relaxation curve, we fit the data with:

$$\theta(t) = a \cdot \log\left(\frac{t+b}{b}\right), \quad (5.1)$$

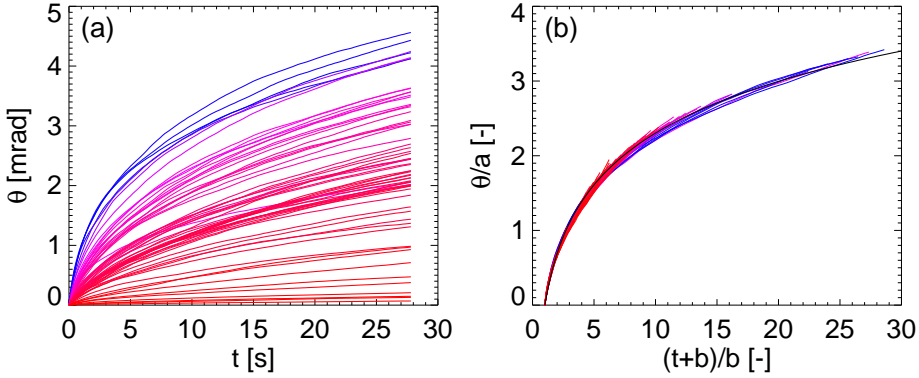


FIGURE 5.4: (a) The raw  $\theta(t)$  relaxation curves. The color represents the relaxation speed at  $t=0$  s. (b) A collapse of the data onto the master curve  $\log[(t + b)/b]$  (plotted in black) using Eq. 5.1.

where  $b$  is a measure for the curvature (a *higher*  $b$  corresponds to *less* curvature), and  $a/b$  is the slope of the relaxation curve at  $t = 0$ . In addition, the fit function is chosen such that  $\theta = 0$  at  $t = 0$ . In Fig. 5.4(b), we show that the fit with Eq. 5.1 works well by using it to collapse the data onto the master curve  $\log[(t + b)/b]$ .

To test if we could fit the data with a 1-parameter fit function, we plot the correlation between the initial slope  $R = a/b$  and the curvature  $b$  in Fig. 5.5(a). We see a correlation where, in general, a faster initial relaxation corresponds to a more curved relaxation curve. However, the relation is quite scattered, which means that a 1-parameter fit would correspond significantly less to the data.

To investigate the quality of the fits, we calculate their standard weighted  $\chi^2$  [127] and show the results in Fig. 5.5(b). It can be seen that the logarithmic fit matches the data better for fast relaxations. This is also visible in the collapse of the raw data in Fig. 5.4(b). Here, the slow (red) relaxation curves do not collapse perfectly, but lay just above the master curve for large  $t$ . We find that, for low  $R$ , the initial relaxation is relatively fast, but for  $t > 5$  s, the curvature is very low (an example is plotted in Fig. 5.10(a)). This results in a shape that does not fully match a logarithm.

Hence, the scatter in Fig. 5.5(a) suggests that it is hard to characterize the relaxation curve with a single parameter, and the correlation in



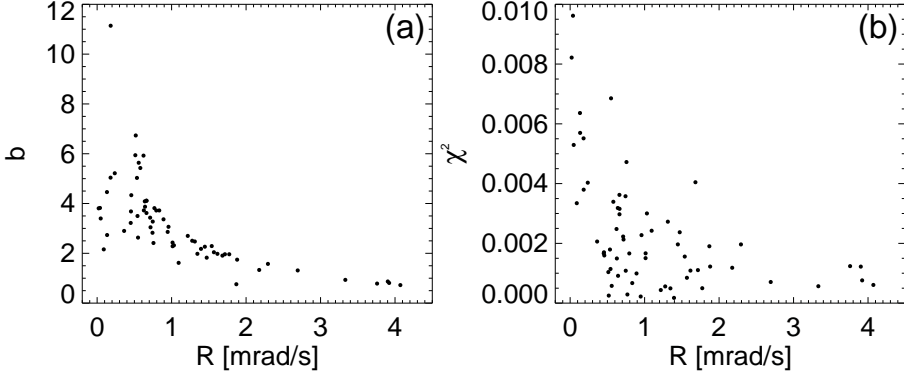


FIGURE 5.5: (a) A scatter plot of the initial relaxation rate  $R = a/b$  versus the inverse curvature  $b$ . There is a clear correlation, however, for low  $R$ , the scatter is large. (b) A scatter plot of the quality of the fit  $\chi^2$  vs  $R$ . There is a trend that the fit is better for faster relaxations.

Fig. 5.5(b) shows that the fit with Eq. 5.1 systematically works better for fast relaxations. However, we already know that the relaxation curves cannot be true logarithms as our data does not go to  $\theta = \infty$ . Moreover, as shown by the relatively low values of  $\chi^2$  and the good collapse in Fig. 5.4(b), the fits do match the data closely. Fig. 5.4 shows that the general shape of the relaxation curves is robust, and the curves do not intersect. Therefore, we are confident that we can characterize the relaxation process by the single parameter  $R$  - defined as the initial relaxation speed at  $t = 0$ ,  $a/b$  - as it is a good proxy for the anisotropy of the frozen state. We have verified that the main results that we report are independent of the precise choice of order parameter.

### 5.3.2 Dependence on $(\Omega, \Gamma)$ and $(T, \Gamma)$

In Fig. 5.6(a) we show  $R$  as function of the control parameters  $\Gamma$  and  $\Omega$ . The red curve corresponds to the case without vibrations,  $\Gamma = 0$ . We see that, for this curve,  $R$  is essentially independent of  $\Omega$ . This is what we expect: at  $\Gamma = 0$ , the flow is rate independent for the range in  $\Omega$  that we measure (except for  $\Omega > 0.1$  rps). As a result, different values of  $\Omega$  correspond to the same anisotropy and  $R$ ; it will only take a different amount of time to reach the steady state. For  $\Omega > 0.1$  rps,  $R$  decreases. We be-

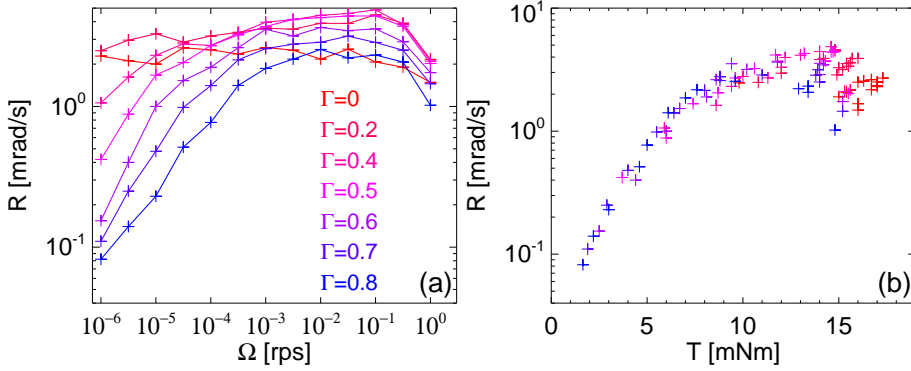


FIGURE 5.6: (a) The relaxation  $R$  as a function of the control parameters  $\Gamma$  and  $\Omega$ . (b) The data collapses when we plot  $R$  as a function of the steady state  $T$  that we measure during stage 1 where we build the anisotropy.

lieve this is caused by the flow itself, which is so fast, that it fluidizes and relaxes the packing. Overall, the values of  $R$  for  $\Gamma = 0$  seem surprisingly low, we will discuss this in Sec. 5.5.1.

For  $\Gamma > 0$ , the situation is more complex. During stage 1, there is a competition between the flow, that is increasing the anisotropy, while the vibrations are relaxing it. For low  $\Omega$ , this results in a monotonic lowering of  $R$  with  $\Gamma$ . Surprisingly, for intermediate  $\Omega \approx 10^{-2}$  rps,  $R$  is non-monotonic in  $\Gamma$  – the relaxation is strongest for  $\Gamma \approx 0.4$ . This means that, even though the system is relaxing during stage 1,  $R$  for  $\Gamma = 0.4$  is larger than for  $\Gamma = 0$ . This suggests that more anisotropy can be built into a weakly vibrated and thus softened packing. There is, however, a second effect that could play a role in our system; density. Contrary to the anisotropy, flow decreases the density [18], while vibrations increase it [126]. From our current data it is hard to determine whether the stronger relaxation is caused by the anisotropy or by the density.

To see how the relaxation is related to  $T$ , we plot  $R$  as a function of the steady state  $T$  and  $\Gamma$  during stage 1 in Fig. 5.6(b). In this representation, we find a nice data collapse, especially for the slow flows. When  $\Gamma$  is increased, the flow rate will be higher for equal  $T$ , but because of the higher vibrations, the anisotropy also relaxes more. The collapse indicates that, in terms of relaxation, these two effects cancel. In other words: it

is the  $T$  that sets how much anisotropy is built into the system, or even: it is the anisotropy that determines how much  $T$  is required for the flow. The concept that a stress-dependent back stress is generated in sheared granular materials, is also known from geophysical kinematic hardening models [128].

The data collapse in Fig. 5.6(b) also implies that when trying to understand granular flow and searching for a constitutive relation [68–70, 90], the anisotropy is a relevant factor that should be taken into account.

### 5.3.3 Conclusion

In this section we studied how anisotropic a packing becomes after shearing at certain  $\Omega$  and  $\Gamma$ . After a certain strain, a steady state is reached where the effects of shear (that builds anisotropy) and vibrations (that release it) balance. We can then measure the anisotropy by probing how fast the packing relaxes ( $R$ ) as we impose  $T = 0$  while vibrating.

We find that for  $\Gamma = 0$ ,  $R$  is constant. For  $\Gamma > 0$ , as expected,  $R$  decreases with decreasing  $\Omega$ . Surprisingly, for  $\Omega \approx 0.01$  rps,  $R$  is non-monotonic in  $\Gamma$ . This suggests that  $R$  could be determined by two physical properties of the system, likely the anisotropy and the density.

## 5.4 Dynamics of Anisotropy

In the previous section we studied the relaxation of sheared packings that were in *steady state*; here we will investigate how the anisotropy builds up by measuring the relaxation of packings that are in a *transient* state.

We focus on two questions. First, we probe whether the anisotropy has a unique steady state, by studying its evolution from state 1 to state 2, varying state 1. Second, we investigate how the relaxation curves  $\theta(t)$  evolve during the transient between two steady states.

We begin by discussing the transient to a steady state from the pre-sheared state in Sec. 5.4.1. In Sec. 5.4.2 we discuss the results of experiments with an extended protocol, involving two different stages whose  $\Gamma$ ,  $\Omega$ , and duration we vary independently.

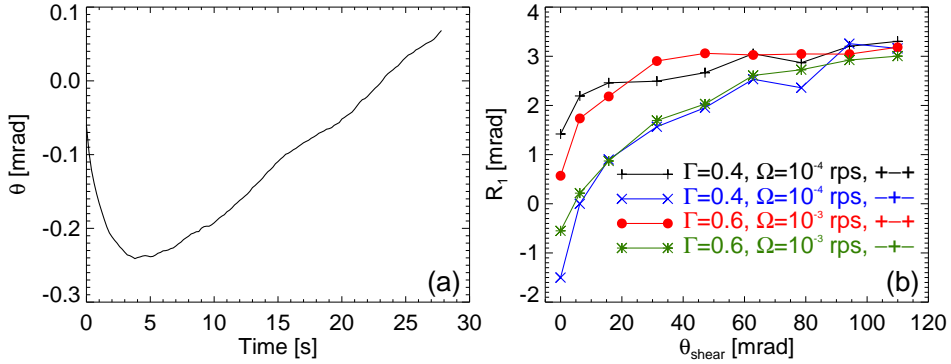


FIGURE 5.7: (a) Complex relaxation curve where different parts of the system have opposite anisotropy. This situation occurs when the last stage of the preshear is opposite to the flow during the evolution stage. (b) The dependence of  $R_1$  on the strain during the evolution stage.

### 5.4.1 Relaxing from Preshear to Steady State

The packing that we create with the preshear protocol is well-defined and reproducible, but already anisotropic. This implies that during the evolution stage of the protocol of Fig. 5.3 (stage 1), the anisotropy evolves from an already anisotropic state. Because of the large range of shear rates  $\dot{\gamma}$  that are present in split-bottom flow, the local transient time scale can be expected to vary with location, and the global relaxation time is not easily guessed. Moreover, the relative direction of preshear and evolution stage matters. If the last stage of the preshear was in the counterclockwise (−) direction, and the evolution stage is in the clockwise (+) direction, during the transient, different parts of the packing will have opposite anisotropies. An example of the complex, non-monotonic relaxation curves that result from this is shown in Fig. 5.7(a), where we believe that at different times, different locations in the system dominate the relaxation process. Of course, a complex relation curve such as in Fig. 5.7(a) cannot be fitted with Eq. 5.1. Therefore, we use the alternative  $R_1$  to characterize the relaxation, which is defined as the angle that the disk rotates back during the first 28 s.

To probe the duration of the transient, we determine the plateau where  $R_1$  does no longer depend on the amount of shear during the evolution

stage  $\theta_{\text{shear}}$ . In Fig. 5.7(b) we investigate this for  $\Gamma = 0.4$ ,  $\Omega = 10^{-4}$  rps and  $\Gamma = 0.6$ ,  $\Omega = 10^{-3}$  rps. The preshear always consists of three phases, but we vary in which direction the last phase is. We can either start in the (+) direction, then do (−) and end in (+) (in Fig. 5.7(b) we label this as  $++$ ), or the opposite (−−). The evolution stage is always performed in the (+) direction. The data in Fig. 5.7(b) shows that, for the  $++$  preshears,  $R_1$  is negative for small  $\theta_{\text{shear}}$ , which indicates that the overall anisotropy is dominated by the preshear. For  $\theta_{\text{shear}} \gtrsim 100$  mrad,  $R_1$  takes a constant value, independent of whether the preshear was  $++$  or  $--$ . This shows that the steady state anisotropy has been reached, and that the corresponding value of  $R_1$  is independent of the direction of preshear. We note that all steady state data in Sec. 5.3 was taken for  $\theta_{\text{shear}} \geq 100$  mrad. The final stage of the preshear, at the fast rate of 1 rps, has been imposed for a large strain of  $3 \times 10^5$  mrad.

### 5.4.2 Two Stage Relaxation

In the experiments that were described in Sec. 5.3 and 5.4.1, relaxation from fast preshear to steady flow was studied. To probe how the material's internal structure evolves with time, we now extend the experimental protocol such that it contains two consecutive evolution stages during which we shear the system at fixed  $\Gamma_i$  and  $\Omega_i$ . In this extended protocol there are two transients, first from the preshear to stage 1 (with reversal), then from stage 1 to stage 2 (without reversal). Since we are interested in the time evolution of the anisotropy, the strain in each stage (measured in terms of the angle  $\theta_i$ ) is a crucial control parameter. This results in a total of six control parameters for the experiment:  $\Omega_1$ ,  $\Gamma_1$  and  $\theta_1$  during stage 1, and  $\Omega_2$ ,  $\Gamma_2$ ,  $\theta_2$  during stage 2. The precise protocol is shown in Fig. 5.8.

We will address several questions using the two stage relaxation. First, by varying the flow in stage 1, we will probe whether the anisotropy of stage 2 is unique. Second, we will examine how the relaxation curve evolves during the transient in between steady states.

**Results** – In Fig. 5.9 we show the main results of the experiments, all for  $H/R_s = 0.6$  and  $\Gamma_{\text{probe}} = 0.8$ . As in the previous section, we measure each relaxation five times and report the average, where the error bars represent the standard deviation over the five runs. We note that, once the relaxation has been measured, it is impossible to restart the flow and simply

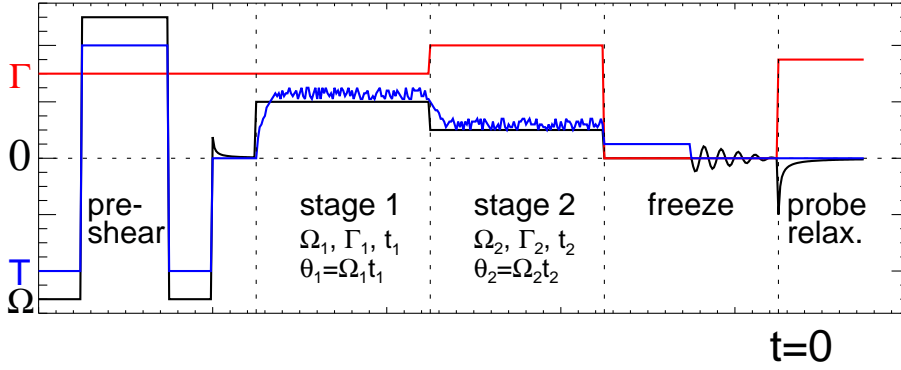


FIGURE 5.8: The extended protocol where there are two evolution stages after the pre-shear. There are two transients, one from the preshear to the first stage, the other from the first to the second stage. The parameters that characterize a stage are  $\Omega_i$ ,  $\Gamma_i$ , and the total disk rotation  $\theta_i$ .

measure the next data point. Therefore, for each measurement, we have to start from the beginning (with the preshear). As a consequence, the measurements performed with the extended protocol are relatively time consuming. Also note that for small  $\theta_1$ , complex relaxation curves such as in Fig. 5.7(a) occur, so that we cannot fit all our data with Eq. 5.1. As the temporal resolution of our data is too low to find the instantaneous relaxation rate using a numerical derivative, we will characterize the relaxation curves by  $R_1$ ; the angle that the disk rotates back during the first 28 s.

In Fig. 5.9(a-b) we show experiments for  $\Gamma = 0.7$ , where the black data corresponds to  $\Omega_1 = 10^{-2}$  rps and  $\Omega_2 = 10^{-4}$  rps, and the red data to the opposite, *i.e.*  $\Omega_1 = 10^{-4}$  rps and  $\Omega_2 = 10^{-2}$  rps (in Fig. 5.9, all the left panels correspond to stage 1, and the right panels to stage 2). In Fig. 5.9(a) the black data shows that for  $\Omega_1 = 10^{-2}$  rps, the anisotropy monotonically reaches a plateau value of  $R_1 \approx 8$  mrad. If we then change to the second stage with  $\Omega_2 = 10^{-4}$  rps (panel (b), black), we see that the relaxation monotonically drops to a steady state value of  $R_1 \approx 4$  mrad. This trend is consistent with the prior results: for lower  $\Omega$ , the vibrations are relatively more important, which leads to a less anisotropic packing.

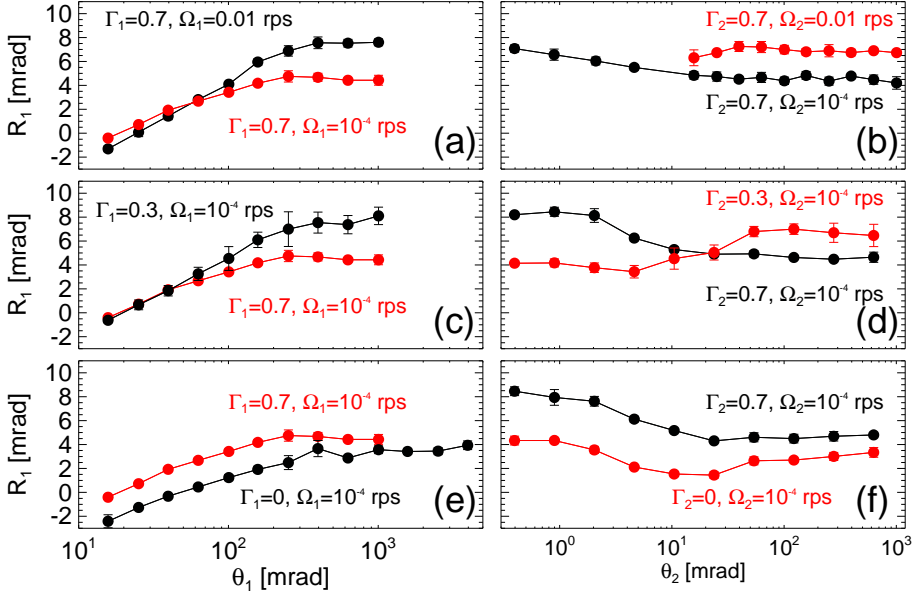


FIGURE 5.9: The relaxation  $R_1$  for experiments using the extended protocol as shown in Fig. 5.8. By interchanging the  $\Gamma$  or  $\Omega$  that is imposed during stage 1 and stage 2, we can investigate the uniqueness of the steady state values of the anisotropy.

In red, we show the inverse experiment. In Fig. 5.9(a) we find that the red data ( $\Omega_1 = 10^{-4}$  rps) equilibrates at  $R_1 \approx 4$  mrad, and for  $\Omega_2 = 10^{-2}$  rps, the red data in Fig. 5.9(b) evolves to  $R_1 \approx 8$  mrad. Hence, for these parameters, the asymptotic value of  $R_1$  only depends on its current stage and not on the previous stage; irrespective of the system's history, at  $\Gamma = 0.7$ , an  $\Omega$  of  $10^{-4}$  rps corresponds to a  $R_1$  of 4 mrad, and  $\Omega = 0.01$  to  $R_1 \approx 8$  mrad. We finally note that (with the exceptions for small  $\theta_1$ ), all the relaxations are logarithmic, and the anisotropy changes monotonically.

In (c-d) we keep  $\Omega$  constant at  $10^{-4}$  rps, but change  $\Gamma$  between 0.3 and 0.7. Also here the steady state is history-independent and unique, and the anisotropy evolves monotonically.

In Fig. 5.9(e-f) we illustrate qualitatively different curves that govern the evolution between  $\Gamma = 0.7$  and  $\Gamma = 0$ . Several saillant features stand out. First: for  $\Gamma_1 = 0$ , the transient seems longer than in previous data, but after a strain  $\theta_1 \approx 500$  mrad, the system reaches a steady state  $R_1 =$

4 mrad. Second: the steady state  $R_1$  is the same for  $\Gamma_1 = 0.7$  and  $\Gamma_1 = 0$  – this is consistent with the observation in Fig. 5.6(a) that at intermediate flow rates, the anisotropy is non-monotonic in  $\Gamma$ . Third: comparing the steady state values in (e) and (f), we find that they are consistent: also here, the steady state value of  $R_1$  is unique. Fourth: the behavior of the black curve in (f) is surprising: if we switch on the vibrations, the relaxation almost instantly *increases* from  $R_1 \approx 4$  mrad to  $R_1 \approx 8$  mrad. A possible explanation for this is that the vibrations compact the packing, and that a denser packing leads to a higher anisotropy. With increasing  $\theta_2$ , the packing adapts to its steady state  $R_1 \approx 4$  mrad. Fifth: as shown by the red curve in (f), the evolution from  $R_1 \approx 4$  mrad (which is the steady state for  $\Gamma = 0.7$ ) to the similar relaxation value  $R_1 \approx 4$  mrad for  $\Gamma = 0$ , is strongly non-monotonic:  $R_1$  does not remain constant at 4 mrad, but dips to 1 mrad (while  $T$  peaks to a maximum) before growing back to 4 mrad. This means that for small strains, the flow first *removes* anisotropy from the packing. This suggests that even though  $\Gamma = 0.7$  and  $\Gamma = 0$  correspond to the same amount of relaxation, the way the anisotropy is built into the packing is different between these two cases.

The examples in (e-f) suggest that  $\Gamma = 0$  is a special case. Even though the steady state values of the anisotropy are unique, the evolutions show surprising non-monotonic behavior, indicating that there are different ways for the packing to be anisotropic.

We proceed by looking at the raw relaxation curves to see how they change as the system evolves towards a new steady state. In Fig. 5.10 we show the curves that correspond to the red data in Fig. 5.9(f) for  $\theta_2 = 0.40, 24, 628$  mrad – as indicated in the legend. The black and red curves correspond to similar  $R_1$ , however, the black curves (as emphasized by the normalized curves in (b)) are slightly more curved. This is consistent with Fig. 5.5(a) where we found scatter in the relation between the initial slope and the curvature of the relaxation curve.

The blue curves in Fig. 5.10(a) correspond to the dip in Fig. 5.9(f). For these curves, the relaxation is significantly slower than for the red and the black data. This demonstrates that even though it is impossible to grasp all the precise characteristics of the curve with a single parameter, the dip in Fig. 5.9(f) is a robust effect which would also have been easily picked up by the original parameter  $R$ .



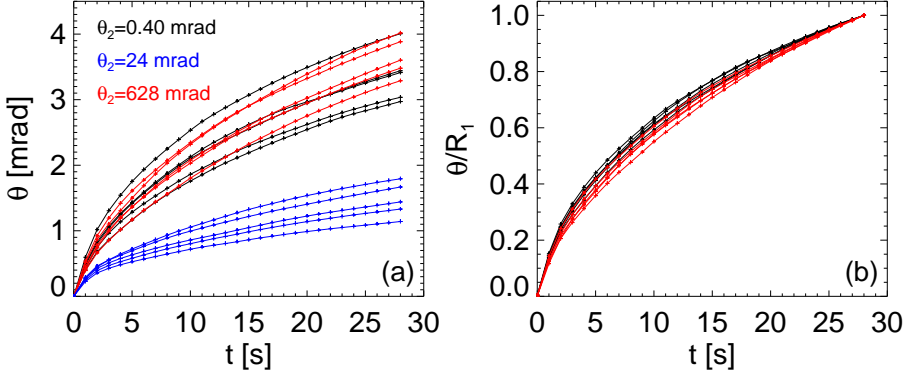


FIGURE 5.10: (a) The relaxation curves for the red data points in Fig. 5.9(f) with  $\theta_2$  [mrad] = 0.40, 24, 628. The black and the red curves correspond to similar  $R_1$ , however, the black data is slightly more curved. The relaxation in the blue data is significantly slower. (b) The red and black data as in (a), normalized by  $R_1$ , confirm that the black data is more curved.

During the evolution between stage 1 and 2, the relaxation curves appear to be logarithmic – just as for steady states. As a check, we calculate  $\chi^2$  for the fits and compare the values to the ones found for the steady state relaxation in Fig. 5.5(b). We find that the values are consistent, suggesting that the shape of the relaxation curves during the evolution is the same as the shape for steady state relaxations.

Finally, we want to verify the *robustness* of the deviating behavior for  $\Gamma = 0$  that was observed in Fig. 5.9(e-f). Therefore, we perform more experiments, with different  $\Omega_1$ ,  $\Gamma_1$ ,  $\Omega_2$ , and  $\Gamma_2$  (either  $\Gamma_1$  or  $\Gamma_2$  is 0), and show the results in Fig. 5.11. As we are only interested in the surprising behavior during stage 2, we take a constant  $\theta_1$  of 600 mrad (long enough to reach a steady state), and probe only the relaxation during the second stage.

The blue and the green curve in Fig. 5.11 represent the case where  $\Gamma_1 = 0$  and  $\Omega_1 = 10^{-4}$  rps. As we know from Fig. 5.9, the corresponding  $R_1 = 4$  mrad. The behavior for these cases is the same as for the black curve in Fig. 5.9(f); as soon as the vibrations are switched on, the anisotropy suddenly increases significantly. The fact that the increase is of different

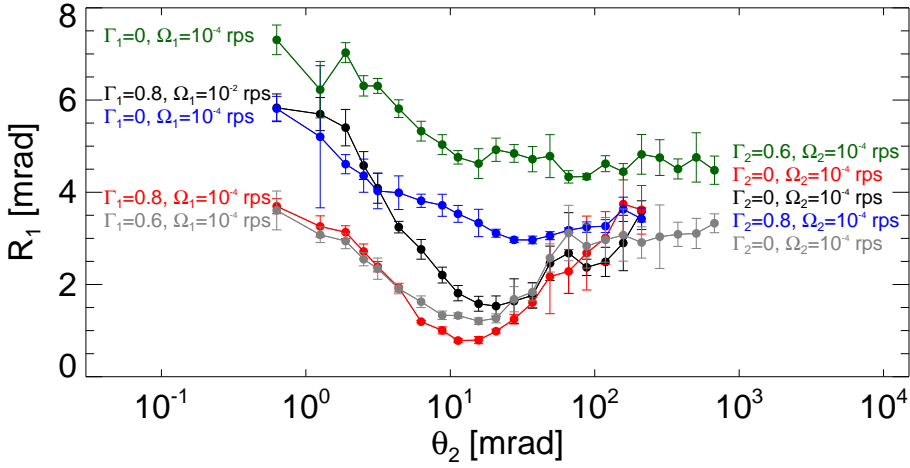


FIGURE 5.11: Additional experiments to investigate the deviating results when either  $\Gamma_1$  or  $\Gamma_2$  is 0. In this case, we only probe the relaxation during stage 2.

size between the green (which goes to  $\Gamma_2 = 0.6$ ) and the blue curve ( $\Gamma_2 = 0.8$ ), shows that the increase is  $\Gamma$ -dependent.

The red and the gray curve are for the case where  $\Gamma_2 = 0$ . Again, we see the characteristic significant dip in  $R_1$ , similar to the dip in the red curve in Fig. 5.9(f).

For the black curve we change both  $\Gamma$  and  $\Omega$ . We start from a very anisotropic packing that we reached with relatively fast flow:  $\Gamma_1 = 0.8$  and  $\Omega_1 = 0.01$  rps. We then switch to slow flow ( $10^{-4}$  rps) at  $\Gamma_2 = 0$ , and again see a strongly non-monotonic  $R_1(\theta_2)$ .

Hence, all the curves in Fig. 5.11 are consistent with the behavior that was observed in Fig. 5.9.

## 5.5 Conclusion and Discussion

In this chapter we have investigated the anisotropy of packings by probing how the anisotropy relaxes from the packing as it is weakly vibrated. In Fig. 5.6(b) we found that the strength of the relaxation is set by the torque that was imposed during the flow. This observation suggests that the an-

isotropy is a crucial ingredient towards finding a constitutive relation for granular flows.

In Fig. 5.9 we found that for each  $\Gamma$ ,  $\Omega$ , there is a unique value of the anisotropy – independent of the history of the system. The relaxation curves, both for a steady state and an evolving packing, can be fitted using a two-parameter logarithmic function. There is a robust trend that this fit matches the data slightly better for faster relaxations.

From our measurements it is hard to precisely quantify the anisotropy at a certain point in time. First, the non-monotonic evolution of the anisotropy in time in Fig. 5.9 and Fig. 5.11 shows that the relaxation is a complex quantity, which seems to depend not only on anisotropy, but also on density. We expect these two effects to be coupled [129], so it requires great care to separate the influences of the two and to assign a value to the anisotropy. A second difficulty is the complex flow profile in the split-bottom geometry. We find that, because of the large range of strain rates that are present in the system, different parts of the system can correspond to a different value of the anisotropy. The relaxation that we measure is a collective result of the relaxation of all the different regions. In Fig. 5.9(a,c,e) it seems that the building of anisotropy from the presheared state is logarithmic in time. However, because of spatial inhomogeneities, we cannot claim that this dependence is true for all, especially more simple, flow geometries. In fact, in simulations it is found that anisotropy grows exponentially in time [130]. Another consequence of the complex shape of the relaxation curves is that they cannot precisely be characterized using a single parameter. However, the relaxation curves are similar in size enough to allow us to obtain robust results, independent of the precise order parameter.

In general, we expected flow to *build* anisotropy and vibrations to *relax* it. In Fig. 5.6(a) this was confirmed for finite  $\Gamma$  and small  $\Omega$ , which corresponds to a significantly slower relaxation. For intermediate flow rates,  $\Omega \approx 0.01$  rps, the relaxation is non-monotonic in  $\Gamma$  – also suggesting that the relaxation that we measure is the result of at least two different physical properties of the system. This physical picture is backed up by the data in Fig. 5.9 and Fig. 5.11. In these results we found the additional evidence that equal relaxation does not imply that the precise anisotropic state of the packing is also the same. Even though the steady state values of the relaxation are unique and independent of the system's history,

we observed surprising behavior during the (non-monotonic) evolutions, where in some cases vibrations *increase* the relaxation and flow *decreases* it. All the deviating transients involve  $\Gamma = 0$ , either as initial or destination state. This shows once more that the granular flow in a system with “zero temperature” differs significantly from the case with weak vibrations.

### 5.5.1 Outlook

For future experiments, we suggest two modifications to the protocol that was introduced in Fig. 5.3.

First, the way we switch off the shaker during the freezing stage can be improved. For the experiments reported in this chapter, we stopped the shaking abruptly – at an arbitrary phase of the oscillation. However, this can result in a fast relaxation of the shaker to its equilibrium position, which might affect the packing. We have performed exploratory measurements where we smoothly damp out the vibrations using a Doepfer A-143-2 voltage controlled amplifier that gradually decreases the wave amplitude to 0 over a period of ten oscillations. We found that the main results reported in this chapter, including the torque collapse in Fig. 5.6(b), are unaffected by this modification of the protocol.

Second, we would modify the way the flexure is relaxed during the freezing stage. In the reported experiments, we abruptly switch to  $T = 0$ , which we do not expect to alter the frozen packing. However, at  $\Gamma = 0$ , the flexure is stretched with a torque of the order of the yield torque, and we cannot be certain that the impact, that the packings endures when we switch to  $T = 0$ , does not affect the packing. In fact, this impact could explain the surprisingly low values of  $R$  for  $\Gamma = 0$  in Fig. 5.6. To improve the protocol, the torque can be reduced to zero smoothly. We stress that the main result of this chapter, the torque collapse in Fig. 5.6(b), is not sensitive to the way the torque is reduced, as the collapse occurs for low torque experiments, where the torque in the spring is significantly below the yielding torque of the frozen packing.

# GIANT HEAPING IN SHEARED ANISOTROPIC GRANULAR MEDIA

---

## 6.1 Introduction

Most work on granular media focusses on simplified circular (2D) or spherical (3D) particles. However, the particles in granular media encountered in industry and nature usually have more complex, anisotropic shapes. Gaining insight into the behavior of anisotropic particles is therefore practically relevant, but it also enlarges the theoretical understanding of granular materials in general, and leads to novel questions, for example regarding ordering. In this chapter, we describe experiments where we shear granular rods in the split-bottom geometry.

Recently, the interest in granular rods has increased, with most experiments focusing on the role of *vibrations*. Experiments in 3D on rods in a vibrated tube show that the rods align to the walls and form a high density nematic phase [131–134]. Others performed quasi-2D experiments where similar alignment was found [135]. For low packing fractions, large local density fluctuations are found due to a competition between alignment and void formation [136]. Some studies are performed on the *flow* of rod systems. Here, the emphasis is on the time evolution of the alignment of the particles in the shear band [123, 124, 137–139]. A recent review summarizes the work on granular rod systems [140].

In our flow experiments, we observe strong alignment of the particles in the shear band. In addition, we observe the formation of a heap that arises from the center of the system. In Fig. 6.1 we show two photos of the system – one before, and one after the formation of the heap. The peak of the heap can reach heights of up to 50% of the filling height, which makes these surface undulations a very significant effect. The goal of this



FIGURE 6.1: (top) The initial flat surface. (bottom) A vermicelli heap that has grown while we sheared the system.

chapter is to characterize the heaping process and to unravel the physical mechanism responsible for it.

It is well-known that a densely packed granular material *dilates* under shear [18]. It then reaches the so-called critical state with a steady state void ratio or packing fraction, independent of the initial packing [125]. In geology, it is known from experiments that materials consisting of elongated particles also expand under shear [121]; a result that is confirmed in simulations [141]. In both of these cases it is found that shear creates large voids in the packing, which results in a low packing fraction. A competing mechanism in sheared rod systems is that the shear can cause *alignment* of the particles. This alignment can result in an *increased* packing fraction, as observed in rice avalanches [142] and 2D simulations [143]. In general, both dilation and compaction are present in a sheared granular rod system. It then depends on, *e.g.*, the shape of the particles and the flow geometry which of the two dominates. Recent experiments have shown that in a split-bottom Couette geometry, for shallow filling heights, the dilation dominates, even in the shear band where the particles are strongly aligned [139].

We note that there is a vast literature on sheared thermal rods. Kinetic theory predicts that rods can only align in situations of weak local diffusion [144]. In polymer simulations [145] and attractive colloid exper-

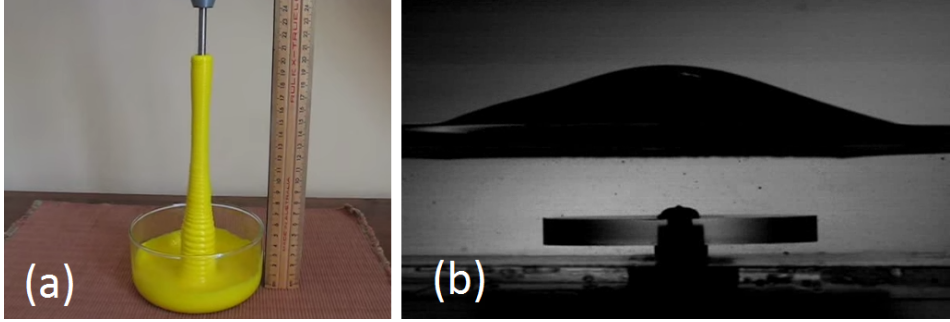


FIGURE 6.2: (a) Traditional rod climbing experiment using a mixture of polyvinyl acetate and sodium tetraborate [147]. (b) Rodless Weissenberg effect using a HASE polymer [148].

iments [146], it is found that the tendency of rods to move out of the shear plane strongly depends on the local  $\dot{\gamma}$ .

The heaping is reminiscent of the so-called *Weissenberg* effect – see Fig. 6.2. This effect occurs when a spinning rod is inserted into a polymer solution, which as a result will climb up the rod [149]. A similar surface deformation has also been observed with a viscoelastic fluid in the split-bottom geometry [148]. In both cases, the surface deformation is driven by a net centripetal force, which originates from normal force differences in the system. As a consequence, the height of the fluid bump depends on the rotation rate of the rod and goes to zero for slow flows. We note that, whereas similar heaping is found [151–153] for very fast granular flows, our measurements are in the rate-independent regime. We therefore can rule out rate-dependent effects as the cause for heaping.

Experiments on the flow of spherical particles in the split-bottom geometry have shown the presence of *convection rolls* [82, 150, 154, 155] – see Fig 6.3. Similar convection is observed for vibrated sys-

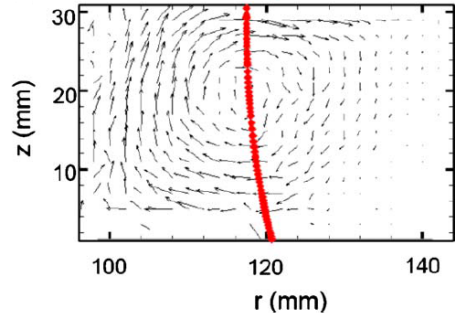


FIGURE 6.3: A vertical slice through the split-bottom cell [150]. The velocity vectors indicate the convection; the red line depicts the shear band.

tems [156, 157]. The flow driven convection, which can create either an upwards or a downwards motion in the core, is very slow with respect to the main flow, and much slower compared to our heaping. Nevertheless, as we shall see in this chapter, our heaping process is caused by convection. The essential difference is that the convection is much stronger in a system consisting of elongated particles compared to spherical particles. We believe this to be caused by the misalignment between the particle orientations and streamlines of the flow.

The outline of this chapter is as follows: In Sec. 6.2, we will introduce the setup and explain how the raw data is processed. In Sec. 6.3, we characterize the heaping phenomenon by carefully describing what we observe in the experiments. To unravel how the heaps are formed, we perform experiments with a more complex measuring protocol in Sec. 6.4. To see the motion of the particles below the surface, we performed experiments in an X-ray CT scanner in collaboration with the groups of T. Börzsönyi and R. Stannarius; the results are shown in Sec. 6.5. We end with an outlook where we suggest other interesting experiments concerning anisotropic particles in App. 6.A.1.

## 6.2 Setup and Methods

### 6.2.1 Setup

**Split-Bottom Cell** – The experiments are carried out in a split-bottom cell (see Fig. 6.4(a)) with an outer radius of 110 mm, an inner radius  $R_s$  of 85 mm and a height of the container of 120 mm. The inner bottom disk is connect to a SWF 403.559 24 V DC motor, which we use to shear the system. The rate of the motor is controlled by an external duty-cycle controlled, pulsed DC source. The rotating disk is visible from below the system, which enables us to measure its rotation rate, which - for constant settings of the pulse-controlled source - does not significantly depend on the amount of grains in the system. Rice grains are glued to the entire inside of the cell to ensure no-slip boundary conditions.

As we shall see later in this chapter, it was crucial for the discovery of the heaping process that the experiments are performed in the split-bottom geometry. In a Couette geometry, the shear is very localized and



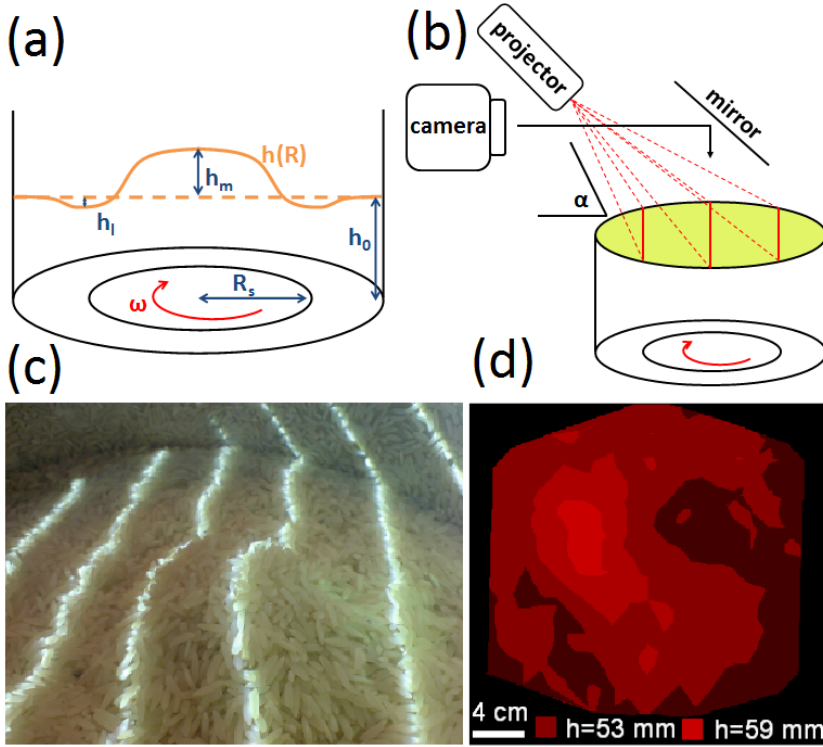


FIGURE 6.4: (a) A schematic of the setup with initial surface (dashed) and steady state heap (solid). The parameters (that are explained in the text) are indicated. (b) A schematic image of the imaging part of the setup. (c) Close up of the heap and the deformed line pattern. (d) The reconstructed surface  $\hat{h}$ .

there is no significant heaping. This nicely illustrates, once more, how rich the flow behavior of the split-bottom geometry is.

To image the surface we use a Foculus FO432B camera which is mounted horizontally – see Fig. 6.4(b). We obtain images of the surface of the material right from above using a mirror. To see surface deformations, we project straight lines on the surface using an Epson EB-824 projector. For details, see Sec. 6.2.2.

**Particles** – Most of the measurements are carried out with long grain “Surinam Rice” particles. The grains have a long axis of approximately



FIGURE 6.5: A picture of the particles that are used for most of the experiment: long grain “Surinam Rice” (left) and vermicelli (right).

$7 \pm 1$  mm and fairly constant short axes of 2.0 and 1.5 mm – resulting in an aspect ratio  $Q \approx 4$ . Furthermore, measurements are performed using “vermicelli” grains with a very constant diameter of 1 mm and length of  $14 \pm 3$  mm, corresponding to an aspect ratio of about  $Q \approx 14$ . Most of the vermicelli grains are slightly curved. A sample of these particles is shown in Fig. 6.5.

### 6.2.2 Methods

In this section we discuss how we measure and reconstruct the particle surface. In addition, we explain how we use the reconstruction to quantify the shape of the heap.

**Protocol** – Before each run we stir the system by hand to reach a disordered initial state. We proceed by flattening the surface by gently pushing on the system using a circular piece of cardboard. We then start the motor (with a rotation rate of 0.066 rps) and the imaging system, and observe the heap formation.

**Surface Reconstruction** – To reconstruct the shape of the surface, a series of lines is projected onto the surface using the projector, which is

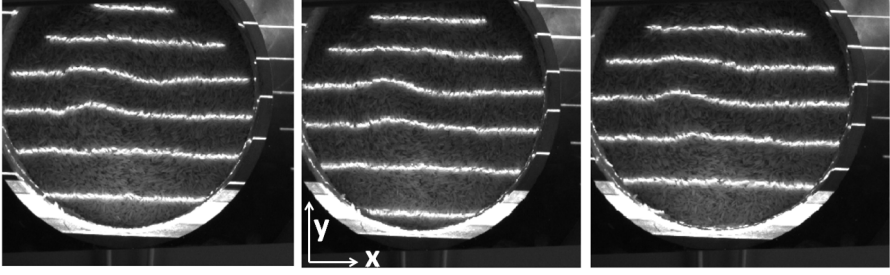


FIGURE 6.6: An example of how we project three series of five or six lines. This method enables us to reach a high spatial resolution without running into tracking limitations.

aimed at the surface under an angle  $\alpha$  of  $51^\circ$  (for the middle line) – see Fig. 6.4(b-c). The mean distance between the projector and the surface is about 75 cm. The height profile of the surface is recovered from these lines, which, when seen from above, are deformed when the surface shape changes. We take pictures from the top and use these to track the lines using an in-house built IDL-code. To increase the spatial resolution without running into tracking limitations, we project three series of lines (within 0.3 s) consecutively, where the locations of the lines are shifted with respect to each other. The projection of the lines in three series limits our rotation rate to rates below 0.1 Hz; this is not problematic as we have verified to be in a rate-independent regime, so we can perform the experiments at low rotation rate.

An example of three series of lines can be seen in Fig. 6.6. The spacing between the lines in consecutive frames, and thus the horizontal spatial resolution  $dy$ , is 10 mm. In the  $x$  direction, parallel to the projected lines, for symmetry reasons, we also pick  $dx = 10$  mm.

The amount of shear that has been imposed to the system is proportional to the total rotation angle of the bottom disk  $\theta$ . Because of core precession [77], this can differ from the rotation observed at the free surface. We chose to use the angle of the bottom disk because it is easier to measure than the rotation of the surface (which requires PIV) and because it is kept constant for all the runs. As we shall see in the next section, we have performed experiments where the rotational direction was changed during the run. To plot this without the curve overlapping, we will plot

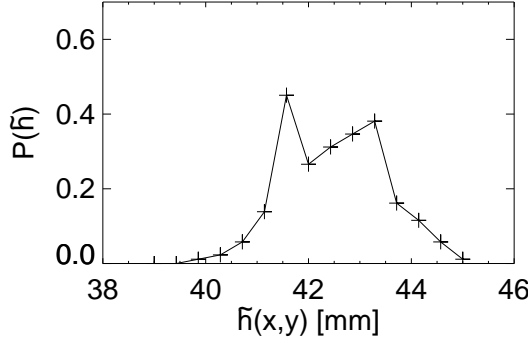


FIGURE 6.7: An example of a pdf of  $\tilde{h}(x, y)$  for a flattened surface for  $Q = 4$  rice particles.

them as a function of  $|\omega|t$ , where  $\omega$  is the rotation rate of the inner bottom disk.

We obtain the local surface height as a function of deflection angle ( $\theta$ ),  $\tilde{h}(x, y, \theta)$ . For a clear distinction between heaps and depressions we define  $h(x, y, \theta) = \tilde{h}(x, y, \theta) - h_0$ , where  $h_0$  is the filling height, which is defined as  $\langle \tilde{h}(x, y, \theta = 0) \rangle$ . In Fig. 6.4(d) we show a color plot that represents the reconstructed surface ( $\tilde{h}$ ).

To investigate the accuracy of surface reconstruction, we prepare the system, as described above, using  $Q = 4$  rice particles up to a filling height of 42 mm. We perform the surface reconstruction and plot a pdf of  $\tilde{h}(x, y)$  in Fig. 6.7. It can be seen that the spread in  $h$  is of the order of 2 mm. We believe that this spread is mostly caused by the rough, grainy surface. From  $\tilde{h}(x, y)$ , we obtain the actual average filling height  $h_0 = 42.7$  mm.

To analyze the orientation of the particles we have an additional fourth stage in our imaging where we just project light on the surface. From these images we can find the local orientation of the grains using PIV analysis.

**Interpretation** – One key parameter to describe the heaps is their height. Since the maximum value of  $h$  is noisy, we define the heap height  $h_m$  as the average of the five maximum points of  $h$ . Similarly, we define the lowest depression of the surface  $h_l$  as the mean over the five lowest points of  $h$ . Finally, we look at the average height  $\langle h \rangle$ . As we shall see in the next

section, the global heap formation process is robust to such an extent that the single parameter  $h_m$  is well capable of characterizing the heap.

The parameters that we use to describe the surface undulation are summarized in Fig. 6.4(a).

## 6.3 Phenomenology

Before studying the heap formation in detail we want to globally characterize the growth process.

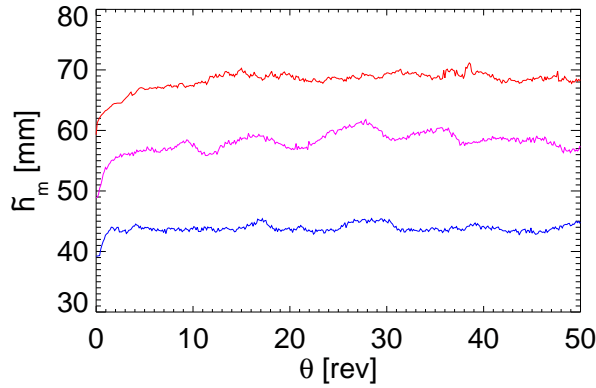


FIGURE 6.8: Evolution of  $\tilde{h}_m$  for three different filling heights. It can be seen that for a certain  $\theta$ ,  $\tilde{h}_m$  reaches a steady state value  $\tilde{h}_M$ . The time it takes to reach the steady value decreases with  $h_0$ . This data is for  $Q = 4$  rice particles.

### 6.3.1 Growth Evolution

**Heap Height  $h_m(\theta)$**  – In Fig. 6.8 we plot  $h_m(\theta)$  for three different filling heights. It can be seen that  $h_m$  reaches a maximum value  $h_M$  after typically a few rotations. Our data suggests that the process quickly reaches a steady state, in contrast to slow (logarithmic) processes as in the compaction of granular material under vibration [126]. The data also illustrates that the equilibration time increases with  $h_0/R_s$ . This can be under-

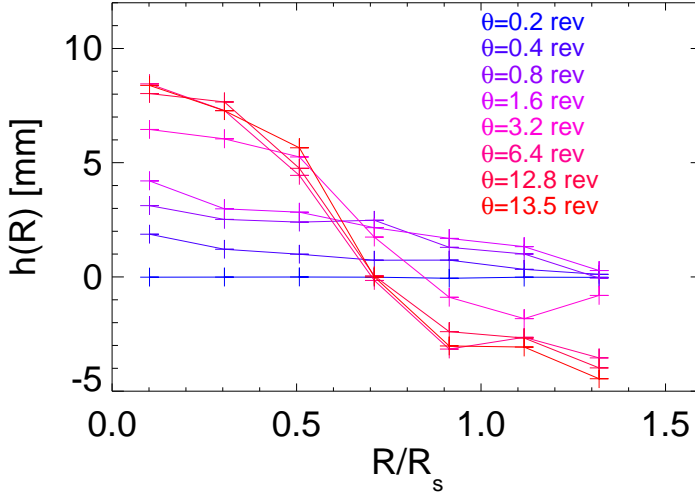


FIGURE 6.9: The surface shape  $h(R)$  for  $h_0/R_s = 0.46$  and  $Q = 14$  vermicelli particles.

stood by realizing that, for large  $h_0/R_s$ , the average strain rate and thus the heap formation is slower.

From visual observations of the heap, we see that, even when the steady state height has been reached, particles avalanche down the slopes of the heap. This suggests that the steady state is a dynamical one, where avalanches that decrease  $h_m$  and other processes that increase  $h_m$  precisely balance.

**Heap Profile  $h(R, \theta)$**  – Because of the cylindrical symmetry of the geometry, we transform  $h(x, y, \theta)$  to polar coordinates to get  $h(R, \phi, \theta)$ . In the case of a rotationally symmetric surface, this can be averaged over  $\phi$  to get  $h(R, \theta)$ . This provides a simple alternative way to visualize the development of the heaping process.

We show a typical example of its evolution for  $Q = 14$  particles in Fig. 6.9. We see that in the center of the system (small  $R$ ), the heap grows monotonically. In the shear band, at  $R/R_s \approx 1$ , the height evolution is not monotonic. It seems that the particles first have to align, which requires dilation, but once aligned, the surface drops to a height even below the

original level at  $\theta = 0$  [158]. Starting from the curve for  $\theta = 6.4$  rev,  $h(R)$  maintains its shape, indicating that the system has reached a steady state.

From  $h(R)$  we cannot only see whether the system dilates or compacts for certain  $R$ , but we can also calculate the total volume of the granular medium by evaluating the integral  $2\pi \int \tilde{h}(R) R dR$ . As a consistency check, we calculate the volume (for an unsheared packing), and using the total mass of the particles, we find an initial density of approximately 670 g/l. Comparing this to the particle density that we measure to be  $1.2 \times 10^3$  g/l, we find a packing fraction of 58% – very similar to the ones reported in literature [131, 138].

### 6.3.2 Aspect Ratio, Shape and Material

We performed exploratory experiments with many different kinds of particles with varying aspect ratio  $Q$  and shape. The heaping occurs very robustly for elongated particles with high enough  $Q > 3$  – regardless of their exact shape and material. We have done tests and observed heaping for rice grains, slightly bent vermicelli grains (see Fig. 6.5), and perfect PMMA cylinders and metal spherocylinders, both measuring  $3 \times 3 \times 12$  mm<sup>3</sup> ( $Q = 4$ ). For short grain rice ( $Q = 2$ ), we did not observe any heaping.

### 6.3.3 Heap Location

A qualitative difference between the behavior of rice ( $Q = 4$ ) and vermicelli ( $Q = 14$ ) is the precise location of the heap. For  $Q = 14$ , it is exactly in the center of the system, which results in a symmetric  $h(R, \phi)$  that can be averaged over  $\phi$ . For  $Q = 4$ , the center of the heap is often a few cm off-center (see Fig. 6.4(d)). The heap *does* reach a steady height (Fig. 6.8), but the center of its location corotates with the system. This observation could help in finding the explanation for the heap formation, but it is also a reason, especially when studying  $h(R)$ , to perform experiments with high aspect ratio particles.

### 6.3.4 Filling Height Dependence

We study how the heaping effect varies with the filling height  $h_0/R_s$ . In the split-bottom geometry, the flow profile changes with  $h_0/R_s$  [76]. Therefore, it is interesting to study its influence on the heaping.

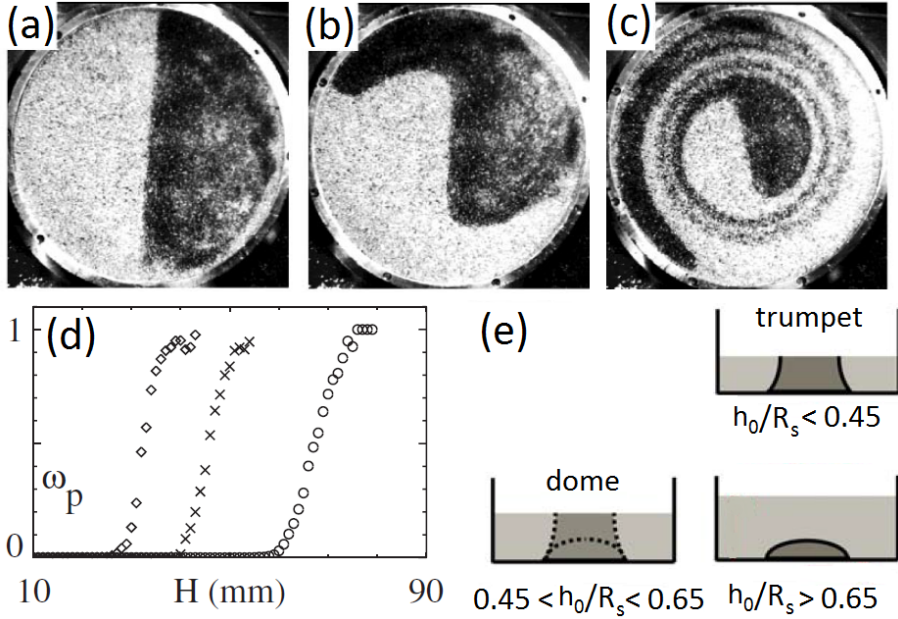


FIGURE 6.10: (a-c) Series of snapshots of top views of the setup, where colored particles sprinkled on the surface illustrate the core precession [77]. (d) Precession rate  $\omega_p$  as a function of vertical coordinate  $H$  for  $R_s = 45$  mm ( $\diamond$ ),  $R_s = 65$  mm ( $\times$ ) and  $R_s = 95$  mm ( $\circ$ ) [77]. (e) The transition in flow structure from shallow to deep flows in the cylindrical split-bottom geometry. In the dark gray region the material comoves with the disk. [76].

Before looking at the heaping data, we summarize the filling height dependence of split-bottom flows in Fig. 6.10. In (e), we show how the flowing region varies with  $h_0$ . For shallow filling heights, all the grains in the center of the system comove with the inner bottom disk. For high  $h_0$ , there is a velocity gradient in the vertical direction (precession), and particles at the surface have a significantly lower flow rate than the disk. The precession is visualized in (a-c) using colored particles at the surface. Here, the system is driven via the outer wall, and the spiral pattern is a reflection of the angular velocity difference, which increases with  $R$ , between bottom disk and surface particles. In (d), we plot the precession rate  $\omega_p = 1 - \frac{\omega_s(R \rightarrow 0)}{\omega}$ , where  $\omega_s(R \rightarrow 0)$  is the limit of the rotation rate towards center of the top surface [77], as a function of the vertical coor-



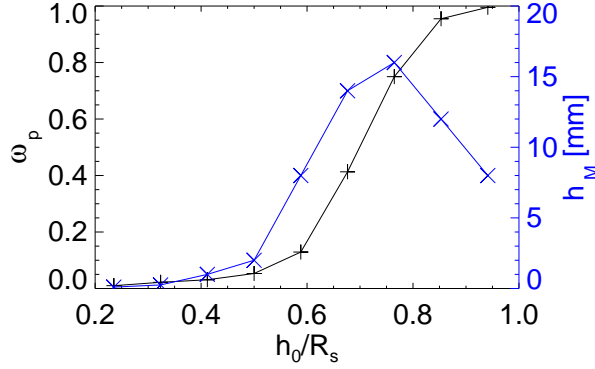


FIGURE 6.11: Filling height dependence of  $h_M$  and the core precession  $\omega_p$  for  $Q = 14$  particles.

dinate  $H$ . We see that at the bottom, the particles comove with the disk, whereas with increasing  $H$ , the precession also increases.

Going back to the heap data, the first question is for which  $h_0/R_s$  the effect is the most prominent. In the blue curve in Fig. 6.11, we show the heap height  $h_M$  of the heap as a function of  $h_0/R_s$  and see that the effect is strongest for  $h_0/R_s \approx 0.75$ . To compare the heaping with the flow profile, we compare  $h_M$  to the precession rate  $\omega_p$  (plotted in black). We note that we believe the  $h_0/R_s$ -dependence to vary with  $Q$ .

When we systematically study the filling height, we find the following regimes:

**$h_0/R_s < 0.5$**  – For low  $h_0/R_s$  (trumpet flow), there is no heap formation. The grains on top of the bottom disk just corotate with it ( $\omega_p = 0$ ) and nothing happens in this rigid core. For  $h_0/R_s$  close to 0.5, we see a small ridge on the outside of the center, next to the shear band (Fig. 6.12(b)).

**$0.5 < h_0/R_s < 0.9$**  – For this range in  $h_0/R_s$  (dome flow), the shear band starts to close and the grains at the surface rotate slower than the bottom, which results in  $\omega_p > 0$ . We observe high heaps where the highest point (for  $Q = 14$ ) is at the center of the core (Fig. 6.12(a)).

**$h_0/R_s > 0.9$**  – For  $h_0/R_s > 0.9$ , the flow at the surface becomes increasingly smaller,  $\omega_p$  goes to 1 and  $h_M$  decreases. The system does dilate,

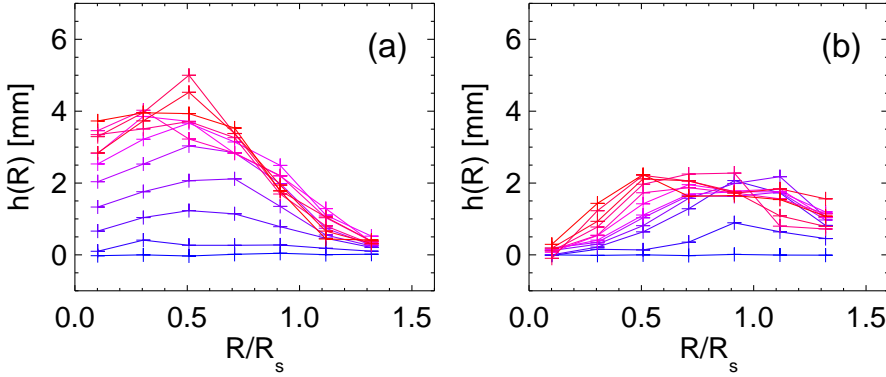


FIGURE 6.12: (a) The surface shape  $h(R/R_s)$  for  $h_0/R_s = 0.57$  and  $Q = 4$  rice particles. The 12 curves from blue to red correspond to  $\theta$  [rev]=0.2, 0.3, 0.5, 0.8, 1.2, 2, 5, 10, 20, 40, 70, 100. (b) The surface shapes for  $h_0/R_s = 0.46$ .

which suggests that the dilation in the core also occurs for high filling heights. However, the dilation is averaged out in space so it manifests itself as a homogenous dilation instead of as a heap.

Hence, we find that  $\omega_p$  and  $h_M$  are connected; for filling heights where there hardly is precession, there is also no significant heaping. This suggests that the heaping could be driven by the gradients in angular velocity.

## 6.4 The Mechanism behind the Heaping

To understand the mechanism behind the heap formation, we perform experiments with a more complex experimental protocol. First, we do experiments where we pause the shear, remove the heap, restart the shear, and see that the heap regrows. Second, we will reverse the direction of the flow, which first, surprisingly, makes the heap disappear and then regrow. Finally, using colored particles, we visualize the secondary convective flow.

### 6.4.1 Heap Removal

We want to know if the driving mechanism for the heaping occurs continuously, or if it is a transient effect that only works until a steady state

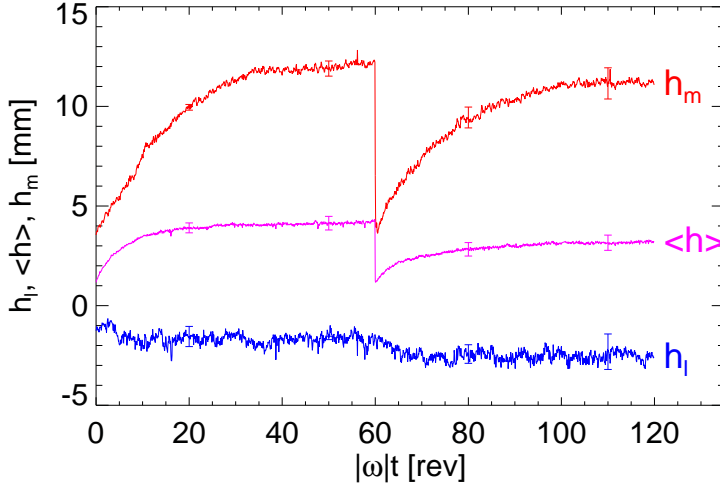


FIGURE 6.13: In this experiment we first grow a steady state heap by shearing the system for 60 rev. The heap height  $h_m$  is plotted in red, purple is the average height  $\langle h \rangle$  (we see that the system dilates), and blue is the lowest point  $h_l$ . After 60 rev we stop the system, remove the heap with a vacuum cleaner, and then restart the flow. We see that the heap grows back. These curves are the average over 10 runs (see error bars) and are for  $Q = 4$  particles.

density has been reached in the core. To find out, we perform experiments where we shear the system for 60 rev at 1/15 rps – which is long enough to reach a steady state. We then stop the motor and remove the heap using a vacuum cleaner. After this we restart the motor (in the same direction) and observe what happens. We perform the experiment ten times and average the data for  $h_m$ ,  $\langle h \rangle$  and  $h_l$ . The result is shown in Fig. 6.13, with error bars that indicate the standard deviation over the ten runs. It can be seen that a steady heap height is reached well before  $\theta = 60$  rev. After we have removed the heap, it grows back at a rate similar to the speed of the first heap formation. The heap reaches a slightly lower height than the first time, which is simply caused by the fact that there are now less particles in the system. From  $\langle h \rangle$ , we see that the system dilates. This is in accordance with the findings of Wegner *et al.* [139], who reported dilatancy for particles with  $2 < Q < 5$  in split-bottom Couette flow.

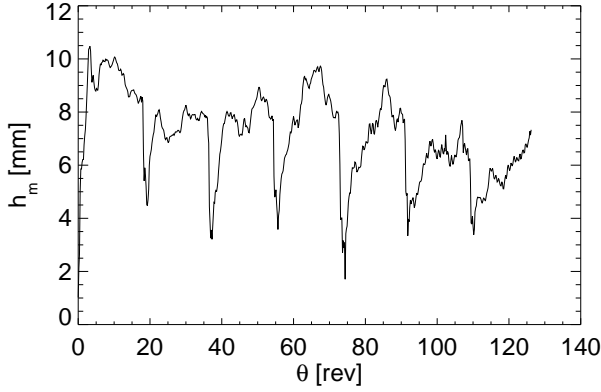


FIGURE 6.14: Evolution of  $h_m$  for an experiment where we repeat the heap growth and removal seven times. Every time we remove the heap, it grows back (until a filling height is reached where we never see heap formation). We can therefore conclude that the heap formation process is not a transient effect. This data is for  $Q = 14$  particles.

We have performed an exploratory measurement, where we repeat the heap removal multiple times in a single experiment. The evolution of  $h_m$  is plotted in Fig. 6.14. After each time we remove the heap, it grows back – until a filling height is reached where no heap formation occurs. Note that the data in Fig. 6.14 is more noisy than the data in Fig. 6.13 because the latter is the average over 10 runs, while the former is only a single run.

The observation that the heap regrows after removal strongly indicates that the heaping process is continuous and not a transient dilation effect.

### 6.4.2 Reversal

To learn something about the structure of the packing, we perform experiments where we reverse the direction of the flow. We first shear for 53 rev at 1/15 rps to reach a steady state heap, and then reverse flow direction. From the results that are plotted in Fig. 6.15(a) (averaged over ten runs), it can be seen that the heap collapses very fast when the flow is reversed. After the collapse, the heap has completely disappeared and the center of system even shows a small dip compared to the shear band (Fig. 6.15(b)). When we keep shearing after the collapse we see that the heap grows back, at a speed similar to the initial growth rate. After 53 more revolutions, we

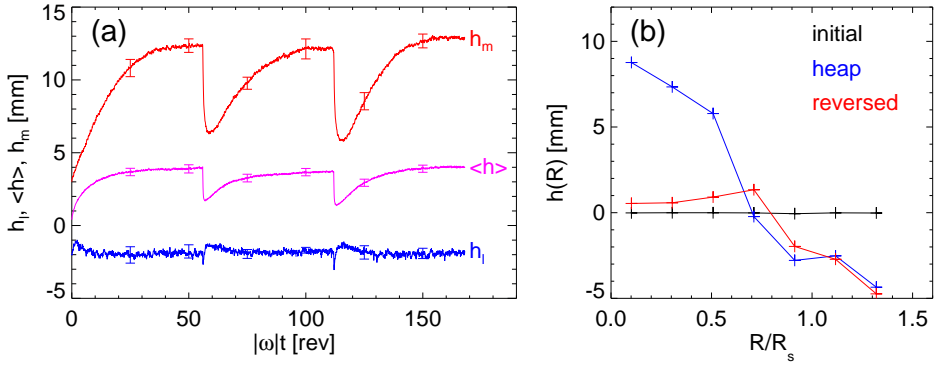


FIGURE 6.15: (a) In this experiment we shear for 53 rev, then shear in the other direction for 53 rev, and then reverse again and shear for 53 rev. Upon reversal, the heap first abruptly disappears and then grows back. This data is for  $Q = 4$  and is averaged over ten runs. (b) The surface profiles  $h(R)$  for the initial surface (black), the steady state heap (blue) and the collapsed heap after reversal (red). This data is for  $Q = 14$ .

reverse the flow direction again, and observe the same behavior. From this experiment we can conclude that the packing in the core of the system is anisotropic. In practice, this could mean that the sheared particles leave empty voids behind, which they can easily reoccupy if the direction of shear is reversed.

### 6.4.3 Convection

The observations that the heap regrows after removal and that particles avalanche down the slopes of the heap, suggest that the heaping is caused by a continuous convective motion that pushes the particles upwards in the center of the system. We test this picture in a simple experiment using colored particles. In this experiment, we prepare the system by putting a layer of colored beads in the core at a certain depth below the surface. When we start shearing the system, we see that after a certain – burying depth-dependent – amount of rotations, the colored particles arise at the surface. When repeating this experiment with spherical particles, we do not observe colored beads at the surface, even after 100 rotations. Using a vacuum cleaner we find that they are still located at their initial position.

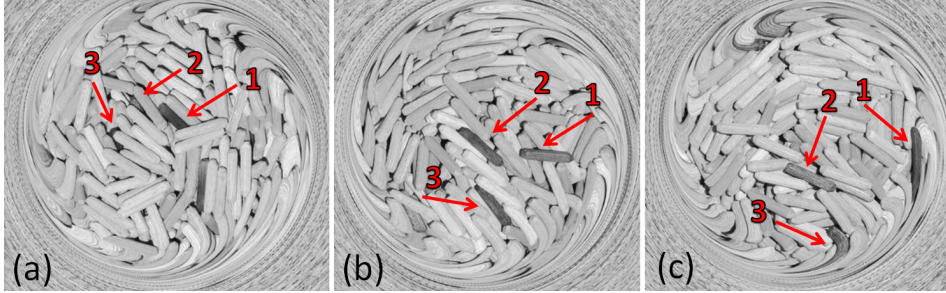


FIGURE 6.16: Three snapshots of continuous heaping. The images are affinely corrected which explains why the sides of the images are blurred. In (a), there are three dark tracer particles rising to the surface, in (b) they are falling down the slope of the hill and in (c) two of the particles disappear in the shear band. This is work in collaboration with T. Börzsönyi.

To visualize the particles that avalanche down the heap, we (in collaboration with T. Börzsönyi – see next section) perform experiments with wooden pegs and make a video of the surface. Using PIV, we correct the frames of this video for the affine motion of the core, so that we can easily see the motion of each individual particle. In Fig. 6.16 we show three snapshots of the video. The blurred outside of the pictures is caused by the affine correction which is only set to correct the motion of the inner part of the system. In (a), there are three dark tracer particles rising to the surface, in (b) they are falling down the slope of the heap and in (c) two of the particles disappear in the shear band. The cyclic raising and disappearing of the tracer particles is a clear visualization of the convection.

#### 6.4.4 Conclusion

From the experiments that are described in Sec. 6.3 and 6.4, we can conclude several things about the heap formation.

From the filling height dependence we learn that heaps only reach a significant height when there is precession. It is easy to imagine that, when there is no precession, the core is not “fluidized” enough to allow heaping. On the other hand, this could also indicate that the gradient in the angular velocity actually drives the heaping. The amount of precession depends on  $R$  [79], and there is more shear between horizontal planes

as  $R$  increases towards  $R_s$ . This could explain why the heap is off-center for  $Q = 4$ , and why we only see a ridge on the inside of the shear band for low filling heights.

Whereas the heap formation is a robust effect that we find for many different particles with  $Q > 3$ , it is less clear how the surface profiles  $h(R)$  and the local densities of the system vary with particle shape. Fig. 6.12(a) and Fig. 6.13, both for  $Q = 4$  particles, suggest that the shear band as well as the core dilate under shear. In contrast, Fig. 6.9 for  $Q = 14$ , suggests that in the shear band, alignment dominates and the packing compacts, whereas in the core, the dilation wins and the volume expands. We have not studied this systematically and cannot offer precise statements.

The facts that the heap regrows after it has been removed, and that the particles rise to the surface of the heap and then avalanche down its slopes, suggest that the heap formation is caused by convection. In the next section we will study this in more detail using 3D data which is acquired via X-ray tomography.

## 6.5 3D X-ray CT Tomography

To be able to see the flow and orientation of the particles below the surface, we perform heaping experiments in an X-ray CT scanner in collaboration with the groups of T. Börzsönyi (Budapest) and R. Stannarius (Magdeburg) [123, 124, 137–139].

### 6.5.1 Setup and Methods

The experiments are performed in a split-bottom cell with an outer radius of 19.5 cm. The inner disk is attached just above the bottom of the container and has a radius of 13 cm and a thickness of 6 mm. In this setup, we shear the particles by rotating the side wall and the outside of the bottom disk. This is in contrast with the setup that was introduced in Sec. 6.2.1, where we drove the system via the inner disk. The reason for this originates from the fact that, because of the CT scanner, the setup cannot contain metal parts and has to be driven by hand. However, there is no difference between rotating the bottom disk or the outer wall in the quasi-static regime in which we measure. The cell is filled to a filling height

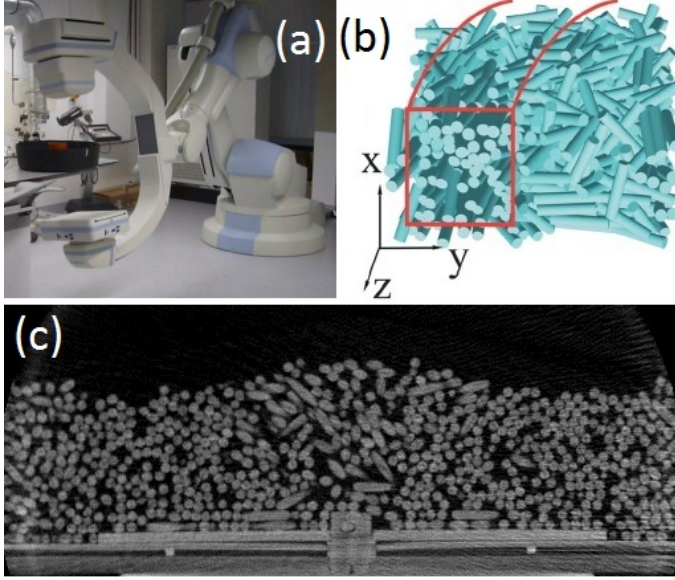


FIGURE 6.17: (a) A picture of the setup placed in the scanner. (b) Visualization of the position and orientation of the particles as reconstructed using a tracing program [138]. (c) An example of a slice through the system made with the X-ray tomograph.

$h_0/R_s = 0.54$  with cylindrical wooden (IKEA ®) pegs with dimensions  $2.5 \times 0.5 \times 0.5 \text{ mm}^3$ .

The scanner is a medical X-ray angiography machine (Siemens Artis zeego) at the INKA lab, Otto von Guericke University, Magdeburg. It consists of a rotational C-arm based X-ray source mounted on a high-precision robot-arm with a flat-panel detector, featuring high resolution whole volume computer tomography [138]. We make a scan after each  $1/16$  of a rotation and obtain a spatial resolution of  $0.49 \text{ mm/voxel}$  – which is significant to identify individual particles. A picture of the scanner and the measuring cell is shown in Fig. 6.17(a).

In Fig. 6.17(c) we show an example of a slice obtained by the X-ray device. From these images we can extract local densities (by simply thresholding the image and counting the light voxels), and particle orientations (via PIV). We can also track each individual particle, and obtain its precisely location and orientation – see Fig. 6.17(b).



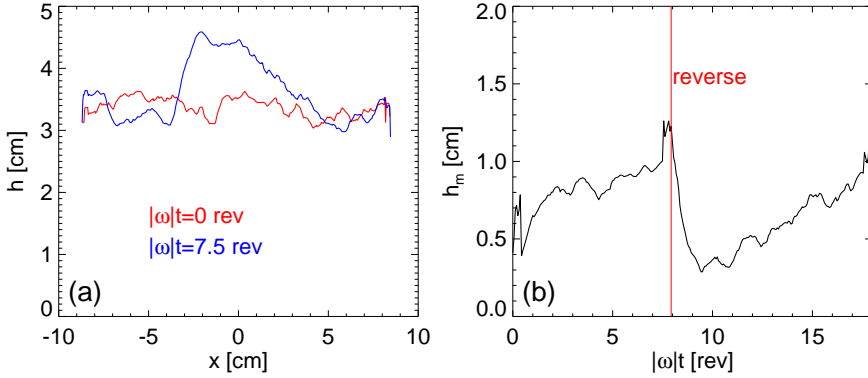


FIGURE 6.18: (a) The shape of the initial surface (red) and after 7.5 rev (blue). (b)  $h_m$  for a run where we reverse the direction of the flow.

## 6.5.2 Results

To get a first impression of the data, we threshold the images that correspond to the slice through the center of the cell (Fig. 6.17(c)), and find the boundary of the packing to recover the shape of the surface (Fig. 6.18(a)) and the heap height (Fig. 6.18(b)). The contrast between the black background and the white particles is large enough so that we can find a threshold value in between the intensity of the particles and the background. This way, we count the percentage of white voxels and obtain a packing fraction of roughly 65%. By finding the height of the packing,  $h$ , as a function of the horizontal coordinate  $x$ , we recover the surface shape  $h(x)$  and heap height  $h_m$ . Fig. 6.18 shows that the global heaping behavior is similar to the results reported in Sec. 6.3.

In Fig. 6.19 we show the density  $\Phi$  (color) and velocity (arrows), obtained by PIV, as a function of  $R$  and  $z$ . The data is averaged over  $\phi$  and 83 scans of the full system, which corresponds to approximately 5 rotations, all in steady state. In the density field we not only observe the shape of the heap, but also that the density is slightly lower in the shear band than in the core. In the shear band,  $\dot{\gamma}$  is higher than in the core, so the data suggests that, for these particles, a higher  $\dot{\gamma}$  favors dilation. This is consistent with our results of Fig. 6.9 and Fig. 6.12, which showed that, for  $Q = 4$  particles, dilatancy is dominant in the shear band.

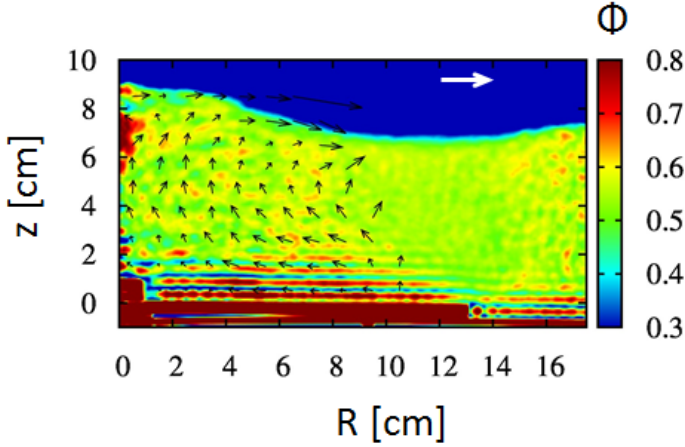


FIGURE 6.19: Density  $\Phi$  (color) and velocity (arrows) as a function of  $R$  and  $z$ . The data is averaged over  $\phi$  and 83 scans of the full system, which corresponds to approximately 5 rotations, all in steady state. The density field shows that the density is slightly lower in the shear band than in the core. The velocity field shows a clear convective roll that pushes the particles upwards for small  $R$ . For large  $R$ , we cannot do PIV because the particle displacements in between two scans are too large to see which particle corresponds to which particle in between two frames. The white scale arrow represents a convection speed of 0.055 cm/rev, which is  $1.4 \times 10^{-3}$  times the main velocity of the grains - in the shear band just outside the inner disk - that corotate with the outer wall.

The velocity field, visualized with the arrows, shows a clear convective roll that pushes the particles upwards at small  $R$ . At the top of the heap, the particles avalanche down the heap with relatively high velocity, just as observed in Sec. 6.3.

We continue our analysis by obtaining the orientation tensor  $T$ :

$$T_{ij} = \frac{3}{2N} \sum_{n=1}^N [l_i^{(n)} l_j^{(n)} - \frac{1}{3} \delta_{ij}], \quad (6.1)$$

where  $l^{(n)}$  is a unit vector along the long axis of particle  $n$  [123]. The eigenvalues of  $T$ ;  $T_{rr}$ ,  $T_{\phi\phi}$  and  $T_{zz}$  correspond to the amount of alignment in the radial, tangential and vertical direction. A value of 1 corresponds to perfect alignment, a value of -0.5 to an alignment in one of the other two

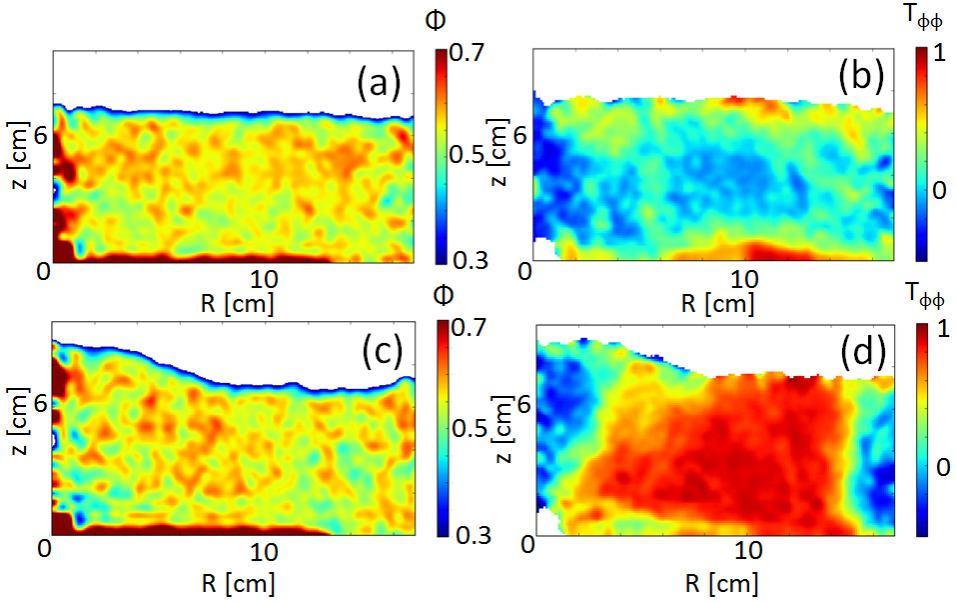


FIGURE 6.20: The density field (a) and eigenvalue  $T_{\phi\phi}$  of the orientation tensor (b) for the initial packing and for the packing after 10.5 rev when a heap has formed (c-d). (a) and (c) show that the density has become slightly lower when the heap has formed. (b-d) show that the difference in alignment is enormous.

directions. We find that the alignment in the tangential direction ( $T_{\phi\phi}$ ) is the strongest. In Fig. 6.20 we show the density  $\phi$  and  $T_{\phi\phi}$  before and after the formation of the heap. It can be seen that the density is slightly lower when the heap has formed, but the difference is small. On the contrary, the difference in alignment before and after the flow is enormous. Initially, the particles are not aligned, but after a shear of 10.5 rev, the particles are aligned in the flow direction in a large part of the system.

### 6.5.3 Origin of the Convection

Now that we have clearly seen that the heaping is the result of convection, we want to know what drives the convection rolls. There are strong indications that the heaping process is related to the breaking of symmetry in the system. We note that, irrespective of the shear direction, the convec-

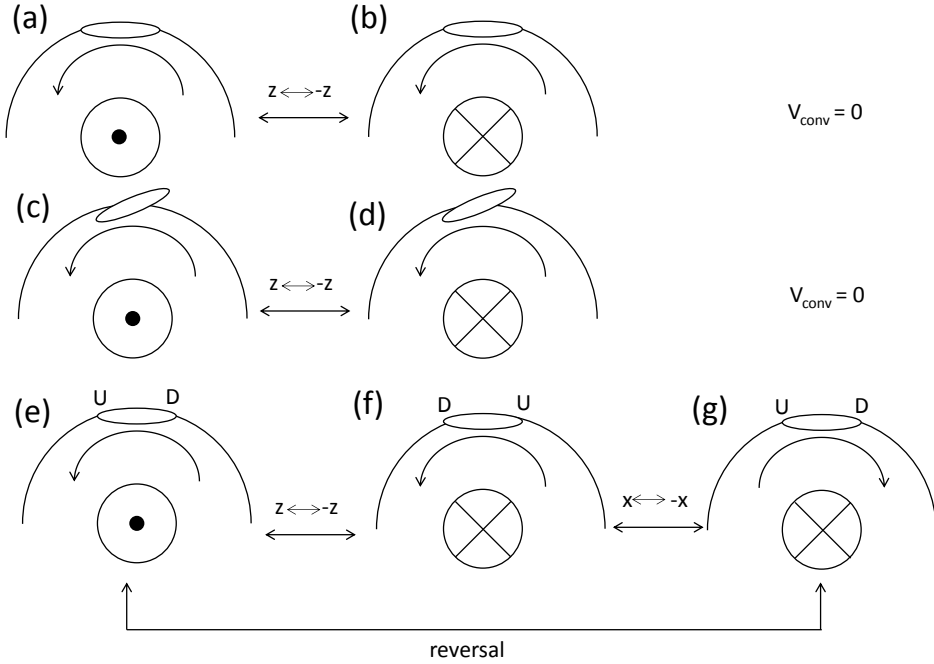


FIGURE 6.21: Using a schematic representation of the particle orientation, shear direction and convection direction, we investigate which particle orientation effect is allowed to cause the heaping by symmetry (see text).

tive flow is always upwards for low  $R$ . However, when we reverse the flow direction once a heap has already grown, the convection initially works in the inverse direction (Fig. 6.15). This suggests that the main flow leads to orientation of the grains, which is crucial to drive the secondary flow – something that is absent for spherical grains.

**Symmetry** – To investigate which particle orientation effect could cause the heaping, we identify which effect is allowed by symmetry. The basic idea is as follows: We take the  $z$ -reflection of the experiment, and consider whether this changes the direction of the convection with respect to the other properties of the system. If the  $z$ -reflection alters only the direction of the convection, and lets the other properties of the experiment

unaffected, then we know that, by symmetry, the speed of the convection,  $v_{\text{conv}}$ , has to be zero.

Of course, the  $z$ -symmetry of the system is broken by both gravity and the shape of the shear band. However, if we reverse the shear direction, the shear band shape and gravity are unaffected, but, initially, the convection does change direction, leading to the vanishing of the heap. Additionally, if the heaping were caused by the gravity or the flow profile, it is expected to also occur for spherical particles – but it does not. Hence, we rule out gravity and flow structure as candidates to determine the direction of the heaping.

We will now consider the symmetry of the directions of the convection and the main flow, and the precise orientation of the particles, where from now on, gravity is neglected. In Fig. 6.21 we show schematic representations of the experiment. The simplest case, where the particles are aligned exactly with the streamlines of the flow, is shown in (a-b). If the situation is reflected in the  $z$ -direction, the particle orientation and flow direction remain the same, but the convection changes sign. This means that in this case, the rate of the convection,  $v_{\text{conv}}$ , must be zero. In (c-d) we consider the case where the particles are misaligned in the horizontal plane. In (c), the front side of particle points *inwards* with respect to the streamline. If we take the  $z$ -reflection of this situation, as in (a-b), the misalignment and flow direction stay the same, while the convection does change sign. Again, this implies  $v_{\text{conv}} = 0$ . In (e-g) we break the  $z$ -symmetry by considering particles of which the front side points *upwards* (U) and the back side point *downwards* (D). If we now take the  $z$ -reflection (f), the flow direction is unaltered, but the misalignment of the particles - which is now also in the  $z$ -direction -, and the direction of the heaping, *do* change. This means that in this case,  $v_{\text{conv}}$  does not have to be zero, and convection is allowed by symmetry. In (g), we take the  $x$ -reflection of (f). Here, the misalignment and flow direction change with respect to (f), but the convection does not. The resulting configuration is the situation that is reached when the flow direction is reversed starting from (e). The misalignment is the same, the flow is reversed and the convection reverses, which results in the initial disappearance of the heap. Hence, a vertical misalignment of the particles is consistent with both a finite secondary flow, and a transient reversal of the secondary flow upon reversal of the main flow.

Earlier analysis of the orientation of the particles in the shear band has shown that the particles indeed do not exactly align with the streamlines of the flow [137]. Instead, the front sides of the particles point *inwards* and *upwards*, where the *average* angles  $\theta_a$  and  $\phi_a$  between the orientation of the particles and the streamline are  $10^\circ$  and  $5^\circ$  respectively. In addition, this orientation state is not stable. The particles continuously tumble with a normalized rotation velocity  $\omega = d\theta/d\theta < 0$  for all  $\theta$  [137, 159]. To verify our hypothesis that the convection is caused by the vertical misalignment of the particles, we extract  $\theta_a(|\omega t|)$  and  $\phi_a(|\omega t|)$  from the orientation tensor  $T$ . Since the behavior of the alignment will most likely be different in different parts of the system, we define four different regions where we will monitor the alignment – see Fig. 6.22. The results are shown in Fig. 6.23. In (a), we show the heap height  $h_m$ , where the dashed line indicates the moment when we reverse the shear direction. In (b-c) we plot  $\theta_a$  and  $\phi_a$  for the four different regions.

By definition, the angles change sign when the flow direction is reversed. The time it takes to reorient is, as expected, different for the eight curves. For instance  $\theta_a$  in region C (shear band) reorients relatively fast. We suggest this is because, in the shear band, the shear rate is relatively high. Other angles, such as  $\theta_a$  in region D (high up in the core) and  $\phi_a$  in regions A, B and D (everywhere except the shear band), take much longer to reorient. The number of rotations that this orientational transient persists, in particular for the vertical deviation angle  $\phi_a$  (about 5 rev), corresponds well to the time it takes for the heap to start regrowing. This strongly supports our claim that the convection roll is driven by the vertical deviations between the particle orientations and the streamlines.

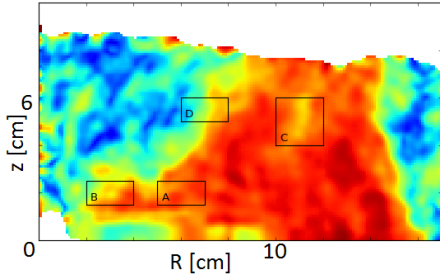


FIGURE 6.22: Indication of the location of regions A, B, C and D where we will monitor the alignment of the particles. The color represents  $s$ , which is the largest eigenvector of  $T$ .

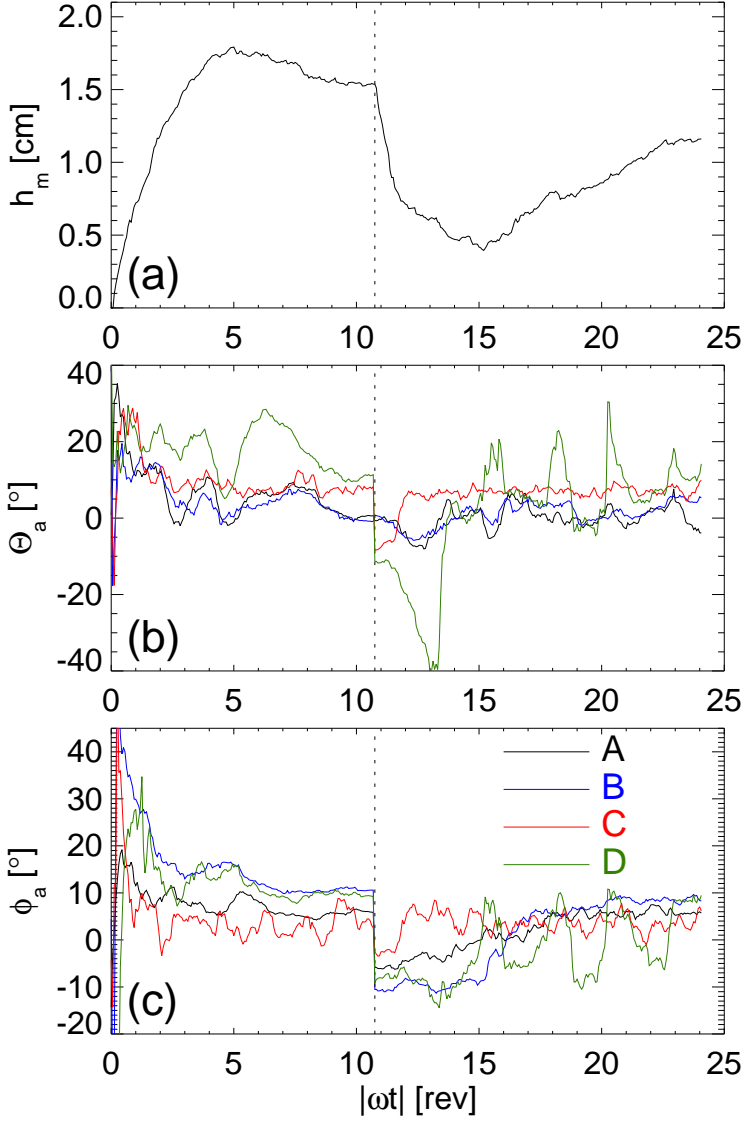


FIGURE 6.23: (a) The heap height  $h_m$  as a function of time for a reversal run. (b) The average horizontal deviation angle  $\Theta_a$  in the four regions as indicated in Fig. 6.22. (c) The average vertical deviation angle  $\phi_a$ . The black dashed line indicates the time when the flow direction is reversed. It can be seen that different parts of the system take a different time to reorient. However, the reorientation times, in particular of  $\phi_a$ , correspond well to the time it takes for the heap to start regrowing.

#### 6.5.4 Conclusion

In this section we have seen that in this alternative setup, that allows for 3D imaging, the heaping phenomenon is the same as in the setup of Sec. 6.3. The PIV analysis of the particles in 3D clearly shows a convection roll that is responsible for the heaping. We have presented a symmetry breaking argument and experimental data that explain how the convection is the result of a vertical deviation between the orientation of the (tumbling) particles and the streamlines of the flow. This argument, in addition, correctly captures the transient disappearance of the heap upon reversal.



## 6.A Appendix

### 6.A.1 Outlook

An obvious experiment to do would be to shear oblate (lentils, smarties, coins) particles rather than prolate (rice) ones. We expect these particles to align with the bottom during the filling of the setup, whereas upon shear, the particles in the shear band might orient with the strain rate. Tumbling and heaping could then also occur.

Another experiment would be to shear ratchet-like particles such as wheat grains. A wheat grain is covered with tiny hairs that all point in the same direction. As a result, the grain can easily slide in one direction but not in the other. In a reversal experiment with ratchet particles, we expect a dramatic response after the grains snap from very frustrated positions.

Something that is not yet well understood is how dilatancy and compaction due to alignment compete for different particle shapes and flow geometries. It would be interesting to find an order parameter that indicates how the two effects relate.

More related to the heaping process, it would be interesting to study the details of the convection. In our 3D experiments, we quantified how fast this convection is, but the speed of the convection may vary with the aspect ratio of the particles. Even in experiments without a 3D scanner, this can be measured relatively simply using colored particles. The dependence of the convection speed on particle shape is the subject of current studies in the group of R. Stannarius.



---

# Bibliography

---

- [1] H. M. Jaeger, S. R. Nagel, and R. P. Behringer, *Granular solids, liquids, and gases*, Rev. Mod. Phys. **4** (1996), doi: 10.1103/RevModPhys.68.1259.
- [2] J. Duran, *Sands, Powders, and Grains: An Introduction to the Physics of Granular Materials*, Springer (1999), ISBN: 978-1-4612-6790-4.
- [3] B. Andreotti, Y. Forterre, and O. Pouliquen, *Granular Media: Between Fluid and Solid*, Cambridge University Press (2013), ISBN: 9781107034792.
- [4] K. van der Weele, *Granular gas dynamics: how Maxwell's demon rules in a non-equilibrium system*, Contemporary Physics **49** (2008), doi: 10.1080/00107510802141226.
- [5] P. Dantu, *Etude Statistique des Forces Intergranulaires dans un Milieu Pulverulent*, Géotechnique **18** (1968), doi: 10.1680/geot.1968.18.1.50.
- [6] C. S. Campbell, *Granular material flows - An overview*, Powd. Techn. **162** (2006), doi: 10.1016/j.powtec.2005.12.008.
- [7] R. Hartley and R. Behringer, *Logarithmic rate dependence of force networks in sheared granular materials*, Nature **421** (2003), doi: 10.1038/nature01394.
- [8] J. H. Snoeijer, W. G. Ellenbroek, T. J. H. Vlugt, and M. van Hecke, *Sheared Force Networks: Anisotropies, Yielding, and Geometry*, Phys. Rev. Lett. **96** (2006), doi: 10.1103/PhysRevLett.96.098001.
- [9] H. Janssen, *Versuche Über Getreidedruck in Silozellen*, Z. Ver. Dt. Ing. **39** (1895).
- [10] I. Goldhirsch, *Clustering Instability in Dissipative Gases*, Phys. Rev. Lett. **70** (1993), doi: 10.1103/PhysRevLett.70.1619.
- [11] J. Eggers, *Sand as Maxwell's Demon*, Phys. Rev. Lett. **83** (1999), doi: 10.1103/PhysRevLett.83.5322.
- [12] A. J. Liu and S. R. Nagel, *Jamming is not just cool any more*, Nature **396** (1998), doi: 10.1038/23819.

## Bibliography

---

- [13] J. Dijkstra, *Granular Media: Flow & Agitations*, Ph.D. thesis, Leiden University (2009).
- [14] W. Ellenbroek, Z. Zeravic, W. van Saarloos, and M. van Hecke, *Non-affine response: Jammed packings vs. spring networks*, *Europhys. Lett.* **87** (2009), doi: 10.1209/0295-5075/87/34004.
- [15] C. Coulomb, *Essai sur une application des regles des maximis et minimis a quelques problemes de statique relatifs, a la architecture*, *Mem. Acad. Roy. Div. Sav.* **7** (1776).
- [16] M. Faraday, *On a peculiar class of acoustical figures*, *Philos. Trans. R. Soc. London* **121** (1831), doi: 10.1098/rstl.1831.0018.
- [17] G. Hagen, *Über den Druck und die Bewegung des trocknen Sandes*, *Ber. Akad. Wiss. Berlin* (1852).
- [18] O. Reynolds, *On the Dilatancy of Media composed of rigid particles in contact*, *Phil. Mag. S. 20* (1885), doi: 10.1080/14786448508627791.
- [19] R. Bagnold, *The Physics of Blown Sand and Desert Dunes*, Methuen (1941).
- [20] B. Ennis, J. Green, and R. Davies, *The legacy of neglect in the US*, *Chem. Eng. Prog.* **90** (1994).
- [21] J. Knight, H. Jaeger, and S. Nagel, *Vibration-induced size separation in granular media: The convection connection*, *Phys. Rev. Lett.* **70** (1993), doi: 10.1103/PhysRevLett.70.3728.
- [22] P. de Gennes, *Superconductivity Of Metals And Alloys*, Addison-Wesley Publishing Company (1966), ISBN: 0738201014.
- [23] M. Roberts and B. Field, *2011 Summary of Grain Entrapments in the United States* (2012).
- [24] M. Möbius, S. R. Nagel, and H. M. Jaeger, *Brazil-nut effect: Size separation of granular particles*, *Nature* **414** (2001), doi: 10.1038/35104697.
- [25] K. Nichol, *Fluidization and Fluctuations in Granular Systems*, Ph.D. thesis, Leiden University (2011).
- [26] A. Khaldoun, E. Eiser, G. H. Wegdam, and D. Bonn, *Liquefaction of quicksand under stress*, *Nature* **437** (2005), doi: 10.1038/437635a.
- [27] D. Lohse, R. Rauhé, R. Bergmann, and D. van der Meer, *Creating a dry variety of quicksand*, *Nature* **432** (2004), doi: 10.1038/432689a.
- [28] E. Brown, N. Rodenberg, H. Lipson, and H. Jaeger, *Universal robotic gripper based on the jamming of granular material*, *Proc. Natl. Acad. Sci.* **107** (2010), doi: 10.1073/pnas.1003250107.

- 
- [29] J. Amend, E. Brown, N. Rodenberg, H. Jaeger, and H. Lipson, *A Positive Pressure Universal Gripper Based on the Jamming of Granular Material*, IEEE Trans. Robot. **28** (2012), doi: 10.1109/TRO.2011.2171093.
- [30] Cornell Creative Machines Lab, *Robotic grippers based on granular jamming*, URL [http://www.youtube.com/watch?v=ZK0I\\_1VDPpw](http://www.youtube.com/watch?v=ZK0I_1VDPpw).
- [31] A. Winfield, *Soft robotics in space*, Robohub (2014), URL <http://robohub.org/soft-robotics-in-space/>.
- [32] M. Miskin and H. Jaeger, *Adapting granular materials through artificial evolution*, Nature Mater. **12** (2013), doi: 10.1038/nmat3543.
- [33] S. R. Waitukaitis and H. M. Jaeger, *Impact-activated solidification of dense suspensions via dynamic jamming fronts*, Nature **487** (2012), doi: 10.1038/nature11187.
- [34] B. Killeen, *Bumpfree Dynamic Speed Bump*, Master's thesis, Newcastle University (2012).
- [35] P. Khant, L. Yuen, and T. Chye, *Development of High Energy Dissipation Composite System Utilizing Shear Thickening Materials*, Master's thesis, National University of Singapore (2011).
- [36] GDR MiDi, *On dense granular flows.*, Eur. Phys. J. E Soft Matter **14** (2004), doi: 10.1140/epje/i2003-10153-0.
- [37] Y. Forterre and O. Pouliquen, *Flows of Dense Granular Media*, Annu. Rev. Fluid Mech. **40** (2008), doi: 10.1146/annurev.fluid.40.111406.102142.
- [38] K. Nichol, A. Zanin, R. Bastien, E. Wandersman, and M. van Hecke, *Flow-Induced Agitations Create a Granular Fluid*, Phys. Rev. Lett. **104** (2010), doi: 10.1103/PhysRevLett.104.078302.
- [39] I. Sánchez, F. Raynaud, J. Lanuza, B. Andreotti, E. Clément, and I. S. Aranson, *Spreading of a granular droplet*, Phys. Rev. E **76** (2007), doi: 10.1103/PhysRevE.76.060301.
- [40] D. Rubin, N. Goldenson, and G. A. Voth, *Failure and strengthening of granular slopes under horizontal vibration*, Phys. Rev. E **74** (2006), doi: 10.1103/PhysRevE.74.051307.
- [41] H. Jaeger, C. Liu, and S. Nagel, *Relaxation at the Angle of Repose*, Phys. Rev. Lett. **62** (1989), doi: 10.1103/PhysRevLett.62.40.
- [42] P. Marchal, N. Smirani, and L. Choplin, *Rheology of dense-phase vibrated powders and molecular analogies*, J. Rheol. **53** (2009), doi: 10.1122/1.3037266.
- [43] A. Janda, D. Maza, A. Garcimartin, E. Kolb, J. Lanuza, and E. Clément, *Unjamming a granular hopper by vibration*, Europhys. Lett. **87** (2009), doi: 10.1209/0295-5075/87/24002.

## Bibliography

---

- [44] K. Reddy, Y. Forterre, and O. Pouliquen, *Evidence of Mechanically Activated Processes in Slow Granular Flows*, Phys. Rev. Lett. **106** (2011), doi: 10.1103/PhysRevLett.106.108301.
- [45] F. Guillard, Y. Forterre, and O. Pouliquen, *Depth-Independent Drag Force Induced by Stirring in Granular Media*, Phys. Rev. Lett. **110** (2013), doi: 10.1103/PhysRevLett.110.138303.
- [46] K. Nichol and M. van Hecke, *Flow-induced agitations create a granular fluid: Effective viscosity and fluctuations*, Phys. Rev. E **85** (2012), doi: 10.1103/PhysRevE.85.061309.
- [47] E. Wandersman and M. van Hecke, *Nonlocal Granular Rheology: Role of Pressure and Anisotropy*, Europhys. Lett. **105** (2014), doi: 10.1209/0295-5075/105/24002.
- [48] K. Desmond, U. Villa, M. Newey, and W. Losert, *Characterizing the rheology of fluidized granular matter*, Phys. Rev. E **88** (2013), doi: 10.1103/PhysRevE.88.032202.
- [49] M. Y. Karim and E. Corwin, *Eliminating Friction with Friction: 2D Janssen Effect in a Friction-Driven System*, Phys. Rev. Lett. **112** (2014), doi: 10.1103/PhysRevLett.112.188001.
- [50] M. Bouzid, M. Trulsson, P. Claudin, E. Clément, and B. Andreotti, *A non-local rheology for granular flows across yield conditions*, Phys. Rev. Lett. **111** (2013), doi: 10.1103/PhysRevLett.111.238301.
- [51] M. Falk and J. Langer, *Dynamics of viscoplastic deformation in amorphous solids*, Phys. Rev. E **57** (1998), doi: 10.1103/PhysRevE.57.7192.
- [52] P. Sollich, F. Lequeux, P. Hébraud, and M. Cates, *Rheology of Soft Glassy Materials*, Phys. Rev. Lett. **78** (1997), doi: 10.1103/PhysRevLett.78.2020.
- [53] D. Krimer, S. Mahle, and M. Liu, *Dip of the granular shear stress*, Phys. Rev. E **86** (2012), doi: 10.1103/PhysRevE.86.061312.
- [54] J. Goyon, A. Colin, G. Ovarlez, A. Ajdari, and L. Bocquet, *Spatial cooperativity in soft glassy flows*, Nature **454** (2008), doi: 10.1038/nature07026.
- [55] N. Swisher and B. Utter, *Flow profile of granular avalanches with imposed vertical vibration*, Granul. Matter **16** (2014), doi: 10.1007/s10035-014-0488-2.
- [56] C. Mankoc, A. Garcimartín, I. Zuriguel, and D. Maza, *Role of vibrations in the jamming and unjamming of grains discharging from a silo*, Phys. Rev. E **80** (2009), doi: 10.1103/PhysRevE.80.011309.
- [57] G. Caballero-Robledo and E. Clément, *Rheology of a sonofluidized granular packing*, Eur. Phys. J. E Soft Matter **30** (2009), doi: 10.1140/epje/i2009-10537-0.
- [58] G. Caballero, E. Kolb, A. Lindner, J. Lanuza, and E. Clément, *Experimental investigation of granular dynamics close to the jamming transition*, J. Phys. Cond. Matt. **17** (2005), doi: 10.1088/0953-8984/17/24/009.

- 
- [59] C. Coulais, R. P. Behringer, and O. Dauchot, *Dynamics of the contacts reveals Widom lines for jamming*, Europhys. Lett. **100** (2012), doi: 10.1209/0295-5075/100/44005.
- [60] E. Longhi, N. Easwar, and N. Menon, *Large Force Fluctuations in a Flowing Granular Medium*, Phys. Rev. Lett. **89** (2002), doi: 10.1103/PhysRevLett.89.045501.
- [61] P. Schall and M. van Hecke, *Shear Bands in Matter with Granularity*, Ann. Rev. Fluid Mech. **42** (2010), doi: 10.1146/annurev-fluid-121108-145544.
- [62] J. Crassous, J.-F. Métayer, P. Richard, and C. Laroche, *Experimental study of a creeping granular flow at very low velocity*, J. Stat. Mech. **44** (2008), doi: 10.1088/1742-5468/2008/03/P03009.
- [63] A. Amon, V. Nguyen, A. Bruand, J. Crassous, and E. Clément, *Hot Spots in an Athermal System*, Phys. Rev. Lett. **108** (2012), doi: 10.1103/PhysRevLett.108.135502.
- [64] E. Jagla, *Finite width of quasistatic shear bands*, Phys. Rev. E **78** (2008), doi: 10.1103/PhysRevE.78.026105.
- [65] J. Török, T. Unger, J. Kertész, and D. E. Wolf, *Shear zones in granular materials: Optimization in a self-organized random potential*, Phys. Rev. E **75** (2007), doi: 10.1103/PhysRevE.75.011305.
- [66] M. Depken, W. van Saarloos, and M. van Hecke, *Continuum approach to wide shear zones in quasistatic granular matter*, Phys. Rev. E **73** (2006), doi: 10.1103/PhysRevE.73.031302.
- [67] P. Marchal, C. Hanotin, L. Michot, and S. K. de Richter, *Two-state model to describe the rheological behavior of vibrated granular matter*, Phys. Rev. E **88** (2013), doi: 10.1103/PhysRevE.88.012207.
- [68] K. Kamrin and G. Koval, *Nonlocal Constitutive Relation for Steady Granular Flow*, Phys. Rev. Lett. **108** (2012), doi: 10.1103/PhysRevLett.108.178301.
- [69] D. Henann and K. Kamrin, *A predictive, size-dependent continuum model for dense granular flows*, Proc. Natl. Acad. Sci. **110** (2013), doi: 10.1073/pnas.1219153110.
- [70] D. Henann and K. Kamrin, *Continuum Modeling of Secondary Rheology in Dense Granular Materials* (2014), arXiv:1408.3884v1.
- [71] J. Dijkstra, G. Wortel, L. van Dellen, O. Dauchot, and M. van Hecke, *Jamming, Yielding and Rheology of Weakly Vibrated Granular Media*, Phys. Rev. Lett. **107** (2011), doi: 10.1103/PhysRevLett.107.108303.
- [72] A. Suzuki and T. Tanaka, *Measurement of Flow Properties of Powders along an Inclined Plane*, Ind. Eng. Chem. Fundom. **10** (1971).
- [73] O. Pouliquen, *Scaling laws in granular flows down rough inclined planes*, Phys. Fluids **11** (1999), doi: 10.1063/1.869928.

## Bibliography

---

- [74] D. A. Weitz, *Colloidal Glasses*, Glasses and Grains **61** (2011), doi: 10.1007/978-3-0348-0084-6.
- [75] G. Marty and O. Dauchot, *Subdiffusion and Cage Effect in a Sheared Granular Material*, Phys. Rev. Lett. **94** (2005), doi: 10.1103/PhysRevLett.94.015701.
- [76] J. A. Dijksman and M. van Hecke, *Granular flows in split-bottom geometries*, Soft Matter **6** (2010), doi: 10.1039/b925110c.
- [77] D. Fenistein, J.-W. van de Meent, and M. van Hecke, *Core Precession and Global Modes in Granular Bulk Flow*, Phys. Rev. Lett. **96** (2006), doi: 10.1103/PhysRevLett.96.118001.
- [78] D. Fenistein and M. van Hecke, *Wide shear zones in granular bulk flow*, Nature **425** (2003), doi: 10.1038/425256a.
- [79] D. Fenistein, J.-W. van de Meent, and M. van Hecke, *Universal and Wide Shear Zones in Granular Bulk Flow*, Phys. Rev. Lett. **92** (2004), doi: 10.1103/PhysRevLett.92.094301.
- [80] J. Dijksman, E. Wandersman, S. Slotterback, C. Berardi, R. Christian, W. Updegraff, M. van Hecke, and W. Losert, *From frictional to viscous behavior: Three-dimensional imaging and rheology of gravitational suspensions*, Phys. Rev. E **82** (2010), doi: 10.1103/PhysRevE.82.060301.
- [81] G. Wortel, J. Dijksman, and M. van Hecke, *Rheology of weakly vibrated granular media*, Phys. Rev. E **89** (2014), doi: 10.1103/PhysRevE.89.012202.
- [82] X. Cheng, J. B. Lechman, A. Fernandez-Barbero, G. S. Grest, H. M. Jaeger, G. S. Karczmar, M. E. Möbius, and S. R. Nagel, *Three-Dimensional Shear in Granular Flow*, Phys. Rev. Lett. **93** (2006), doi: 10.1103/PhysRevLett.96.038001.
- [83] R. Moosavi, M. R. Shaebani, M. Maleki, J. Török, D. E. Wolf, and W. Losert, *Coexistence and Transition between Shear Zones in Slow Granular Flows*, Phys. Rev. Lett. **111** (2013), doi: 10.1103/PhysRevLett.111.148301.
- [84] A. Singh, V. Magananim, K. Saitoh, and S. Lunding, *Effect of cohesion on shear banding in quasi-static granular material*, Phys. Rev. E **90** (2014), doi: 10.1103/PhysRevE.90.022202.
- [85] E. Wandersman, J. Dijksman, and M. van Hecke, *Particle diffusion in slow granular bulk flows*, Europhys. Lett. **100** (2012), doi: 10.1209/0295-5075/100/38006.
- [86] J.-Y. Chastaing and A. Kudrolli, *Crystal order in vibrated granular rods*, Master's thesis, Clark University (2011).
- [87] O. Kuwano, T. Hatano, and R. Ando, *Crossover from negative to positive shear rate dependence in granular friction*, Geophys. Res. Lett. **40** (2013), doi: 10.1002/grl.50311.



- 
- [88] H. Jaeger, H.-H. Liu, S. Nagel, and T. Witten, *Friction in Granular Flows*, Europhys. Lett. **11** (1990), doi: 10.1209/0295-5075/11/7/007.
  - [89] P. Coussot, *Rheometry of Pastes, Suspensions, and Granular Materials*, Wiley-Interscience (2005), ISBN: 978-0-471-65369-1.
  - [90] P. Jop, J. Forterre, and O. Pouliquen, *A constitutive law for dense granular flows*, Nature **441** (2006), doi: 10.1038/nature04801.
  - [91] L. Bureau, T. Baumberger, and C. Caroli, *Rheological aging and rejuvenation in solid friction contacts*, Eur. Phys. J. E **8** (2002), doi: 10.1140/epje/i2002-10017-1.
  - [92] P. Hähner and Y. Drossinos, *Nonlinear dynamics of a continuous spring - block model of earthquake faults*, J. Phys. A: Math. Gen. **31** (1998), doi: 10.1088/0305-4470/31/10/002.
  - [93] O. Pouliquen, C. Cassar, P. Jop, Y. Forterre, and M. Nicolas, *Flow of dense granular material: towards simple constitutive laws*, J. Stat. Mech. (2006), doi: 10.1088/1742-5468/2006/07/P07020.
  - [94] R. M. Nedderman and C. Laohaku, *The thickness of the shear zone of flowing granular materials*, Powd. Techn. **25** (1980), doi: 10.1016/0032-5910(80)87014-8.
  - [95] T. Unger, J. Török, J. Kertész, and D. Wolf, *Shear Band Formation in Granular Media as a Variational Problem*, Phys. Rev. Lett. **92** (2004), doi: 10.1103/PhysRevLett.92.214301.
  - [96] G. Wortel and M. van Hecke, *Anisotropy of weakly vibrated granular flows* (2014), arXiv: 1410.4335.
  - [97] M. Depken, J. B. Lechman, M. van Hecke, W. van Saarloos, and G. S. Grest, *Stresses in smooth flows of dense granular media*, Europhys. Lett. **78** (2007), doi: 10.1209/0295-5075/78/58001.
  - [98] M. Menon and D. Durian, *Particle Motions in a Gas-Fluidized Bed of Sand*, Phys. Rev. Lett. **79** (1997), doi: 10.1103/PhysRevLett.79.3407.
  - [99] M. Möbius, X. Cheng, P. Esthuis, G. Karczmar, S. Nagel, and H. Jaeger, *Effect of air on granular size separation in a vibrated granular bed*, Phys. Rev. E **72** (2005), doi: 10.1103/PhysRevE.72.011304.
  - [100] J. D. van der Waals, *Over de continuïteit van den gas- en vloeistofoestand*, Ph.D. thesis, Leiden University (1873).
  - [101] E. Ising, *Beitrag zur Theorie des Ferro- und Paramagnetismus*, Ph.D. thesis, University of Hamburg (1924).
  - [102] L. Onsager, *Crystal Statistics. I. A Two-Dimensional Model with an Order-Disorder Transition*, Phys. Rev. Lett. **65** (1944), doi: 10.1103/PhysRev.65.117.

## Bibliography

---

- [103] L. Landau, *On the theory of phase transitions*, Zh. Eksp. Teor. Fiz. **7** (1937).
- [104] L. Kadanoff, *More is the Same; Phase Transitions and Mean Field Theories*, J. Stat. Mech. **137** (2009), doi: 10.1007/s10955-009-9814-1.
- [105] H. Eerkens, G. Wortel, and M. van Hecke, *Fluctuations and transitions in weakly vibrated granular matter*, Master's thesis, Leiden University (2012).
- [106] National Instruments, *Encoder Measurements: How-To Guide* (2013).
- [107] Heidenhain, *Encoders for Servo Drivers* (2011).
- [108] C. Garrod, *Statistical Mechanics and Thermodynamics*, Oxford University Press (1995).
- [109] D. Beysens, J. Straub, and D. Turner, *Phase Transitions and Near-Critical Phenomena*, Springer (1987).
- [110] V. V. Vladimirsky, *To the question of the evaluation of mean products of two quantities, related to different moments of time, in statistical mechanics*, Zh. Eksp. Teor. Fiz. **12** (1942).
- [111] V. Brazhkin, Y. D. Fomin, A. Lyapin, V. Ryzhov, and K. Trachenko, *Two liquid states of matter: A dynamic line on a phase diagram*, Phys. Rev. E **85** (2012), doi: 10.1103/PhysRevE.85.031203.
- [112] H. E. Stanley, *Scaling, universality, and renormalization: Three pillars of modern critical phenomena*, Rev. Mod. Phys. **71** (1999), doi: 10.1103/RevModPhys.71.S358.
- [113] C. Bonnoit, J. Lanuza, A. Lindner, and E. Clément, *Mesoscopic Length Scale Controls the Rheology of Dense Suspensions*, Phys. Rev. Lett. **105** (2010), doi: 10.1103/PhysRevLett.105.108302.
- [114] L. Bocquet, A. Colin, and A. Ajdari, *Kinetic Theory of Plastic Flow in Soft Glassy Materials*, Phys. Rev. Lett. **103** (2009), doi: 10.1103/PhysRevLett.103.036001.
- [115] V. Mansard, A. Colin, P. Chauduri, and L. Bocquet, *A kinetic elasto-plastic model exhibiting viscosity bifurcation in soft glassy materials*, Soft Matter **7** (2011), doi: 10.1039/c1sm05229b.
- [116] V. Mansard, A. Colin, P. Chauduri, and L. Bocquet, *A molecular dynamics study of non-local effects in the flow of soft jammed particles*, Soft Matter **9** (2013), doi: 10.1039/C3SM50847A.
- [117] M. Toiya, J. Stambaugh, and W. Losert, *Transient and Oscillatory Granular Shear Flow*, Phys. Rev. Lett. **93** (2004), doi: 10.1103/PhysRevLett.93.088001.
- [118] B. Utter and R. Behringer, *Transients in sheared granular matter*, Eur. Phys. J. E Soft Matter **14** (2004), doi: 10.1140/epje/i2004-10022-4.

- 
- [119] T. S. Majmudar and R. Behringer, *Contact force measurements and stress-induced anisotropy in granular materials*, *Nature* **435** (2005), doi: 10.1038/nature03805.
- [120] N. Guo and J. Zhao, *The signature of shear-induced anisotropy in granular media*, *Comput. Geotech.* **47** (2013), doi: 10.1016/j.compgeo.2012.07.002.
- [121] M. Oda, S. Nemat-Nasser, and J. Konishi, *Stress-Induced Anisotropy in Granular Masses*, *Soils Found.* **25** (1985).
- [122] E. Collins and B. Muhunthan, *On the relationship between stress-dilatancy, anisotropy, and plastic dissipation for granular materials*, *Géotechnique* **23** (2003), doi: 10.1680/geot.2003.53.7.611.
- [123] T. Börzsönyi, S. Wegner, and R. Stannarius, *Orientational Order and Alignment of Elongated Particles Induced by Shear*, *Phys. Rev. Lett.* **108** (2012), doi: 10.1103/PhysRevLett.108.228302.
- [124] B. Szabó, J. Török, E. Somfai, S. Wegner, R. Stannarius, A. Böse, G. Rose, F. Angenstein, and T. Börzsönyi, *Evolution of shear zones in granular materials*, *Phys. Rev. E* (2014), doi: 10.1103/PhysRevE.90.032205.
- [125] A. Casagrande, *Characteristics of cohesionless soils affecting the stability of slopes and earth fills*, *J. Boston Soc. Civil Eng.* **23** (1936).
- [126] J. Knight, C. Fandrich, C. Lau, H. Jaeger, and S. Nagel, *Density relaxation in a vibrated granular material*, *Phys. Rev. E* **51** (1995), doi: 10.1103/PhysRevE.51.3957.
- [127] P. Bevington and D. Robinson, *Data Reduction and Error Analysis for the Physical Sciences*, McGraw-Hill Inc (1992), Ch.4.
- [128] A. Gajo and D. M. Wood, *A kinematic hardening constitutive model for sands: the multi-axial formulation*, *Int. J. Num. Anal. Methods Geomech.* **23** (1999), doi: 10.1002/(SICI)1096-9853(19990810)23:9<925::AID-NAG19>3.0.CO;2-M.
- [129] J. Brandt and L. Nilsson, *A constitutive model for compaction of granular media, with account for deformation induced anisotropy*, *Mech. Cohes.-Frict. Mater.* **4** (1999), doi: 10.1002/(SICI)1099-1484(199907)4:4<391::AID-CFM68>3.0.CO;2-0.
- [130] N. Kumar, S. Luding, and V. Magananim, *Macroscopic model with anisotropy based on micro-macro information*, *Acta Mechanica* **225** (2014), doi: 10.1007/s00707-014-1155-8.
- [131] F. X. Villarruel, B. E. Lauderdale, D. M. Mueth, and H. M. Jaeger, *Compaction of rods: Relaxation and ordering in vibrated, anisotropic granular material*, *Phys. Rev. E* **61** (2000), doi: 10.1103/PhysRevE.61.6914.
- [132] G. Lumay and N. Vandewalle, *Compaction of anisotropic granular materials: Experiments and simulations*, *Phys. Rev. E* **70** (2004), doi: 10.1103/PhysRevE.70.051314.

## Bibliography

---

- [133] D. L. Blair, T. Neicu, and A. Kudrolli, *Vortices in vibrated granular rods*, Phys. Rev. E **67** (2003), doi: 10.1103/PhysRevE.67.031303.
- [134] V. Yadav, J.-Y. Chastaing, and A. Kudrolli, *Effect of aspect ratio on the development of order in vibrated granular rods*, Phys. Rev. E **88** (2013), doi: 10.1103/PhysRevE.88.052203.
- [135] J. Galanis, D. Harries, D. L. Sackett, W. Losert, and R. Nossal, *Spontaneous Patterning of Confined Granular Rods*, Phys. Rev. Lett. **96** (2006), doi: 10.1103/PhysRevLett.96.028002.
- [136] V. Narayan, S. Ramaswamy, and N. Menon, *Long-Lived Giant Number Fluctuations in a Swarming Granular Nematic*, Science **317** (2007), doi: 10.1126/science.1140414.
- [137] T. Börzsönyi, S. Wegner, and R. Stannarius, *Shear-induced alignment and dynamics of elongated granular particles*, Phys. Rev. E **86** (2012), doi: 10.1103/PhysRevE.86.051304.
- [138] S. Wegner, T. Börzsönyi, T. Bien, G. Rose, and R. Stannarius, *Alignment and dynamics of elongated cylinders under shear*, Soft Matter **8** (2012), doi: 10.1039/C2SM26452H.
- [139] S. Wegner, R. Stannarius, A. Böse, G. Rose, B. Szabó, E. Somfai, and T. Börzsönyi, *Effects of grain shape on packing and dilatancy of sheared granular materials*, Soft Matter **10** (2014), doi: 10.1039/C4SM00838C.
- [140] T. Börzsönyi and R. Stannarius, *Granular materials composed of shape-anisotropic grains*, Soft Matter **9** (2013), doi: 10.1039/c3sm50298h.
- [141] A. A. Peña, R. García-Rojo, and H. J. Herrmann, *Influence of particle shape on sheared dense granular media*, Granular Matter **9** (2007), doi: 10.1007/s10035-007-0038-2.
- [142] V. Frette, K. Christensen, A. Målthe-Sørensen, J. Feder, T. Jøssang, and P. Meakin, *Avalanche dynamics in a pile of rice*, Nature **379** (1996), doi: 10.1038/379049a0.
- [143] C. S. Campbell, *Elastic granular flows of ellipsoidal particles*, J. Fluid Mech. **23** (2011), doi: 10.1063/1.3546037.
- [144] E. Ben-Naim and P. Krapivsky, *Alignment of rods and partition of integers*, Phys. Rev. E **73** (2006), doi: 10.1103/PhysRevE.73.031109.
- [145] Y. Tao, W. Otter, and W. Briels, *Kayaking and Wagging of Rods in Shear Flow*, Phys. Rev. Lett. **95** (2005), doi: 10.1103/PhysRevLett.95.237802.
- [146] M. Ripoll, P. Holmqvist, R. G. Winkler, G. Gompper, J. Dhont, and M. P. Lettinga, *Attractive Colloidal Rods in Shear Flow*, Phys. Rev. Lett. **101** (2008), doi: 10.1103/PhysRevLett.101.168302.
- [147] Psidot, *The Weissenberg Effect*, URL <http://www.youtube.com/watch?v=npZzlgKjs0I>.

- 
- [148] E. Soto, O. Endríquez, R. Zenit, and O. Manero, *Rodless Weissenberg Effect* (2008), arXiv:0810.1551.
- [149] K. Weissenberg, *A Continuum Theory of Rheological Phenomena*, Nature **159** (1947), doi: 10.1038/159310a0.
- [150] Y. Fan and K. Hill, *Shear-driven segregation of dense granular mixtures in a split-bottom cell*, Phys. Rev. E **81** (2010), doi: 10.1103/PhysRevE.81.041303.
- [151] A. Kumar, *Experimental Surface Profile Of Dense Granular Media in Cylindrical Couette Flow*, Appl. Mech. Mater. **116** (2012), doi: 10.4028/www.scientific.net/AMM.110-116.776.
- [152] M. Shahinpoor and S. Lin, *Rapid couette flow of cohesionless granular materials*, Acta Mechanica **42** (1982), doi: 10.1007/BF01177191.
- [153] F. Boyer, O. Pouliquen, and E. Guazzelli, *Dense suspensions in rotating-rod flows: normal stresses and particle migration*, J. Fluid Mech. **686** (2011), doi: 10.1017/jfm.2011.272.
- [154] M. Harrington, J. H. Weijs, and W. Losert, *Suppression and Emergence of Granular Segregation under Cyclic Shear*, Phys. Rev. Lett. **111** (2013), doi: 10.1103/PhysRevLett.111.078001.
- [155] K. Sakaie, D. Fenistein, T. J. Carroll, M. van Hecke, and P. Umbanhowar, *MR imaging of Reynolds dilatancy in the bulk of smooth granular flows*, Europhys. Lett. **84** (2008), doi: 10.1209/0295-5075/84/38001.
- [156] P. Ribière, P. Richard, R. Delannay, and D. Bideau, *Importance of convection in the compaction mechanisms of anisotropic granular media*, Phys. Rev. E **71** (2005), doi: 10.1103/PhysRevE.71.011304.
- [157] H. J. van Gerner, M. van der Hoef, D. van der Meer, and K. van der Weele, *Interplay of air and sand: Faraday heaping unravelled*, Phys. Rev. E **76** (2007), doi: 10.1103/PhysRevE.76.051305.
- [158] S. Farhadi and B. Behringer, *Dynamics of Sheared Ellipses and Circular Disks: Effects of Particle Shape*, Phys. Rev. Lett. **112** (2014), doi: 10.1103/PhysRevLett.112.148301.
- [159] G. Jeffrey, *The Motion of Ellipsoidal Particles Immersed in a Viscous Fluid*, Proc. R. Soc. Lond. A **102** (1922), doi: 10.1098/rspa.1922.0078.



---

# Samenvatting

---

Dit proefschrift gaat over de natuurkunde van de stroming van granulaire materialen. Een granulair materiaal, zoals zand, is een materiaal dat bestaat uit losse korrels. Hoewel één korrel een simpel object is, kan het collectieve gedrag van miljarden korrels samen erg ingewikkeld zijn. In verrassend veel gevallen is het niet precies bekend hoe een granulair materiaal zich gedraagt en dat terwijl dit soort materialen zowel in het leven van alledag, als in de industrie, als in de natuur enorm veel voorkomen.

Net als materialen zoals water, dat als ijs, vloeibaar water en damp voor kan komen, kan zand ook verschillende toestanden (fases) aannemen. Als je bijvoorbeeld over het strand loopt, dan gedraagt zand zich als een stevige vaste stof, maar als je na afloop het zand uit je schoenen giet, dan stroomt het als een vloeistof. Het voornaamste deel van dit proefschrift gaat over experimenten waar we onderzoeken wat er precies gebeurt als je zand een beetje “vloeibaar” probeert te maken door het zachtjes te schud-den.

Als twee lagen zand langs elkaar stromen, is er een relatief dunne *afschuifzone* waar de korrels daadwerkelijk langs elkaar schuren. Het is gebleken dat zandstroming vrij goed te begrijpen is, als je deze afschuif-zone beschouwt als twee oppervlakken die langs elkaar bewegen met een zekere wrijving. Opvallend genoeg hangt de benodigde kracht niet af van de stroomsnelheid, dit omdat de kracht vooral gebruikt wordt om de wrijving te overwinnen. In hoofdstuk 3 onderzoeken we of dit beeld blijft kloppen als het zand zachtjes geschud wordt. We vinden dat ook het gedrag van heel zacht geschud zand bepaald wordt door wrijving. Echter, de wrijvingsweerstand hangt nu af van hoe hard je precies schudt én van hoe snel het zand stroomt. Als je iets harder schudt, gebeurt er iets heel anders. Het zand wordt nu zo zacht dat je andere natuurkunde, namelijk die van vloeistoffen, nodig hebt om de zandstroming te beschrijven.

Als je een plank met zand steeds iets schever houdt, glijdt het zand voor een zekere hoek ineens hard naar beneden. Het is onmogelijk om zand rustig van de plank te laten stromen. Wanneer de korrels zacht geschud worden, is trage stroming wel mogelijk. Echter, het zand is slechts “vloeibaar” genoeg om heel traag te stromen en er zijn nog steeds tussenliggende snelheden die niet mogelijk zijn. Hoe harder je schudt, hoe meer snelheden er mogelijk worden. Boven een zekere kritische schudintensiteit zijn alle snelheden toegestaan. In hoofdstuk 4 bestuderen we de trage en snelle stroming en de overgang ertussen. We beschouwen dit vanuit het belangrijke, *kritische* punt waar de twee soorten stroming samenkomen.

Als zand een bepaalde kant op heeft gestroomd, heeft die richting zich in het systeem ingebouwd. Dit resulteert erin dat wanneer je het zand nu nogmaals wilt laten stromen, het meer kracht kost om dit weer in dezelfde richting te doen dan in de tegengestelde. We zeggen dat de pakking *anisotroop* is. In hoofdstuk 5 laten we zien dat je deze anisotropie kunt meten door te kijken hoe deze uit de pakking verdwijnt als het systeem geschud wordt. We vinden een relatie tussen hoeveel kracht op het zand werd uitgeoefend toen het stroomde en de resulterende anisotropie. Dit vertelt ons dat anisotropie een cruciaal ingrediënt is voor het begrijpen van zandstroming.

In hoofdstuk 6 bestuderen we de stroming van staafvormige deeltjes. Een belangrijk verschil tussen staaf- en bolvormige deeltjes is dat het voor staafvormige deeltjes van belang is in welke richting ze liggen. Granulaire materialen zetten typisch uit als je ze laat stromen, maar staafjes kunnen zich ordenen waardoor ze juist een zeer hoge dichtheid bereiken. Uit onze stromingsexperimenten, waar we, als we staafjes laten stromen, een heuvel zien verrijzen uit het oppervlak, blijkt dat de uitzetting het van de ordening wint. Uit metingen in een CT-scanner, waarbij we ook de deeltjes onder het oppervlak kunnen zien, blijkt dat er in het midden van het systeem tevens een continue stroming van deeltjes omhoog is die het groeien van de heuvel veroorzaakt. Aan de rand van de heuvel vallen de deeltjes dan weer naar beneden. Dit is een mooi voorbeeld van de invloed van de vorm van de deeltjes op hun stromingsgedrag.



---

# Summary

---

This dissertation is dedicated to the physics of the flow of granular materials. A granular material, such as sand, is a material that consists of a conglomeration of discrete particles. Even though a single particle is a simple object, the collective behavior of billions of particles can be very complex. In a surprisingly large amount of cases, it is not exactly known how a granular material behaves, and this while these kinds of materials are omnipresent in everyday life, industry, and nature.

Similar to materials such as water, which can occur as ice, liquid water and vapor, sand can also exist in different phases of matter. If you for instance walk on the beach, sand behaves like a solid, but if you pour it out of your shoes afterwards, it flows like a liquid. The main part of this thesis is dedicated to experiments where we investigate what happens when you try to “liquefy” sand by weakly vibrating it.

If two layers of sand flow past each other, there is a relatively thin *shear zone* where the particles actually scrape past each other. It was found that sand flow can be understood relatively well if you consider this shear zone as two surfaces sliding past each other with a certain friction. Surprisingly, the required force does not depend on the flow rate, because the force is mostly used to overcome the friction. In chapter 3, we investigate whether this picture remains valid when the sand is weakly vibrated. We find that the behavior of weakly vibrated sand is also determined by friction. However, the frictional resistance now does depend on the amount of vibrations *and* on the flow rate. If you shake more vigorously, something completely different happens. The sand now becomes soft to the extent that you need different physics, namely that of fluids, to describe the sand flow.

If you increasingly tilt a plank with sand, for a certain angle, the sand will rapidly slide down. It is impossible to make the sand slide down the

plank slowly. But, if the grains are weakly vibrated, slow flow *is* possible. However, the sand is only “fluid” enough to sustain very slow flow, and there remain intermediate flow rates that are impossible to induce. The more you vibrate the sand, the fewer rates are impossible. Above a certain critical vibration intensity, all rates are allowed. In chapter 4 we investigate the slow and fast flow, and the transition between these two flow regimes. We consider this from the perspective of the important, *critical* point where the two kinds of flow meet.

If sand has flowed in a certain way, this direction is built into the packing. As a result, if you want to make the system flow more, it requires more force to do this in the same direction than in the opposite. We say the packing is *anisotropic*. In chapter 5 we show that this anisotropy can be measured by looking how it disappears from the packing when the system is vibrated. We find a relation between how much force was exerted during the flow, and the resulting anisotropy. This tells us that anisotropy is a crucial ingredient for the understanding of sand flow.

In chapter 6 we study the flow of rod-shaped particles. An important difference between rod-shaped and spherical particles is that, for rods, it is important in which direction they are oriented. Granular materials typically expand when they are sheared. However, rods can order, thereby reaching a very high density. From our flow experiments, where we see a heap arising from the surface when we shear rods, we know that the expansion dominates over the ordering. From measurements in a CT-scanner, where we can also see the particles below the surface, we know that there is an additional continuous upwards flow of particles in the center of the system. At the edge of the heap, the particles avalanche down its slope. This secondary flow is a good example of the influence of the shape of the particles on their flow properties.

---

# Publication List

---

- [1] G. Wortel, J. Dijksman, and M. van Hecke,  
*Rheology of weakly vibrated granular media*,  
Phys. Rev. E **89**, 012202 (2014).
- [2] J. Dijksman, G. Wortel, L. van Dellen, O. Dauchot, and M. van Hecke  
*Jamming, Yielding, and Rheology of Weakly Vibrated Granular Media*  
Phys. Rev. Lett. **107**, 108303 (2011).
- [3] F. Tabak, E. Disseldorp, G. Wortel, A. Katan, M. Hesselberth  
T. Oosterkamp, J. Frenken, and M. van Spengen  
*MEMS-based fast scanning probe microscopes*  
Ultramicroscopy **110**, 559 (2010).

In preparation:

- [4] G. Wortel and M. van Hecke,  
*Anisotropy of weakly vibrated granular flows*,  
Submitted to Phys. Rev. E, arXiv: 1410.4335 (2014).
- [5] G. Wortel, T. Börzsönyi, S. Wegner, B. Szabo, E. Somfai,  
R. Stannarius, and Martin van Hecke  
*Heaping and Broken Symmetry in Flows of Anisotropic Granular Media*  
In Preparation.



---

# Curriculum Vitae

---

I was born on November 22nd 1985 in Zoetermeer, the Netherlands. My childhood was spent in this same city, and I attended the “Oranje Nassau College” where I obtained my vwo-diploma in 2004. I went on to study Experimental Physics at the University of Leiden. After two research projects, “MEMSPM - Tip formation and actuation”, under supervision of prof. J.W.M. Frenken, and “Piles of Rice - Surface Instability in Sheared Granular Rod Systems”, with prof. M. van Hecke, I received my master’s degree in August 2010.

After a six day vacation, I started my PhD project in M. van Hecke’s “Complex Media and Metamaterials” group. During this time, I attended schools in Edinburgh (Scotland), Beg Rohu (France), and Enschede (The Netherlands). In addition, I went to conferences in Cambridge (England), Boston, Baltimore, Denver (APS March Meetings, United States), and many in The Netherlands. At Physics@FOM Veldhoven (2012) and three APS March Meetings (2012-2014), I presented my work. In 2012, I presented my work at the annual meeting of the Burgerscentrum at the TU Eindhoven and won the prize for the best talk of the day.

During my PhD, I was teaching assistant for the undergraduate courses “Diffusion and Dissipation” and “Fourier Physics”. In addition, I have supervised seven students for a BSc or MSc internship. Besides writing papers, I have been an active referee, having reviewed nine papers for APS journals. I have given many lab tours for the biannual Open House Day of the university, and helped set up fun demonstration experiments.



---

# Acknowledgements

---

This thesis would never have been there if it wasn't for the help and support of several people.

I owe a lot to Martin, who not only encouraged me to do a physics master, but also a PhD. His lessons, help, support, and enthusiasm over the years have been invaluable, and helped me bring my PhD project to a good ending.

Another special thanks goes to Joshua; he supervised my first internship in 2008, and has been my granular mentor ever since.

A big thank you goes to my collaborators. Thank you Olivier Dauchot for your enthusiasm and interesting insights, thank you Ralf Stannarius and Tamás Börzsönyi for our fruitful rod collaboration.

Thanks Jeroen for your amazing technical support. Having Daniëlle as a secretary was a true blessing. Thanks to Eddy van de Wiele who always came to the rescue soon when the rheometer needed fixing.

Thank you fellow PhD students Kiri, Alex, Erik, Daniël, Luuk, Peter, Casper, Vera, and office mates Bastiaan and Merlijn. Thank you postdocs Elie, Siet, Simon, Corentin, Scott, and assistant professor Daniela.

It was a pleasure to work on projects with my students: Anouk, Arthur, Hedwig, Sandra, Swier, Peter (again) and Jean-Yonnel.

On a more personal level I am grateful for the support of my parents, brother and sister, parents in law, friends, family, and my card buddies Daniël, Gerard and Remco. Thank you dad and Hanneke for proofreading my thesis; now you know what I've been up to the last four years. And finally, my dear Hanneke, thank you for always being there for me!